Development and validation of a dynamics model for an unmanned finless airship

Prashant Peddiraju

Master of Engineering

Department of Mechanical Engineering

McGill University

Montreal,Quebec

February 2010

A thesis submitted to McGill University in partial fulfilment of the requirements of the degree of Master of Engineering

ACKNOWLEDGEMENTS

First and foremost, I would like to express my heartfelt thanks to my supervisor Meyer Nahon for his constant support and guidance over the course of my Master's. He is one of the most patient and reasonable people I have known at McGill, and it was truly a pleasure working with him.

I am also grateful to my friend and colleague Torsten Liesk for the time he spent helping me in various aspects of my research. His passion for aviation is infectious and it has re-ignited my own interest in the subject. Thank you to Yuwen Li for helping me understand his airship dynamics model when I began my Master's and for offering his insight on approaches to viscous drag modeling.

I would like to thank the interns and exchange students that worked at the lab for their time and dedication to this project. They are Daniel Peon, Ricardo Freistafilho, Gabriela Waldhart, Geoffrey King, Henna Warma, and Mardig Taslakian.

I would like to thank my friends and family for being there for me through the good times and bad times. I would not have made it this far without your support and encouragement.

Finally, I would like to thank the Natural Sciences and Engineering Research Council (NSERC) for their financial support during this project.

ABSTRACT

The research described in this thesis relates to a highly-maneuverable, almost-lighter-than-air vehicle (ALTAV). The vehicle is controlled by four vectored thrusters and is marginally stable due to its finless design. In order to better understand the behavior of this vehicle, a non-linear mathematical model was developed to represent the behavior of the airship under the effect of thruster forces and wind. The underlying equations of motion in the dynamics model take into account aerostatic and aerodynamic forces on the airship. Physical parameters used in the equations of motion were estimated through experiments and a CAD model. The viscous drag acting on the hull was computed for a 360° range of angle of attack by adapting an existing semi-empirical method for slender bodies. A model of the vectored thrusters developed from experimental data was shown to provide good agreement with actual thrust measurements under static conditions. Reference flight data for model validation was obtained by measuring the airship's response to environmental disturbances and thruster inputs. In general, the simulation was found to provide a reasonable estimate of the airship's roll, pitch and vertical trajectory. However, the airship motion was strongly affected by wind. This suggests that better results would be obtained if the simulation could better reproduce the wind conditions existing during the flight tests.

RÉSUMÉ

La recherche décrite dans cette thèse fait réference à un vehicule flottant très manœvrable. Le véhicule est contrôlé par quatre propulseurs et a peu de stabilité en raison de sa conception sans ailettes. Afin de mieux comprendre le comportement de ce véhicule, un modèle mathématique non-linéaire a été développé pour representer le comportement de l'aéronef sous les effets de ses propulseurs et du vent. Les équations de déplacements/mouvements dans le modèle dynamique prennent en considération les interactions aérostatiques et aérodynamiques qui se produisent entre l'aéronef et l'air environnant. Les paramètres physiques utilisés dans les équations de mouvement ont été estimés à l'aide d'essais réels et d'un modèle CAO(CAD). La resistance aérodynamique agissant sur le châssis a été calculée pour des angles d'attaque de 0° à 360° en adaptant une méthode semi-empirique applicable aux corps minces. Un modèle des propulseurs développé à partir de données expérimentales a démontré un bon accord avec les données de propulsion réelles dans des conditions statiques. Les données pour la validation du modeèle ont été obtenues en mesurant la reaction de l'aéronef sous l'effet de perturbations environnementales et de l'action des propulseurs. En général, la simulation a fourni une estimation raisonnable du roulis, du tangage, et de la trajectoire verticale de l'aéronef. Toutefois, le mouvement de l'aéronef est susceptible d'être fortement affecté par le vent. Ceci suggère que de meilleurs résultats seraient obtenus si la simulation pouvait mieux reproduire les conditions de vent existantes pendant les essais en vol.

TABLE OF CONTENTS

LIST OF TABLES

LIST OF FIGURES

CHAPTER 1
Introduction

1.1 Background

Figure 1–1: TCOM 71M aerostat[1]

Figure 1–2: AS-300 thermal airship[2]

Lighter-Than-Air Vehicles(LTAVs) are aerial platforms that derive some or most of their lift through a lifting gas such as Helium or hot air. Examples of this class of vehicles include blimps(airships), tethered aerostats and hot-air balloons. Over the past couple of decades, there has been a revival of interest in Lighter-Than-Air Vehicle technology due to advances in materials and the ever-increasing cost of fuel. Compared to fixed and rotary wing aircraft, airships have a number of advantages. Firstly, they have a high endurance and can typically remain deployed for days or weeks at a time since very little energy is expended to keep them afloat. For example, the TCOM 71M tethered aerostat's(shown in Figure 1–1) maximum deployment time is rated[1] at an impressive 30 days. The passive generation of lift through buoyancy allows airships to hover and perform station-keeping in an energy-efficient manner. Airships are also relatively stealthy due to their lower heat and noise signature. As a result of these qualities, they excel at tasks such as surveillance, wildlife and oceanographic research, and land mapping where the speed of a fixed-wing aircraft is not needed. Figure 1–2 shows the AS-300 thermal airship assisting scientists working on the forest canopy in Borneo[2]. Here, the AS-300's hovering capabilities and low noise signature enable it to deploy the inflatable observation deck in a non-intrusive way.

On the downside, conventional airship designs are susceptible to winds due to their large surface area. They also suffer from poor handling at low speeds since aerodynamic control surfaces such as the rudder and elevator require airflow over them in order to be effective. To compound the problem, not only do most airships handle poorly, but they are also designed to be inherently stable and thus incapable of maneuvering quickly. As a result, most mid to large sized airships usually require a dedicated ground crew to assist during takeoff and landing. Historically, a number of accidents have occurred during the ground handling phase and the USS Akron is an example of an airship that has suffered its share of mishaps[3]. On February 22, 1932 the USS Akron broke free of its handlers and smashed its vertical stabilizer on the ground (see Figure 1–3). In a separate incident, the USS Akron rose unexpectedly from the ground and lifted up three workers holding on to the mooring lines, who ultimately fell to their death.

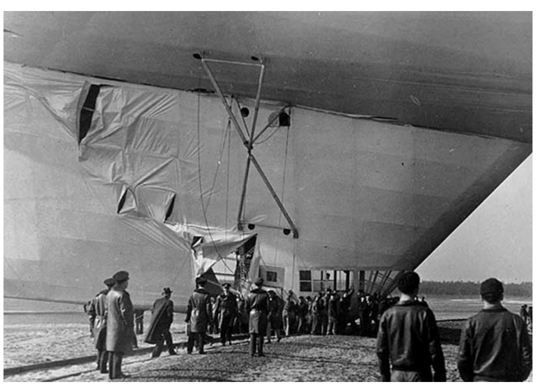

Figure 1–3: The USS Akron after its ground-handling accident[3]

Figure 1–4: Vectored thrusters on Skyship-600

More recent airship designs have incorporated measures to tackle these problems. One way to improve low-speed maneuvering is the use of vectored thrusters, which has been shown to be beneficial by a number of researchers [4, 5, 6, 7]. For example, Nagabhushan, Tomlinson [5] and Faiss [6] have shown through simulations that the use of thrust vectoring can improve an airship's low-speed maneuverability. Their results also indicated that the takeoff and landing distances could be significantly reduced by the use of vectored thrust. Figure 1–4 shows an example of such a thruster setup on the Skyship 600 airship. Some airship designs also incorporate a fixed thruster at the nose and/or tail of the airship to provide lateral thrust and hence improve yaw control. Two methods can be employed to cope with wind: 1) reducing the size of the airship envelope, and 2) installing more powerful thrusters. Unfortunately, there is a weight penalty involved in increasing the thrust capacity of an airship. In addition, reducing the size of the airship envelope leads to a reduction in buoyant lift thereby decreasing its payload. In the following section, a unique LTA vehicle concept is presented that attempts to address the shortcomings of conventional airship designs.

1.1.1 Quanser MkII ALTAV

Figure 1–5: Quanser MkII ALTAV

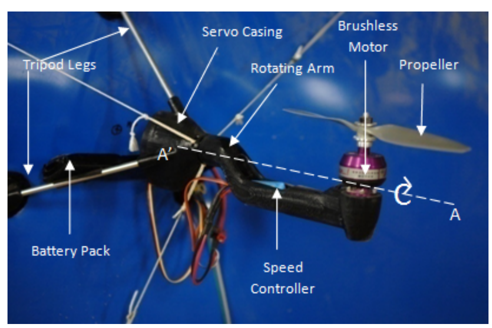

Figure 1–6: Vectored thruster on MkII

The MkII ALTAV (*Almost*-Lighter-Than-Air-Vehicle) is a novel quad-rotor airship that has been developed by Quanser Inc. As can be seen in Figure 1–5, the MkII's hull has a relatively slender, near ellipsoidal shape. The airship is roughly 4.8 m long and has a maximum diameter of approximately 1.5 m. In normal operation, the weight of the airship exceeds the lift generated by the helium. In other words, the airship is negatively buoyant and additional lift must be provided by the thrusters to keep the airship afloat. One advantage of this configuration is that in case of total thruster failure, the airship will drift back to the ground rather than floating away with the wind. Since the vehicle derives only some of its lift from Helium, the envelope size is reduced considerably. This, in turn, makes the vehicle less susceptible to winds due to its reduced surface area.

Perhaps the most distinctive feature of the MkII is its lack of aerodynamic control surfaces. In the absence of restoring forces provided by the fins, the vehicle becomes highly maneuverable albeit at the expense of stability. As a result, stable flight relies heavily on artificial stability provided by its controllers. Control actuation is provided by four thrust sub-assemblies mounted along the equator of the hull. Figure 1–6 shows a close-up of one such unit. A DC brushless motor paired with a 0.305 m(12") diameter propeller is mounted to a rotating arm to deliver thrust and a servo motor changes the direction of application by rotating the arm up to approximately $\pm 90°$ from the vertical. With four thrust and four angle inputs controlling five independent degrees of freedom(lateral translation of the airship is not controlled), there is a redundancy in actuation.

The MkII is capable of fully autonomous operation with little to no intervention by the operator. It is equipped with a flight computer as well as a GPS and Inertial Measurement Unit (IMU) for position and attitude measurements respectively. The data logging system on board the airship is highly configurable, allowing the user to record time histories of up to 50 parameters during flight.

1.1.2 Thesis Objectives and Motivation

The MkII's instability and redundant actuation present an interesting control problem. With more control inputs than independent degrees of freedom, it is possible to employ a variety of control schemes to effect a desired change in its attitude and position. In order to allow controller design without resorting to costly and time-consuming field tests, we need a dynamics model that will accurately represent the vehicle's motion. Another benefit of a dynamics model is that it can serve as a design tool to evaluate various configurations of the airship such as thruster placement and envelope size. Furthermore, a dynamics model can be used to study the modes and stability characteristics of the airship under various flight conditions.

The high angle of attack aerodynamics of airships have been of little interest to researchers since airships usually spend most of their mission time in steady cruise flight, where the flow is generally at a low angle of attack. However, during hover or low-speed maneuvering in the presence of winds, large angles of attack could be experienced by the airship hull. It would therefore be desirable to model the aerodynamic forces experienced by the MkII at very large angles of attack. Another objective of this study shall be to accurately model the transient characteristics of the vectored thrusters of the MkII. This is especially crucial for control design, since an inaccurate model of the thrusters can lead to unrealistic closed-loop simulation results.

1.2 Literature Review

1.2.1 Airship Dynamics

Airship dynamics models have much in common with numerical models for fixed-wing aircraft given by authors such as Etkin[8] and Philips[9], with the exception of two physical effects that are predominant in lighter-than-air vehicles. These are the buoyant lift and added mass. Added mass is a phenomenon which causes an apparent increase in the mass (and inertias) of a moving body due to acceleration of the air surrounding it. The added mass can be quite significant in lighter-than-air flight, often approaching the mass of the vehicle itself. One commonly used method to compute the added mass of an airship hull is by using added mass factors of ellipsoidal shapes given by Lamb[10].

Tischler *et al.*[11, 12] developed a non-linear 6 DOF simulation to study the dynamics of a heavy lift airship powered by four gondola-mounted helicopters. In their simulation, special attention was paid to modeling the aerodynamic and added mass forces on the airship at incidence angles less than 21° as well as interference between the hull, fins and rotors. In a later work[13], this dynamics model was used to analyze the airship's response to atmospheric turbulence.

The dynamics of the Skyship-500 airship were studied by a number of researchers. Jex and Gelhausen[14] adapted the airship dynamics model by Tischler *et al.*[11, 12] to the Skyship-500. Using the airship's measured frequency response to control surface and thruster inputs given in [15], they were able to refine their dynamics model and obtain estimates of the aerodynamic stability derivatives by using a frequency-domain fitting technique. Amann[16] developed a simulation of the Skyship-500 that incorporated DeLaurier's[17] improved method of predicting aerodynamic forces and moments. The model was validated by comparing simulated time and frequency domain responses of the airship to experimental responses obtained from the PACE (Patrol Airship Concept Evaluation)[18] project. Li[21] developed a non-linear 6 degree of freedom (DOF) model of the Skyship-500 and validated it against measured responses given by Jex[14, 15]. The added mass formulation was validated by comparing the estimated (using Lamb[10]) added mass of the Lotte airship against CFD values for the Lotte airship given by Lutz[22].

Gomes[19] developed a model of the Westinghouse YEZ-2A airship and used it to verify the response modes of the airship. One interesting finding by Gomes was that at low speeds, the YEZ-2A exhibited non-minimum phase behavior to elevator inputs. Yamasaki and Goto[20] formulated the non-linear equations of motion for the Sky Probe-J airship and used two different experimental methods to identify parameters in the model. Data from both experiments was fitted to the simulated responses using an extended least-squares algorithm and the authors were able to identify added-mass parameters as well as aerodynamic stability derivatives, ultimately concluding that the analytical predictions of the parameters were consistent with the identified values.

Thomasson[23] derived the generalized equations of motion for a body submerged in a moving fluid and Azinheira[24, 25] adapted these equations specifically to airships moving in a non-stationary wind field. Both Thomasson and Azinheira used a Lagrangian approach to derive the equations of motion and their results were confirmed by Liesk[26] who used Newton's second law to derive the same.

Linearized airship models are commonly used to determine the lateral and longitdudinal modes of the vehicle at a given trim condition, and their evolution with airspeed. Such analyses have been carried out by Cook *et al.*[27], Jex *et al.*[14, 15], and Li[21]. However, since our interest is in simulating the non-linear behavior of the MkII, we shall not linearize the airship dynamics.

1.2.2 Aerodynamic Forces

A number of semi-empirical methods can be found in literature that are valid for low angles of attack. Munk[28] applied a potential flow analysis (slender body theory) to determine the loads acting on an airship hull. One of the more important results from his work was the formulation of the Munk moment, a destabilizing moment that acts about the pitch and yaw axes of a slender body inclined with respect to an airflow. However, the slender body theory is only valid at very low angles of attack since the effects of viscous drag increase at higher angles of attack due to separation of airflow over the hull. Munk's work was later built upon by Allen and Perkins[29], who accounted for viscous crossflow forces in addition to loads due to potential flow. Hopkins[30] estimated the normal force and pitching moment coefficient by applying a combination of potential flow over the expanding portion of the hull and viscous flow over the contracting part. His method was shown to be in good agreement with experimental data for low angles of attack (up to 12°).

Current airship dynamics models[31][20][14] have, in general, not addressed the aerodynamic forces that act on the hull at high angles of attack. With an increasing number of airship applications requiring hover and low-speed flight, often in the presence of winds, there is a need to characterize airship behavior in these flight regimes. Estimation of aerodynamic derivatives at high angles of attack can be done from wind-tunnel data[32] or CFD-based methods[33], but these options can be cost and time prohibitive. A more viable alternative is the use of semi-empirical methods from literature to predict the aerodynamic loads acting on the airship hull. Combining the works of Allen and Perkins[29] and Munk[28], Jorgensen[34] developed semi-empirical relations for the normal force, pitching moment, and axial drag acting on elongated, rocket-like shapes for angles of attack up to 180°. His equations were shown to provide accurate measurements of the pitching moment coefficient and normal force for nine test bodies. However, the axial force prediction showed a large error between an angle of attack of 20° and 90°. Hopkins[30] tested the applicability of Jorgensen's equations to airship-like shapes at low angles of attack ($\leq 20°$) and found that the normal force coefficient and pitching moment coefficient showed a good match to experimental data for bodies of lower fineness ratio.

1.2.3 Thruster Dynamics

Due to the relatively recent emergence of UAVs, the modeling of their thrusters is not well covered by literature yet. In particular, our interest is in characterization of electric powerplants consisting of an open (or ducted) propeller driven by a DC motor. Battipede[33] used a steady-state thrust model in a simulation of the Nautilus unmanned airship. A steady-state model is one in which the modeled thrust output T is proportional to the square of the instantaneous propeller speed ω, i.e. $T = K\omega^2$. The effect of varying axial velocity at the propeller hub was incorporated by adjusting the proportionality constant K. Similarly, Pounds *et al.*[35] included a basic steady-state thrust model in the dynamics of a quad-rotor heavier-than-air UAV. Vertical translation of the propeller hub due to pitch and roll of the vehicle was taken into account by implementing a thrust coefficient which was varied based on the vertical velocity at the hub. However, the authors did not explore the effect of other arbitrary vehicle motions on thrust. In a later work, Pounds *et al.*[36] developed a simple model of a brushless motor driven by a speed controller and powered by a Lithium ion battery. Their model was a second order transfer function built up from a cascade of simplified models for the rotor aerodynamics, motor dynamics and battery response. Identification of the the model parameters was performed by measuring step thrust responses, and then fitting the plant response to it using a known sensor model of the force-torque transducer.

In contrast, there is a sizeable body of work devoted to the study of marine thruster dynamics due to years of ongoing research in the field of ocean vehicle maneuvering. Since a number of underwater thruster models are based on fundamental fluid dynamic and electromechanical principles, they serve as a useful starting point to begin development of an open-air thruster model. The simplest thruster model is one that only calculates the steady-state thrust using the propeller rotation speed.

Experimental data in [37], [38], and [39] validated the notion that under steady-state conditions, thrust generated by a fixed pitch propeller is related to the square of its rotation speed.

In [40], Yoerger *et al.* used an energy balance method to model a shrouded thruster using the propeller speed as the sole state variable and motor torque as the input. Their simulation results predicted that the time thrust response would degrade with lowering inputs to the system and this was also confirmed in experiments. Healey *et al.*[37] developed an improved, two state (propeller speed, axial flow velocity) shrouded thruster model that used blade-element theory to determine the propeller thrust and hydrodynamic loading torque. The inclusion of DC motor dynamics makes this model more complete than the work in [40]. The authors also adapted their model to an open thruster by tuning parameters in the propeller thrust and torque equations.

Neither [37] nor [40] took into account non-zero ambient fluid velocity or the effect of inlet flow that was not parallel to the thrust axis. Saunders and Nahon[39] extended the work in [37] to include these effects by augmenting the steady-state portion of the thrust response based on the AUV's yaw angle, forward speed and direction of thrust. While their model successfully predicted the thrust response for a variety of yaw angles and forward speeds, its use of vehicle-specific experimental data means it cannot be used directly to model other similar thruster configurations.

1.3 Thesis Organization

This thesis deals with the development and validation of a non-linear dynamics model for the Quanser MkII ALTAV. The dynamics model was broken down into two parts. First, Chapter 2 focuses on modeling the dynamics of the bare airship hull. Estimation of physical parameters in the equations of motion is discussed followed by the modeling of viscous drag acting on the airship. Next, in Chapter 3, a dynamics model of the MkII's thrusters is developed by identification of parameters through experimental data. The thruster model is also validated through comparison with experimental data to check the accuracy of the prediction of the thruster's transient behavior. Chapter 4 presents a comparison of flight test and simulated results along with a discussion on the discrepancies. Finally, in Chapter 5, concluding remarks are made and suggestions are given for future improvements to the model.

CHAPTER 2
Airship Model

The main focus of this chapter is modeling the non-linear dynamics of the MkII airship. One of the goals in developing an accurate numerical model of the airship is to eventually use it as a foundation for controller development. To this end, a substantial effort was made to accurately estimate the various physical parameters that appear in the equations of motion. Of particular importance are those related to the aerodynamic, aerostatic and added mass forces that are experienced in flight. In Section 2.1, the equations of motion are presented along with an discussion on the various force and moment terms. Section 2.2 is devoted to determining the physical parameters used in the equations of motion. In this section, the airship's inertial properties are estimated experimentally and then verified against a CAD model. Finally, Section 2.3 deals with a semi-empirical method of estimating the viscous drag acting on the airship hull. This section also discusses how the chosen method, originally developed for slender rocket-like shapes, was adapted to the MkII.

2.1 Equations of Motion

This section details the equations that govern the motion of the airship. We start by stating some assumptions as well as defining the reference frames and attitude representation used in the following sections. The airship is treated as a rigid body having six degrees of freedom: three translational (surge, sway, heave) and three rotational (roll, pitch, yaw). These are shown graphically in Figure 2–1. The geographic North-East-Down (NED) frame $\{AXYZ\}$ is an inertial earth-fixed frame whose X axis points to geographic north, Y axis points east and Z axis points down

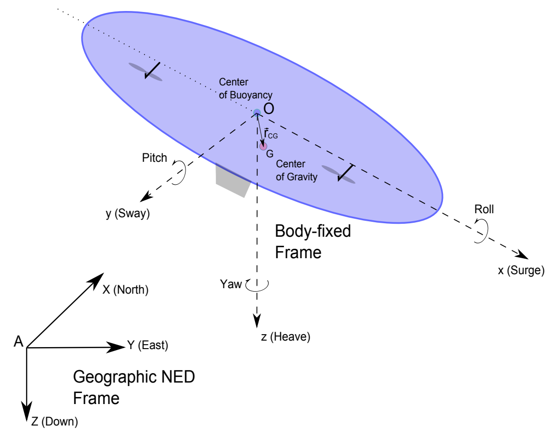

Figure 2–1: Illustration of airship degrees of freedom

towards the center of the earth. A body-fixed frame $\{oxyz\}$ is attached to the airship with its origin o at the center of buoyancy (COB) and its x axis pointing towards the nose, y axis pointing to the right side of the airship and the z axis pointing down. The attitude of the airship is defined by the $Z - Y - X$ Euler angle convention[8], which is comprised of the following sequence of rotations to align the geographic NED frame to the body-fixed frame:

1. Rotate $\{AXYZ\}$ by ψ degrees about the Z axis to align with $\{A_1X_1Y_1Z_1\}$ frame
2. Rotate $\{A_1X_1Y_1Z_1\}$ by θ degrees about the Y_1 axis to align with $\{A_2X_2Y_2Z_2\}$ frame
3. Rotate $\{A_2X_2Y_2Z_2\}$ by ϕ degrees about the X_2 axis to align with $\{oxyz\}$ frame

where the three rotation angles ψ, θ, and ϕ are the yaw, pitch, and roll angles respectively. We can obtain the direction cosine matrix (DCM) from the geographic NED to the body frame by combining elementary rotation matrices in the sequence indicated above to get:

$$\boldsymbol{R}_{Geo\to Body} = \boldsymbol{R}_X(\phi)\boldsymbol{R}_Y(\theta)\boldsymbol{R}_Z(\psi) = \begin{bmatrix} c_\theta c_\psi & c_\theta s_\psi & -s_\theta \\ s_\theta s_\phi c_\psi - c_\phi s_\psi & s_\theta s_\phi s_\psi + c_\phi c_\psi & s_\phi c_\theta \\ c_\phi s_\theta c_\psi + s_\phi s_\psi & c_\phi s_\theta s_\psi - s_\phi c_\psi & c_\theta c_\phi \end{bmatrix} \tag{2.1}$$

in which s_x and c_x are shorthand for $sin(x)$ and $cos(x)$. The DCM $\boldsymbol{R}^{-1}_{Geo\to Body} = \boldsymbol{R}^{T}_{Geo\to Body}$ is used to transform a vector from the body frame to the geographic NED frame.

In order to describe the motion of the airship as completely as possible, the dynamics model includes forces and moments from the following:

1. **Aerodynamics** - Viscous drag exerted on the moving airship hull.
2. **Added Mass** - Apparent increase in inertia of the moving airship due to acceleration of the air around it.
3. **Wind** - Effect of wind on the aerodynamic drag and added mass.
4. **Thrusters** - Loads exerted by the four vectorable thrusters of the MkII.
5. **Gravity** - Force and moment exerted due to weight of airship acting at CG.
6. **Buoyancy** - Buoyant lift produced by displacement of air.

The underlying non-linear equations of motion for this dynamics model have been derived in [26] using Newton's second law with the basic equations shown below:

$$\frac{d(\boldsymbol{p})_i}{dt} = \Sigma(\boldsymbol{f})_i \tag{2.2}$$

$$\frac{d(\boldsymbol{h})_i}{dt} = \Sigma(\boldsymbol{n})_i \tag{2.3}$$

where the right hand sides of equations (2.2) and (2.3) are the net applied force and moment expressed in the inertial frame. The terms $(\boldsymbol{p})_i$ and $(\boldsymbol{h})_i$ are the linear and angular momentum vectors respectively expressed in the inertial frame. After evaluating the time derivatives on the left hand sides of equations (2.2) and (2.3), we transform the two equations back to the body-fixed frame. For the sake of brevity, only the resulting translational and rotational equations of motion have been presented and the reader is referred to [26] for the complete derivation. Expressed in the body-fixed frame, the equations of motion may be written in a compact matrix form:

$$\begin{bmatrix} \dot{\boldsymbol{v}} \\ \dot{\boldsymbol{\omega}} \end{bmatrix} = \bar{\boldsymbol{M}}_a^{-1} \begin{bmatrix} -\boldsymbol{\omega}^{\times}\boldsymbol{M}_a\boldsymbol{v} + m\boldsymbol{\omega}^{\times}\boldsymbol{r_{CG}}^{\times}\boldsymbol{\omega} + \boldsymbol{\omega}^{\times}\boldsymbol{M}_{Da}\boldsymbol{v}_w - \boldsymbol{M}_{Da}\boldsymbol{\omega}^{\times}\boldsymbol{v}_w + \boldsymbol{M}_{Da}\dot{\boldsymbol{v}}_w + \boldsymbol{f}_V + \boldsymbol{f}_T + \boldsymbol{f}_G \\ -m\boldsymbol{r_{CG}}^{\times}\boldsymbol{\omega}^{\times}\boldsymbol{v} - \boldsymbol{\omega}^{\times}\boldsymbol{J}_a\boldsymbol{\omega} - (\boldsymbol{v} - \boldsymbol{v}_w) \times \boldsymbol{M}_{Da}(\boldsymbol{v} - \boldsymbol{v}_w) + \boldsymbol{n}_V + \boldsymbol{n}_T + \boldsymbol{n}_G \end{bmatrix} \tag{2.4}$$

The 6×1 acceleration vector on the left hand side of equation (2.4) consists of $\dot{\boldsymbol{v}}=[\dot{u}\ \dot{v}\ \dot{w}]^T$ and $\dot{\boldsymbol{\omega}}=[\dot{p}\ \dot{q}\ \dot{r}]^T$, which are the linear and angular acceleration vectors expressed in the body-fixed frame. $\bar{\boldsymbol{M}}_a \in \Re^{6\times 6}$ is the generalized apparent mass matrix which contains the true mass and inertias of the airship as well as relevant added mass terms. It is defined as follows:

$$\bar{\boldsymbol{M}}_a = \begin{bmatrix} \boldsymbol{M}_a & -m\boldsymbol{r_{CG}}^{\times} \\ m\boldsymbol{r_{CG}}^{\times} & \boldsymbol{J}_a \end{bmatrix} = \begin{bmatrix} m\boldsymbol{I} + \boldsymbol{A}_m & -m\boldsymbol{r_{CG}}^{\times} \\ m\boldsymbol{r_{CG}}^{\times} & \boldsymbol{J} + \boldsymbol{A}_J \end{bmatrix}. \tag{2.5}$$

where m is the total mass of the airship (including the enclosed Helium gas) and $\boldsymbol{r_{CG}}$ is the position vector of the airship's center of gravity (CG) with respect to the center of buoyancy (COB). $\boldsymbol{r_{CG}}^{\times}$ is the skew-symmetric matrix , which, when multiplied by a vector $\boldsymbol{u}$, represents the cross product $\boldsymbol{r_{CG}} \times \boldsymbol{u}$. $\boldsymbol{M}_a$ and $\boldsymbol{J}_a$ are the *apparent* mass and inertia matrices respectively. As seen in equation (2.5), $\boldsymbol{M}_a$ and $\boldsymbol{J}_a$ are computed from the sum of the true mass and inertia ($m\boldsymbol{I}$ and $\boldsymbol{J}$) and the *added* mass and inertia ($\boldsymbol{A}_m$ and $\boldsymbol{A}_J$). Estimation of the added mass and inertia matrices shall be discussed further in Section 2.2.6.

On the right hand side of equation (2.4), $\bar{\boldsymbol{M}}_a^{-1}$ is multiplied by a 6×1 vector containing the net force and moment acting on the airship, expressed in the body frame. The inertial force terms are given by $-\boldsymbol{\omega}^{\times}\boldsymbol{M}_a\boldsymbol{v}+m\boldsymbol{\omega}^{\times}\boldsymbol{r_{CG}}^{\times}\boldsymbol{\omega}$. Note that the added mass effect is taken into account by the use of the apparent mass matrix $\boldsymbol{M}_a$ instead of the true mass matrix $m\boldsymbol{I}$. The inertial moment contribution is $-m\boldsymbol{r_{CG}}^{\times}\boldsymbol{\omega}^{\times}\boldsymbol{v}-\boldsymbol{\omega}^{\times}\boldsymbol{J}_a\boldsymbol{\omega}$.

Coupling between the effect of wind and added mass is exhibited by the wind related force terms $\boldsymbol{\omega}^{\times}\boldsymbol{M}_{Da}\boldsymbol{v}_w-\boldsymbol{M}_{Da}\boldsymbol{\omega}^{\times}\boldsymbol{v}_w+\boldsymbol{M}_{Da}\dot{\boldsymbol{v}}_w$. Here, $\boldsymbol{v}_w$ and $\dot{\boldsymbol{v}}_w$ represent the wind velocity and acceleration vectors expressed in the body-fixed frame and $\boldsymbol{M}_{Da}$ is the apparent displaced mass matrix, calculated as shown below:

$$\boldsymbol{M}_{Da} = m_D\boldsymbol{I} + \boldsymbol{A}_m \tag{2.6}$$

where m_D is the mass of air displaced by the airship and $\boldsymbol{A}_m$ is the added mass matrix that was defined previously. The moment term $-(\boldsymbol{v}-\boldsymbol{v}_w)\times\boldsymbol{M}_{Da}(\boldsymbol{v}-\boldsymbol{v}_w)$, also known as the Munk moment, has a destabilizing effect on the pitch and yaw motion of the airship. In contrast to the wind related force terms which depend solely on the wind speed and accleration, the Munk moment depends on $\boldsymbol{v}-\boldsymbol{v}_w$, the *airspeed* of the vehicle. In general, the Munk moment tends to turn the airship's longitudinal axis normal to the airspeed vector.

$\boldsymbol{f}_V$ and $\boldsymbol{n}_V$ are the force and moment exerted on the airship hull due to viscous drag. Section 2.3 discusses a semi-empirical method of estimating them. $\boldsymbol{f}_T$ and $\boldsymbol{n}_T$ are the loads generated by the four vectorable thrusters of the MkII. They will be derived in Chapter 3. The effects of gravity and buoyancy have been combined into a single force and moment term, $\boldsymbol{f}_G$ and $\boldsymbol{n}_G$ defined as shown below:

$$\boldsymbol{f}_G = (m-\rho V)\boldsymbol{R}_{Geo\to Body}\begin{bmatrix}0\\0\\g\end{bmatrix}, \qquad \boldsymbol{n}_G = m\boldsymbol{r}_{CG}{}^{\times}\boldsymbol{R}_{Geo\to Body}\begin{bmatrix}0\\0\\g\end{bmatrix} \tag{2.7}$$

where $\boldsymbol{R}_{Geo\rightarrow Body}$ is the transformation matrix from the geographic NED to body-fixed frame defined in equation (2.1), V is the internal volume of the airship, and ρ is the density of air at a temperature of 20°C.

Solution of the Equations of Motion

We can rewrite equation (2.4) as

$$\ddot{\boldsymbol{x}}_{body} = \bar{\boldsymbol{M}}_a^{-1} \cdot \boldsymbol{k}(\dot{\boldsymbol{x}}_{body}, \boldsymbol{x}_{inertial}, \boldsymbol{v}_w, \dot{\boldsymbol{v}}_w) \tag{2.8}$$

in which $\dot{\boldsymbol{x}}_{body} = [u\ v\ w\ p\ q\ r\ ]^T$ is the velocity state vector in the body-fixed frame. $\boldsymbol{x}_{inertial} = [X\ Y\ Z\ \psi\ \theta\ \phi]^T$ is the position state vector in the geographic NED frame. $\dot{\boldsymbol{x}}_{inertial}$ can be transformed to $\dot{\boldsymbol{x}}_{body}$ by the transformation matrix $\boldsymbol{T} \in \Re^{6\times 6}$.

$$\dot{\boldsymbol{x}}_{body} = \boldsymbol{T}\dot{\boldsymbol{x}}_{inertial} \tag{2.9}$$

where

$$\boldsymbol{T} = \begin{bmatrix} \boldsymbol{R}_{Geo\rightarrow Body} & 0 \\ 0 & \boldsymbol{S} \end{bmatrix} \tag{2.10}$$

$\boldsymbol{R}_{Geo\rightarrow Body}$ was defined previously in equation (2.1) and $\boldsymbol{S}$ is a matrix that transforms Euler angle rates to body angular rates:

$$\boldsymbol{S} = \begin{bmatrix} 1 & 0 & -s_\theta \\ 0 & c_\phi & s_\phi c_\theta \\ 0 & -s_\phi & c_\phi c_\theta \end{bmatrix} \tag{2.11}$$

$\boldsymbol{k} \in \Re^{6\times1}$ is a vector of the net force and moment acting on the airship. The matrix form of the airship equations of motion presented in equation (2.8) can be solved with the steps below:

1. Set initial values for inertial state vectors $\boldsymbol{x}_{inertial}$ and $\dot{\boldsymbol{x}}_{inertial}$.
2. Set initial values for wind velocity and acceleration in inertial frame.
3. Transform $\dot{\boldsymbol{x}}_{inertial}$ to $\dot{\boldsymbol{x}}_{body}$ using equation (2.9).
4. Transform inertial wind speed and acceleration to $\boldsymbol{v}_w$ and $\dot{\boldsymbol{v}}_w$ using DCM in equation (2.1).
5. Compute the forces and moments acting on airship $\boldsymbol{k}(\dot{\boldsymbol{x}}_{body}, \boldsymbol{x}_{inertial}, \boldsymbol{v}_w, \dot{\boldsymbol{v}}_w)$.
6. Compute body-fixed acceleration vector $\ddot{\boldsymbol{x}}_{body}$ using equation (2.8).
7. Integrate accelerations to get $\dot{\boldsymbol{x}}_{body}$.
8. Transform $\dot{\boldsymbol{x}}_{body}$ to $\dot{\boldsymbol{x}}_{inertial}$ using $\dot{\boldsymbol{x}}_{inertial} = \boldsymbol{T}^{-1}\dot{\boldsymbol{x}}_{body}$.
9. Integrate $\dot{\boldsymbol{x}}_{inertial}$ to get $\boldsymbol{x}_{inertial}$.
10. Repeat steps 4-9.

2.2 Estimation of Physical Parameters

The airship equations of motion in equation (2.4) make use of a number of physical parameters such as the airship mass, inertias, CG location. In order to model the MkII's dynamics as accurately as possible, special emphasis was placed on estimation of these parameters by CAD and experimental data. To begin, the airship's hull profile was measured experimentally in the lab. Tests were conducted to determine the variation of buoyant lift and hull dimensions with inflation pressure. Based on results from these tests, the measured hull profile was adjusted to reflect the inflation pressure during test flights after which, the location of the airship's CG was determined experimentally. Next, a CAD model was constructed based on the adjusted hull profile and the airship's inertial properties were computed from it. Finally, the airship's added mass was estimated by techniques found in literature.

2.2.1 Measurement of Hull Profile

Figure 2–2: Plumb-bobs suspended along airship hull

A mathematical description of the hull profile is useful in estimation of parameters such as the volume, surface area (for drag computation), added mass, and finally, for constructing a CAD model. The MkII, like most other airships, has a near-ellipsoidal hull that is formed as a body of revolution about the longitudinal x axis. Its hull profile was measured in the lab by first suspending plumb-bobs over the left and right sides of the inflated airship held horizontally (shown in Figure 2–2). The location of each one was then marked on a sheet of paper below the airship and the coordinates with respect to the nose were computed. Due to the presumed symmetry of the hull about the longitudinal axis, only half these data points were entered into MATLAB and an eighth-order polynomial was fitted to them. This polynomial is given in equation (2.12). Figure 2–3 shows the experimental data points along with the polynomial approximation.

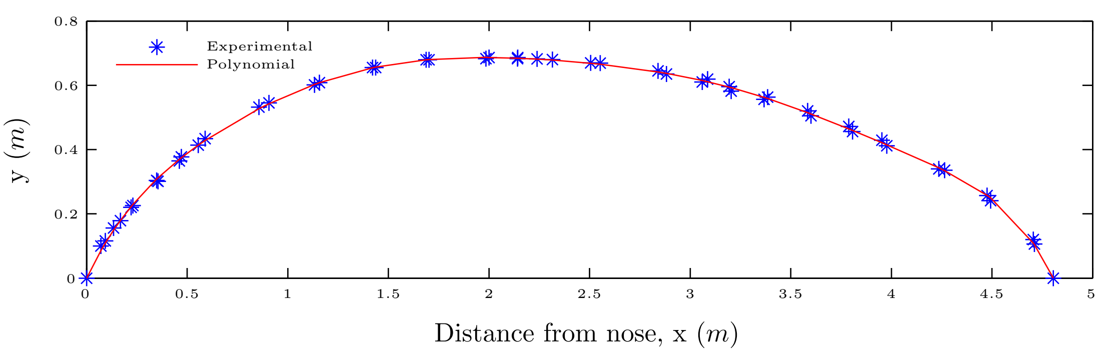

Figure 2–3: Polynomial approximation of hull profile

$$r(x) = -0.0010x^8 + 0.0194x^7 - 0.1489x^6 + 0.6080x^5 - 1.4291x^4 + 1.9906x^3 - 1.7876x^2 + 1.3180x \tag{2.12}$$

The airship's cross-sectional radius obtained from equation (2.12) is valid for $0 \leq x \leq 4.805\ m$ where $4.805\ m$ is the length of the airship. It should be noted that nose and tail of the airship are actually more blunt than shown in Figure 2–3 as a result of which, the true airship length is around $\approx 7\ cm$ shorter than the mathematical representation. The maximum airship diameter from the polynomial is $1.37\ m$ at a distance of $2\ m$ behind the nose.

A year after this profile was measured, the hull was retired due to excessive wear and tear. It was replaced by a newer hull of the same model with which all lab tests in the following sections were performed.

2.2.2 Effect of Inflation Pressure on Hull Profile and Buoyant Lift

In order to completely specify the buoyant lift in our dynamics model, we need knowledge of the Helium pressure and temperature at which that lift is generated. Due to the unavailability of a pressure gauge at the time of the tests, the measured hull profile and all flight tests in Chapter 4 were based on an inflation pressure that was determined strictly by feel and visual inspection of wrinkles in the hull fabric. However, during later lab tests a significant change in the lifting capacity was observed as the internal pressure of the hull was increased. Velcro patches on the hull were also seen to move farther away from each other with increasing pressure, which suggests stretching of the hull. In order to quantify the effect of increasing internal pressure, a pressure gauge was obtained, and an experiment was conducted to record the buoyant lift, hull diameter, and overall length as a function of increasing internal pressure.

Test Configuration

The airship hull was inflated and tied down horizontally using lightweight cords of equal length at its nose and tail. A Berkley FS15 [41] force gauge was attached at both ends of the hull in order to measure the net upward pull. The FS15's rated accuracy of ± 7 g is more than sufficient for our purposes. A UEI EM151 digital manometer [42] was chosen for the pressure measurements due to its low 0.13 $mBar$ resolution and 1.0% full scale accuracy over a large range of -50 $mBar$ to +50 $mBar$.

Measurements Made

The range of internal pressures tested was 2.5 $mBar$ to 5 $mBar$ in increments of $\approx$0.5 $mBar$. At each inflation pressure, the following quantities were measured:

1. Front and rear force gauge readings
2. Circumference at a distance of 2.2 m from the nose - This is the longitudinal distance from the nose at which the gondola and GPS antenna are mounted. A tape measure around the airship hull was used for this measurement.
3. Overall length - A plumb bob was attached to the nose and tail of the airship. The distance between the two was measured using a tape measure.

Results

The circumference, diameter, length and fish scale measurements are presented in Table 2–1. It can be seen that the circumference changes by 25 cm over the range of pressures tested. This corresponds to an increase in diameter of 8 cm. The rapid change in the airship's diameter towards the higher end of pressures indicates that further inflation might have ruptured the hull. The overall length was measured after adding some weight to the airship since the nose and tail support reactions tend to distort the hull. The length measurement at 4.5 $mBar$ is most likely erroneous since that particular measurement was made using a single plumb bob that was

Table 2–1: Raw dimensions as a function of inflation pressure

Pressure, $mBar$	Circumference @ 2.2m, m	Diameter, m	Length, m	Nose Scale Reading, N	Tail Scale Reading, N
2.500	4.580	1.458	4.730	13.891	11.850
3.000	4.610	1.467	4.740	14.195	12.145
3.500	4.650	1.480	4.740	14.656	12.370
4.050	4.700	1.496	4.720	14.872	12.802
4.500	4.740	1.509	4.675	15.206	13.047
5.000	4.830	1.537	4.720	15.774	13.489

transferred from nose to tail. Excluding this measurement, we see that the length of the hull is essentially constant with inflation pressure. A ± 1 cm deviation over an average length of 4.73 m can be considered to be within bounds of experimental error. The constant length of the hull with increasing pressure allows us to postulate the following:

1. The longitudinal position of the COB should stay constant with inflation pressure. Also, since the bare inflated hull is axisymmetric about the longitudinal axis and presumably expands uniformly in the radial direction with increasing pressure, the center of buoyancy's lateral/vertical offset can be neglected.
2. The distance of the CG of the bare hull from the nose does not change with increasing pressure.

Before computing the buoyant lift, we first find the weight and CG location of the bare inflated hull. The hull was inflated with air and suspended horizontally from the ceiling of the lab. The nose and tail support reactions were measured using the FS15 force gauge to be $T_{nose} = 9.584$ N and $T_{tail} = 9.032$ N. A free body diagram of this setup is shown in Figure 2–4. W_{Hull} is the weight of the inflated hull acting at a distance X_{CGHull} from the nose along the longitudinal axis of the hull. Using Figure 2–4, we perform a vertical force balance to find the weight of the hull, $W_{Hull} = T_{nose} + T_{tail} = 18.616$ N. A moment balance about the nose yields the

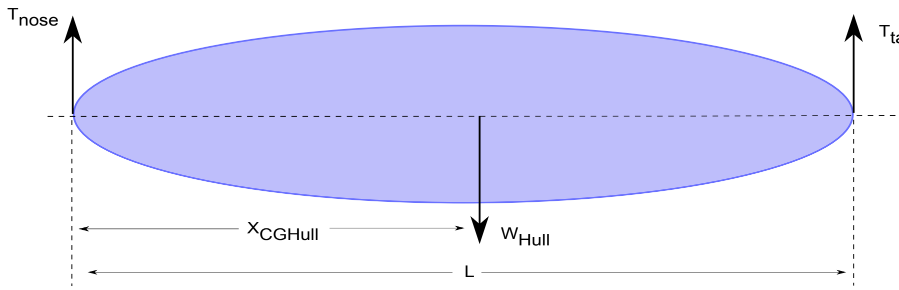

Figure 2–4: Free body diagram of bare hull inflated with air.

distance of the hull's CG from the nose

$$X_{CGHull} = \frac{T_{tail} L}{T_{tail} + T_{nose}} = \frac{9.032 \times 4.73}{9.032 + 9.584} = 2.294\ m \tag{2.13}$$

where $L = 4.73\ m$ is the average airship length computed from Table 2–1.

We can now calculate the buoyant lift of the Helium-filled hull from the nose and tail fish scale measurements. In equation (2.7) of Section 2.1, the buoyant lift acting vertically upwards was defined as the weight of air displaced by the airship hull. That is,

$$F_b = \rho V g \tag{2.14}$$

We now represent the buoyant lift F_b in a free body diagram of the experiment:

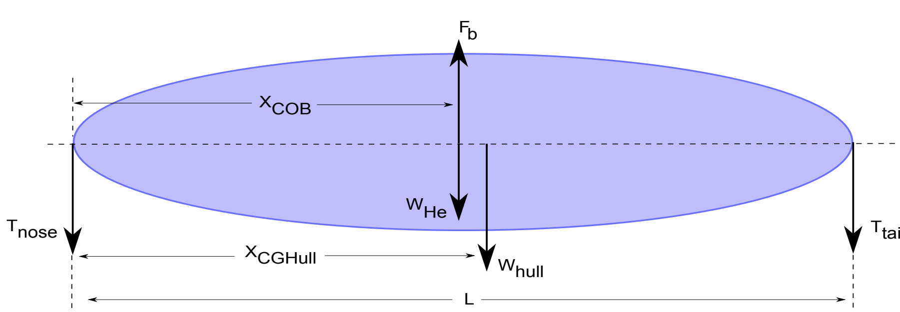

Figure 2–5: Free body diagram of bare hull inflated with Helium.

In Figure 2–5, F_b and the weight of the enclosed Helium, W_{He}, act at the center of buoyancy located at a distance X_{COB} from the nose. The weight of the bare inflated hull W_{Hull} acts at a distance X_{CGHull} from the nose. T_{nose} and T_{tail} are support reactions from the cords at the nose and tail that hold the airship down. Doing a force balance in the vertical direction

$$F_b = W_{He} + T_{nose} + T_{tail} + W_{Hull} \tag{2.15}$$

Using the definition of buoyant lift in equation (2.14) and $W_{He} = \rho_{He} V g$

$$(\rho - \rho_{He})Vg = T_{nose} + T_{tail} + W_{Hull} \tag{2.16}$$

$$V = \frac{T_{nose} + T_{tail} + W_{Hull}}{(\rho - \rho_{He})g} \tag{2.17}$$

For each inflation pressure, the airship volume can be determined by substituting values for T_{nose} and T_{tail} from columns 4 and 5 in Table 2–1. W_{Hull} was found to be 18.616 N. We use air and helium densities at the NIST[43] standard temperature of 20°C, $\rho = 1.204\frac{kg}{m^3}$ and $\rho_{He} = 0.166\frac{kg}{m^3}$. Once the volume is known, equation (2.14) yields the buoyant lift. The calculated values of V and F_b at each inflation pressure are given in Table 2–2.

To compute the location of the center of buoyancy X_{COB}, we perform a moment balance about the nose

$$(F_b - W_{He})X_{COB} = W_{Hull}X_{CGHull} + T_{tail}L \tag{2.18}$$

$$X_{COB} = \frac{W_{Hull}X_{CGHull} + T_{tail}L}{(F_b - W_{He})} \tag{2.19}$$

where $W_{Hull} = 18.616\ N$ and $X_{CGHull} = 2.294\ m$ were computed previously. Using equation (2.19) the center of buoyancy location can be computed, and the values obtained are given in Table 2–2.

Table 2–2: Pressure vs Volume, Buoyant Lift, and Center of Buoyancy Location

Pressure $mBar$	Volume m^3	Buoyant Lift, N	Center of Buoyancy, m
2.500	4.358	51.471	2.226
3.000	4.417	52.166	2.228
3.500	4.484	52.962	2.218
4.050	4.548	53.714	2.231
4.500	4.605	54.385	2.228
5.000	4.704	55.558	2.224

From the values in column 3, it can be seen that there is a 4 N ($\approx$408 g) gain in buoyant lift from 2.5 to 5 $mBar$ internal pressure. On an airship the size of the MkII, this is quite significant since it opens up possibilities for adding additional payload. The center of buoyancy is, as expected, relatively constant since the length of the airship doesn't change appreciably with pressure. The average value of the center of buoyancy is 2.226 m.

2.2.3 Adjusting the Measured Hull Profile

In Section 2.2.2, the effect of the hull's internal pressure on its dimensions was demonstrated experimentally. Although there was negligible expansion of the hull longitudinally, a considerable increase in diameter was observed with increasing pressure. When measuring the profile of the hull, its inflation level was determined solely by feel. As a result, the polynomial representation that was obtained in Section 2.2.1 may not be representative of flight conditions. In particular, we are interested in obtaining the shape of the hull during the test flights presented in Chapter 4. The most accurate way of doing this would be to inflate the airship to the same internal pressure that was used during the flight and measure the profile once again. Unfortunately, in addition to being time consuming, this option is not feasible as the hull's pressure was not measured during the flight tests. We therefore resort to an alternate solution.

If we can somehow *estimate* the hull's internal pressure during the flights, Table 2–1 in Section 2.2.2 can give us the hull diameter 2.2 m behind the nose. Let us denote this value by d_{new}. Using the polynomial representation, $r(x)$, of the measured hull profile in equation (2.12) we can find the diameter, $d_{old} = 2r(2.2)$, at the same longitudinal station. A new hull profile can thus be obtained by scaling the old one as follows

$$r_{new}(x) = \left(\frac{d_{new}}{d_{old}}\right) r(x) \tag{2.20}$$

The airship was configured in a manner that matched, as closely as possible, the way it was setup for the flight tests. Specifically, the airship was inflated until there was no slack in the GPS antenna cable, which runs from the top of the hull to the GPS receiver in the gondola. At this condition, the inflation pressure was measured to be ≈3.5 $mBar$. From Table 2–1, we find $d_{new} = 1.480$ m at a pressure of 3.5 $mBar$. If the hull profile polynomial $r(x)$ is evaluated at $x = 2.2$, we find $d_{old} = 2r(2.2) = 1.365$ m. Comparing the old and new diameters, it is clear that the existing hull profile was measured at a lower inflation pressure than the flight tests. Using equation (2.20) we obtain the polynomial shown in equation (2.21). The scaled and original hull profiles have been plotted in Figure 2–6.

$$r_{new}(x) = -0.0011x^8 + 0.0210x^7 - 0.1614x^6 + 0.6591x^5 - 1.5490x^4 + 2.1577x^3 - 1.9376x^2 + 1.4286x \tag{2.21}$$

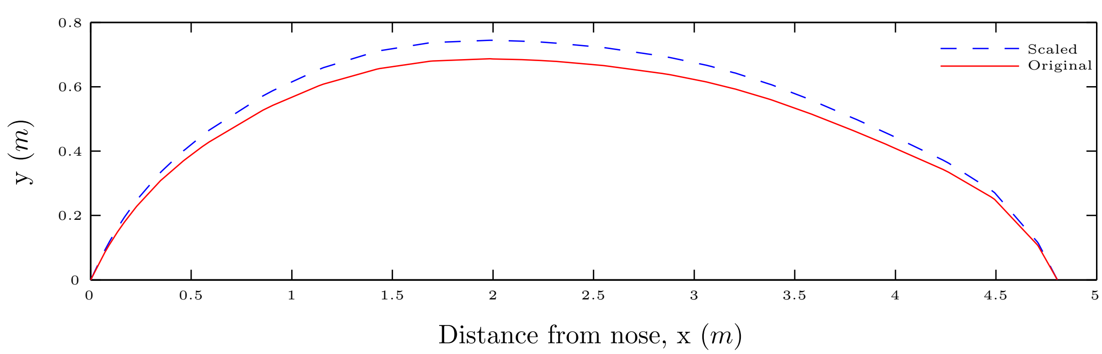

Figure 2–6: Adjusted hull profile of the MkII airship

2.2.4 Computing CG for Flight Conditions

In the previous section, the hull pressure during the test flights was estimated to be roughly 3.5 $mBar$. Since we already know the buoyant lift at this pressure, the location of the center of gravity of the fully rigged airship can be determined experimentally. A breakdown of the MkII's payload when fully rigged is presented in Table 2–3 with the corresponding masses. At the bottom of the table, the total mass including Helium has been estimated using the internal volume at 3.5 $mBar$ computed in Table 2–2. The airship was outfitted with this payload and inflated to a pressure of 3.5 $mBar$. To find the longitudinal position of the CG (distance from the nose), the airship was first suspended horizontally from the ceiling of the lab and the support reactions $T_{nose} = 4.836\ N$ and $T_{tail} = 3.895\ N$ were measured using the FS15 force gauge.

Table 2–3: MkII payload with masses

Item	**Mass,** kg
Hull (incl. patches)	1.898
Gondola (incl. avionics)	0.740
Thruster 1 (incl battery)	0.697
Thruster 2 (incl battery)	0.703
Thruster 3 (incl battery)	0.693
Thruster 4 (incl battery)	0.699
Sonar (w/ cable)	0.012
GPS antenna (w/ cable)	0.131
IMU (w/ cable)	0.105
Total	5.678
+ 4.484 m^3 of Helium at 0.166 $\frac{kg}{m^3}$	6.422

A free body diagram of this setup is shown in Figure 2–7. W is the total weight of the hull payload and lifting gas acting at a longitudinal distance X_{CG} from the nose and Z_{CG} below the midplane of the airship. The buoyant lift F_b acts at a distance X_{COB} from the nose. As before, T_{nose} and T_{tail} are the support reactions holding the airship up.

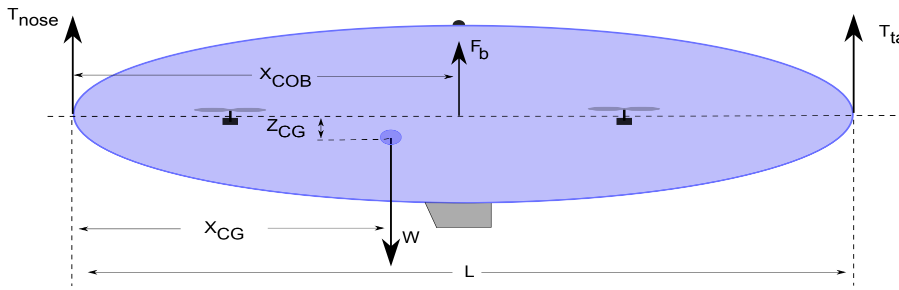

Figure 2–7: Free body diagram of fully rigged, suspended airship

W can be calculated by a force balance in the vertical direction

$$W = T_{nose} + T_{tail} + F_b \tag{2.22}$$

Substituting $T_{nose} = 4.836\ N$ and $T_{tail} = 3.895\ N$ and $F_b = 52.962\ N$ yields $W = 61.693\ N$. This corresponds to a total mass (including the Helium) of 6.288 kg. In comparison with the predicted overall mass in Table 2–3, there is a small error of 2.1%. X_{CG} can be found by performing a moment balance about the nose

$$\begin{aligned}
WX_{CG} &= F_b X_{COB} + T_{tail} L && (2.23)\\
X_{CG} &= \frac{F_b X_{COB} + T_{tail} L}{W} && (2.24)\\
&= \frac{52.962 \times 2.226 + 3.895 \times 4.73}{61.693} && (2.25)\\
&= 2.204m && (2.26)
\end{aligned}$$

where the average values $X_{COB} = 2.226m$ and $L = 4.73m$ were determined in Section 2.2.2. The computed distance of the CG from the nose indicates that it is slightly ahead of the center of buoyancy.

Since the airship remained horizontal in the above test, the vertical offset of the CG, Z_{CG}, did not factor into our equations. To estimate Z_{CG}, a similar experiment can be performed with the airship suspended at a large pitch or roll angle. With the airship still suspended at the nose and tail, it was rolled over to an angle of +90° and held in place by the FS15 force gauge attached to its gondola. A schematic of this configuration with relevant forces is shown below

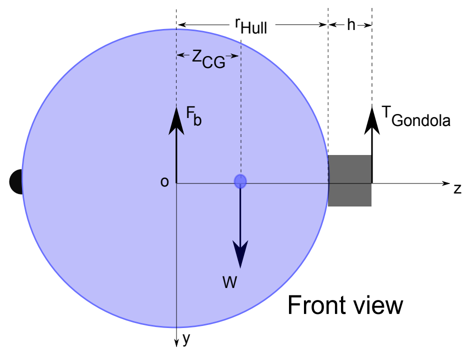

Figure 2–8: Free body diagram of fully rigged airship at +90° roll

$T_{Gondola}$ in Figure 2–8 is measured by the FS15 force gauge. h is the height of the gondola, and r_{Hull} is the radius of the airship hull at the gondola. A vertical force balance gives us W, the weight of the airship

$$W = F_b + T_{Gondola} \tag{2.27}$$

From a moment balance about the origin of the body-fixed frame o, Z_{CG} can be expressed as

$$Z_{CG} = \frac{T_{Gondola}(r_{Hull} + h)}{W} \tag{2.28}$$

where h was measured to be 0.135 m and r_{Hull} can be computed from the diameter at 3.5 $mBar$ in Table 2–2. The same procedure can be repeated for a roll angle of -90°. For both angles, a summary of the experimental measurements along with the computed weight W and vertical CG offset Z_{CG} is shown in Table 2–4.

The two values of Z_{CG} in Table 2–4 differ by only 4 mm and are in good agreement with each other. While the nose and tail of the suspended airship may not have been completely free of reaction forces and moments, they appear to have had little effect

Table 2–4: Roll CG test summary

Angle, deg	Scale reading, N	Weight, N	Z_{CG}, m
+90	9.02	61.982	0.127
-90	9.38	62.340	0.131

on the results. This can be verified through the average airship weight W (column 3) of 62.161 N which is very close to the values computed from equation (2.22) and in Table 2–3. From the average of column 4 in Table 2–4, the CG lies 12.9 cm below the COB.

2.2.5 CAD Model

A CAD model of the airship was constructed on Pro-Engineer Wildfire 3.0 using the hull profile defined in equation (2.21). The airship hull was modeled as two parts: an outer shell and an inner 'solid' body for the Helium. To create the outer shell model, a digital caliper was first used to measure the thickness of the hull material and it was found to be ≈0.091 mm thick. Unfortunately, Pro-Engineer was unable to create a shell with this thickness so a larger shell thickness had to be used instead. Through trial and error, it was found that a 1 mm shell was the minimum that Pro-Engineer could create. Although this is roughly 10 times larger than the actual thickness, it is still very small compared to the overall dimensions of the balloon. For this reason, the inertial properties of the thicker shell should still be representative of the actual hull.

Once the shell was created, a uniform density was assigned to it based on the mass of the deflated hull and the volume of shell material computed by Pro-Engineer. Due to their extremely low weight in relation to the total weight of the balloon, the Velcro patches and rigging hooks on the airship were not modeled and their weights were incorporated into the density of the hull material. The solid Helium model was created using the same profile as that of the hull and a density of 0.166 $\frac{kg}{m^3}$ (at 20°C) was assigned to it. The position of the airship's center of buoyancy was determined by calculating the center of gravity of the Helium model.

Accurate CAD models for the rapid prototyped components in the thrusters were provided by Quanser. The remaining parts of the thruster were modeled and densities were assigned so as to produce the measured masses of the parts. For the sake of simplicity, wiring on the thrusters was not modeled and the weights of wires were incorporated into neighbouring parts by adjusting their densities. Since the lithium polymer battery is roughly one third of the overall mass of the thruster, an effort was made to set its mount point on the thruster as accurately as possible. Finally, the four thruster models were positioned in the main assembly using the coordinates specified in Section 2.2.1. Figure 2–9 shows the modeled thruster assembly. One feature of the airship that could not be reproduced in the CAD model was the noticeable downward sag in the thrusters when mounted on the hull. A precise measurement of the thruster orientation is difficult since it changes based on the hull inflation pressure as well as the tension in the supporting lines.

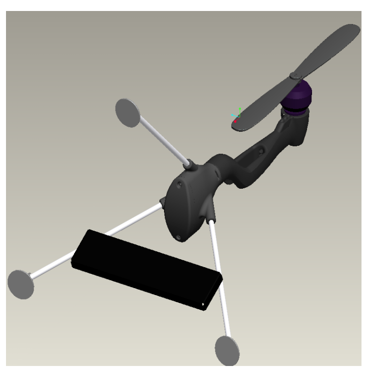

Figure 2–9: Thruster CAD model

The gondola, GPS antenna, and the antenna cable were modeled as solid parts with the masses shown in Table 2–3. A rendering of the final Pro-Engineer model is shown in Figure 2–10.

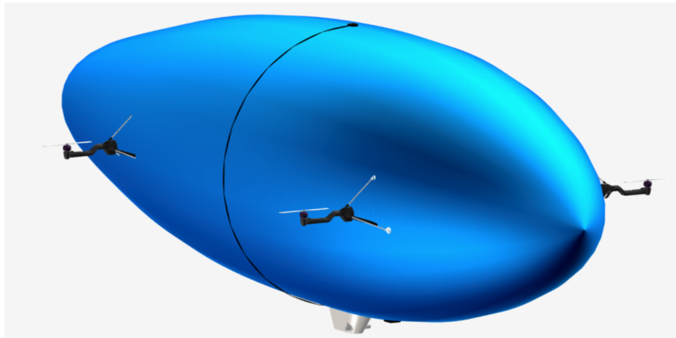

Figure 2–10: Final assembly

Comparison of CAD and Experimental Physical Parameters

The inertial properties of the airship CAD model were evaluated with respect to the body-fixed frame located at the center of buoyancy. Results from the computation are given in Table 2–5 along with a comparison to experimental values (wherever applicable). In order to facilitate comparison of the CAD model's CG location with experimental data, coordinates of the CG have been presented with respect to the nose and not the body-fixed frame.

We see that the overall mass of the CAD model is in close agreement with the experimental value computed from equation (2.22) and the average of the two is chosen for use in the simulation. Similarly, the CAD and experimental values of airship length are a good match, with the CAD value being slightly higher due to the manner in which the nose and tail are represented in the hull profile.

There is a relatively large 11.1% discrepancy in the internal volume and by extension, the gross buoyant lift. To determine the source of this error, we first examine the method used to obtain the hull profile at 3.5 $mBar$ (see Section 2.2.3). As mentioned in Section 2.2.1, the initial hull profile was measured using an older hull which was eventually replaced due to wear and tear. Since the airship hulls are fabricated by hand, there could be manufacturing differences in the form of differing dimensions

Table 2–5: Inertial properties from CAD model

Property	Units	CAD	Experimental	% difference
Mass(incl. Helium), m	kg	6.434	6.288	2.3
Length, L	m	4.805	4.730	1.6
Internal Volume, V	m^3	5.046	4.484	11.1
Gross Lift, F_b	N	59.600	52.980	11.1
COB Location (from nose), X_{COB}	m	2.268	2.226	1.9
CG distance from nose, X_{CG}	m	2.220	2.209	0.5
CG distance below nose, Z_{CG}	m	10.4×10^{-2}	12.9×10^{-2}	24
Diameter @ x=2.2 m from nose, $d_{2.2}$	m	1.480	1.480	0
Maximum Diameter, d_{max}	m	1.488	-	-
Inertias (incl. Helium)*				
I_{XX}	$kg \cdot m^2$	3.125	-	-
I_{YY}	$kg \cdot m^2$	8.077	-	-
I_{ZZ}	$kg \cdot m^2$	9.115	-	-
I_{XY}, I_{YX}	$kg \cdot m^2$	4.456×10^{-3}	-	-
I_{YZ}, I_{ZY}	$kg \cdot m^2$	-2.186×10^{-3}	-	-
I_{ZX}, I_{XZ}	$kg \cdot m^2$	-8.418×10^{-2}	-	-

*-Helium treated as rigid body attached to envelope

from one hull to the other. By scaling the profile of the older hull using one reference diameter (2.2 m behind the nose), we are not guaranteed to get an accurate representation of the new hull at 3.5 $mBar$. The scaled profile could very well overestimate the internal volume. This is supported by the data in Table 2–2, which shows that even at the highest pressure, the airship's internal volume is less than the CAD value. Part of this difference might also originate from errors in computing the airship's internal volume from experimental data. From equation (2.16) in Section 2.2.2, recall that the airship volume is given by

$$\begin{aligned} V &= \frac{T_{nose} + T_{tail} + W_{Hull}}{(\rho - \rho_{He})g} \\ &= \frac{T_{nose} + T_{tail} + T'_{nose} + T'_{tail}}{(\rho - \rho_{He})g} \end{aligned} \tag{2.29}$$

where T'_{nose} and T'_{tail} are the scale readings from which W_{Hull} was computed. The internal volume at 3.5 $mBar$ in Table 2–2 was computed using $\rho_{He} = 0.166\ \frac{kg}{m^3}$ at $20^\circ\ C$. If we assume that the Helium gas was at a much lower temperature, and use the density of Helium at $0^\circ\ C$, $\rho_{He} = 0.1786\ \frac{kg}{m^3}$, the resulting volume is only 1.1% higher. Temperature effects alone cannot explain the 11.1% discrepancy. Errors in the fish scale readings in the numerator of equation (2.29) could also introduce an error in the airship volume. But calibration tests on the FS15 force gauge showed that its readings were off by 2-3%, at most. It is therefore unlikely that the scales could have caused the 11.1% difference. Since the experimental errors cannot explain the observed discrepancy, and considering that the CAD volume is most probably over-estimated, we use the average of the CAD and experimental volumes in the simulation.

The $\approx$4 cm difference in the COB location between the CAD and experiment is acceptable in view of the discrepancy in the airship length and the possibility of experimental errors.

While the CAD value of the CG's longitudinal position showed good agreement with the experiment, the vertical position was off by around 2.5 cm. When compared to the maximum radius of the airship ($\approx$ 75 cm), this difference is relatively small. It is most likely due to errors in the position and orientation of the thrusters in the CAD model. The lateral offset of the CG is assumed to be zero.

Although the lifting gas adds to the inertia of the airship, Pro-Engineer tends to over-estimate its contribution by treating the Helium as a solid mass. As a compromise, we use the average of the inertias from the CAD model with and without the Helium.

Table 2–6 contains the physical parameters that were used in the simulation. Column 4 indicates the source of the chosen value: '*Exp*' denotes the experimental value, 'CAD' denotes the CAD value, and 'Avg' denotes an average of the CAD and experimental values.

Table 2–6: Inertial properties used in dynamics model

Property	Units	Value	Source
Mass(incl. Helium), m	kg	6.346	Avg
Length, L	m	4.768	Avg
Internal Volume, V	m^3	4.765	Avg
Gross Lift, F_b	N	56.29	Avg
COB Location (from nose), X_{COB}	m	2.247	Avg
CG distance from nose, X_{CG}	m	2.215	Avg
CG distance below nose, Z_{CG}	m	11.65×10^{-2}	Avg
Maximum diameter, d_{max}	m	1.488	CAD
Inertias			
I_{XX}	$kg \cdot m^2$	3.038	CAD
I_{YY}	$kg \cdot m^2$	7.627	CAD
I_{ZZ}	$kg \cdot m^2$	8.665	CAD
I_{XY}, I_{YX}	$kg \cdot m^2$	4.456×10^{-3}	CAD
I_{YZ}, I_{ZY}	$kg \cdot m^2$	-2.186×10^{-3}	CAD
I_{ZX}, I_{XZ}	$kg \cdot m^2$	-8.418×10^{-2}	CAD

2.2.6 Estimation of Added Mass and Inertia Matrices

We can estimate the added mass and inertia matrices $\boldsymbol{A}_m$ and $\boldsymbol{A}_J$ in equation (2.5) by treating the airship hull as an ellipsoid of revolution and using the method described in [44]. If the body-fixed frame is located at the center of buoyancy, the off-diagonal terms in both matrices become zero and we can define them as follows

$$\boldsymbol{A}_m = \begin{bmatrix} m_{11} & 0 & 0 \\ 0 & m_{22} & 0 \\ 0 & 0 & m_{22} \end{bmatrix} \tag{2.30}$$

where m_{11} is the added mass of the airship hull in the longitudinal direction (x axis), and m_{22} is the added mass in the lateral directions (y and z).

$$\boldsymbol{A}_J = \begin{bmatrix} 0 & 0 & 0 \\ 0 & m_{33} & 0 \\ 0 & 0 & m_{33} \end{bmatrix} \tag{2.31}$$

where the added inertia about the roll axis is assumed to be zero and m_{33} is the added inertia about the pitch and yaw axes. In equations (2.30) and (2.31), $m_{11} = k_1 m_D$, $m_{22} = k_2 m_D$, and $m_{33} = k_3 I_D$. m_D and I_D are the mass and rotational inertia (about the body-fixed y/z axis) of the displaced air respectively. Using the airship volume in Table 2–6 and an air density $\rho = 1.204\ \frac{kg}{m^3}$, the mass of displaced air is $m_D = 5.7371\ kg$. The hull profile in equation (2.21) is used to compute the rotational inertia of the displaced air, $I_D = 6.769\ kg.m^2$. The added mass factors k_1, k_2 and k_3 depend on the fineness ratio of the hull and can be determined from the plot in Figure 2–11, which has been reproduced from Li[31]. The airship length and maximum diameter listed in Table 2–6 yield a fineness ratio $\frac{L}{d_{max}} = \frac{4.768}{1.488} = 3.204$. Using this fineness ratio and the values of m_D and I_D mentioned above, the added mass and inertias are $m_{11} = 0.638\ kg$, $m_{22} = 4.693\ kg$, and $m_{33} = 3.389\ kg \cdot m^2$. While the longitudinal added mass term m_{11} is relatively low, the lateral term m_{22} is nearly 74% of the airship's total mass.

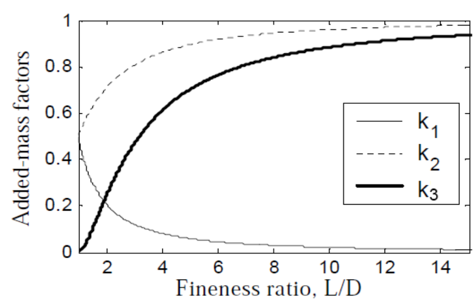

Figure 2–11: Added mass factors versus fineness ratio (L/D)[31].

2.3 Viscous Hull Forces

This section discusses calculation of the aerodynamic force and moment acting on the airship hull. Specifically, in equation (2.4), we require estimates for the terms $\boldsymbol{f}_V$, the aerodynamic force, and $\boldsymbol{n}_V$, the aerodynamic moment as a function of the airship's angle-of-attack. High angle-of-attack aerodynamic characteristics of airship hulls are, in general, difficult to model due to the complex airflow generated under such conditions. Lutz *et al.*[22] analyzed a bare hull of the Lotte airship at angles of attack up to 30° and noted that viscous flow about an inclined hull is characterized by shear layers separation from the airship surface. Ericsson and Reding[45] provide a similar description of the flow about a slender body of revolution with an increasing angle of attack. They state that close to 0°, the flow is mostly axial and remains attached to the hull. In contrast, at 90° crossflow over the hull is dominant, similar to a cylinder placed normal to an oncoming flow. At intermediate angles, vortex pairs are shed that become increasingly asymmetric as the angle of attack increases.

For the purpose of the airship model being developed, we use a semi-empirical method of computing the steady-state aerodynamic coefficients by Jorgensen[34] that is similar to the work by Allen and Perkins[29]. It can be extended to the entire 360° range of angles of attack and is hence suitable for our needs. However, Jorgensen's method does not take into account the above-mentioned unsteady loads produced by vortex shedding at high angles of attack. The method also does not provide a way to calculate the rotational damping due to the the angular velocity of the airship. Since we do not expect the MkII to perform maneuvers with large pitch or yaw rates, this should not have a significant impact in the simulation.

2.3.1 Jorgensen's Equations

Jorgensen's equations for normal force, axial-force and pitching-moment coefficient (about a distance x_m from the nose) are given below:

$$C_N = \frac{A_b}{A} sin2\alpha' cos\frac{\alpha'}{2} + \eta C_{d_n} \frac{A_p}{A} sin^2\alpha'; \quad 0^\circ \leq \alpha \leq 180^\circ \tag{2.32}$$

$$C_A = C_{A_{\alpha=0^\circ}} cos^2\alpha'; \quad 0^\circ \leq \alpha \leq 90^\circ \tag{2.33}$$

$$C_A = C_{A_{\alpha=180^\circ}} cos^2\alpha'; \quad 90^\circ \leq \alpha \leq 180^\circ \tag{2.34}$$

$$C_M = \left[\frac{V - A_b(l - x_m)}{Ad}\right] sin2\alpha' cos\frac{\alpha'}{2} + \eta C_{d_n} \frac{A_p}{A} \left(\frac{x_m - x_p}{d}\right) sin^2\alpha'; \quad 0^\circ \leq \alpha \leq 90^\circ \tag{2.35}$$

$$C_M = -\left[\frac{V - A_b x_m}{Ad}\right] sin2\alpha' cos\frac{\alpha'}{2} + \eta C_{d_n} \frac{A_p}{A} \left(\frac{x_m - x_p}{d}\right) sin^2\alpha'; \quad 90^\circ \leq \alpha \leq 180^\circ \tag{2.36}$$

where the angle of attack $\alpha' = \alpha$ for $0^\circ \leq \alpha \leq 90^\circ$ and $\alpha' = 180^\circ - \alpha$ for $90^\circ \leq \alpha \leq 180^\circ$. A_b is the base area of vehicle, A is the frontal area, and A_p is the planform area of the hull. η is the crossflow efficiency factor and C_{dn} is the crossflow drag coefficient. $C_{A_{\alpha=0^\circ}}$ and $C_{A_{\alpha=180^\circ}}$ are the axial drag coefficients at 0° and 180° angles of attack. V is the internal volume of the airship, l is the airship length, d is the airship's maximum diameter, x_m is the distance behind the nose about which the pitching moment is computed, and x_p is the center of the hull's planform area.

The first term in equations (2.32),(2.35) and (2.36) is derived from Munk's[28] formulation of the normal force generated by potential flow over a slender body. In Munk's work, the added mass of a body is taken into account by multiplying the potential flow term by the difference of the lateral and longitudinal added mass factors, $(k_2 - k_1)$. Jorgensen does not include this factor in his potential flow terms since his test bodies were of high fineness ratio for which $(k_2 - k_1) \approx 1$. Since the MkII's hull has a relatively low fineness ratio, we shall append this factor to the potential flow terms in Jorgensen's equations i.e., the first term on the right hand side of equations (2.32),(2.35) and (2.36) are multiplied by (k_2 - k_1).

The second term in equations (2.32),(2.35) and (2.36) computes loads due to viscous crossflow caused by separation of the airflow over the body. η is a factor to account for the finite length of the body. Knowing the ratio of the airship's length(L) to its maximum diameter(d_{max}), η can be determined from the graph in Figure 2–12. C_{d_n} is the drag coefficient of an 'infinite' cylinder placed normal to the flow. Figure 2–13 shows Jorgensen's crossflow drag model for circular cylinders at sub-critical Mach numbers. The crossflow Reynolds number is given by

$$Re_{cross} = \frac{V_{cross} d_{max}}{\nu} \tag{2.37}$$

where the kinematic viscosity of air at 20°C, $\nu = 14.813 \times 10^{-6} \frac{m^2}{s}$ and $V_{cross} = \sqrt{v_{ac}^2 + w_{ac}^2}$

The normal force acts at a distance x_{ac} from the nose defined as follows

$$x_{ac} = \left(\frac{x_m}{d} - \frac{C_M}{C_N} \right) d \tag{2.38}$$

where x_m is the distance from the nose about which the pitching moment is computed. In our simulation, we set this point at the center of buoyancy. C_N and C_M are calculated from (2.32) and either one of (2.35) or (2.36) (depending on the angle of

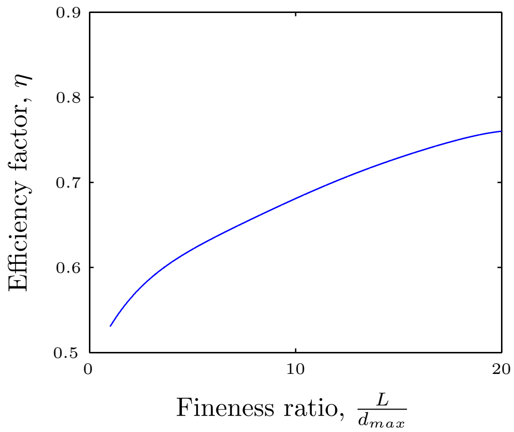

Figure 2–12: Hull efficiency factor

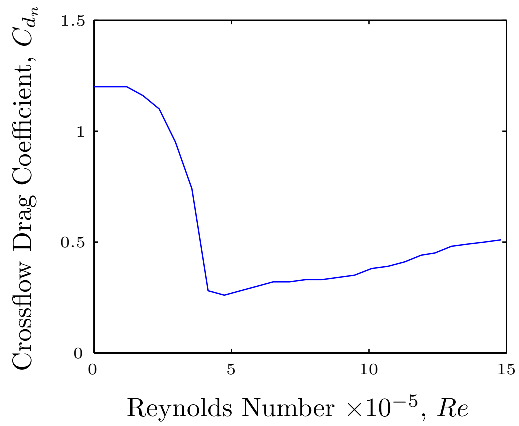

Figure 2–13: Crossflow drag coefficient

attack). In the case of an axisymmetric body of revolution, x_{ac} lies on the longitudinal axis. x_{ac}'s location can now be expressed with respect to the pitching-moment center

$$x'_{ac} = x_m - x_{ac} = x_m - \left(\frac{x_m}{d} - \frac{C_M}{C_N}\right) d = \frac{C_M}{C_N} d \tag{2.39}$$

The angle of attack α in equations (2.32)-(2.36) is determined from the velocity components at the aerodynamic center. If the airship has a velocity $\boldsymbol{v}$=$[u, v, w]$, angular velocity $\boldsymbol{\omega}$=$[p, q, r]$ and is subject to a wind speed $\boldsymbol{v}_w$=$[u_w, v_w, w_w]$ expressed in the body-fixed frame, the velocity at x_{ac} is calculated from:

$$\boldsymbol{v_{ac}} = [u_{ac}\ v_{ac}\ w_{ac}] = (\boldsymbol{v} - \boldsymbol{v}_w) + \boldsymbol{\omega} \times \boldsymbol{r}_{ac} \tag{2.40}$$

where the position vector of the aerodynamic center is $\boldsymbol{r}_{ac} = [x'_{ac}\ 0\ 0]$. The angle of attack, depicted graphically in Figure 2–14, can then be expressed as:

$$\alpha = tan^{-1} \frac{\sqrt{v_{ac}^2 + w_{ac}^2}}{u_{ac}} \tag{2.41}$$

A_b represents the base area of the body under consideration and for a closed profile such as that of an airship hull, it has a value of zero. It can be shown that by setting $A_b = 0$ in (2.35) and (2.36), the resulting moment contribution from potential flow at

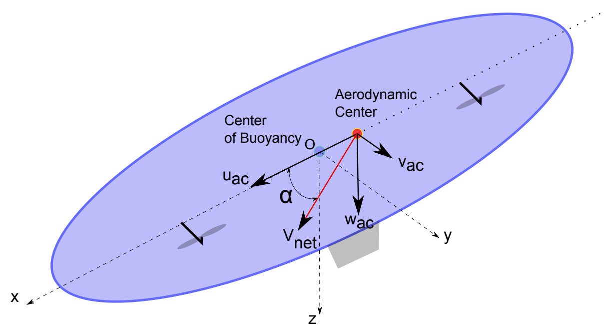

Figure 2–14: Angle of attack and aerodynamic center velocity components

low angles of attack is equivalent to the destabilizing Munk moment term discussed in Section 2.1. Since the Munk moment has already been accounted for in the derivation of equations of motion, we can omit it from (2.35) and (2.36). Furthermore, equation (2.32) indicates that a base area $A_b = 0$ nullifies the potential flow contribution to the normal force leaving only the viscous crossflow drag term which is proportional to $sin^2\alpha'$. Jorgensen's original equations can now be reduced to:

$$C_N = \eta C_{d_n} \frac{A_p}{A} sin^2\alpha'; \quad 0^\circ \leq \alpha \leq 180^\circ \tag{2.42}$$

$$C_A = C_{A_{\alpha=0^\circ}} cos^2\alpha'; \quad 0^\circ \leq \alpha \leq 90^\circ \tag{2.43}$$

$$C_A = C_{A_{\alpha=180^\circ}} cos^2\alpha'; \quad 90^\circ \leq \alpha \leq 180^\circ \tag{2.44}$$

$$C_M = \eta C_{d_n} \frac{A_p}{A} \left(\frac{x_m - x_p}{d} \right) sin^2\alpha'; \quad 0^\circ \leq \alpha \leq 180^\circ \tag{2.45}$$

where $\alpha' = \alpha$ for $0^\circ \leq \alpha \leq 90^\circ$ and $\alpha' = 180^\circ - \alpha$ for $90^\circ \leq \alpha \leq 180^\circ$. Using equations (2.42) and (2.45) in (2.39), the location of the aerodynamic force center with respect to the pitching moment center gets simplified to the following constant value

$$\begin{aligned} x'_{ac} &= \left[\frac{\eta C_{d_n} \frac{A_p}{A} \left(\frac{x_m - x_p}{d} \right) sin^2 \alpha'}{\eta C_{d_n} \frac{A_p}{A} sin^2 \alpha'} \right] d \\ &= x_m - x_p \end{aligned}$$

which simply states that the aerodynamic center of the viscous hull force is the center of the hull planform.

2.3.2 Adapting Jorgensen's Equations to Quanser MkII ALTAV

Although the MkII does not have a constant cross-sectional area along its hull, the area of the cylindrical section A is calculated using the maximum hull diameter listed in Table 2–6. The planform area(A_p), and centroid of the planform area(x_p) are estimated from the mathematical description of the hull profile. The pitching moment center x_m is set at the center of buoyancy. d is set to the maximum diameter of the airship. Jorgensen provides a method of calculating the zero-angle axial drag coefficient C_A in equations (2.33) and (2.34) by adding contributions from skin-friction, and pressure at the nose and base of the body. However, we choose not to use his method since it is intended for use with blunt-based bodies and would likely overestimate the drag for the MkII's streamlined hull. Instead, data from Hoerner[47] is used in which the drag coefficients are calculated based on the frontal area as a function of the airship's fineness ratio. It is also assumed that the drag coefficient at 0° is equal in magnitude to 180°. The axial drag coefficient will most likely need to be tuned by flight test data since the protruding thruster arms and gondola also contribute to the form drag of the airship. A summary of the geometric parameters used in equations (2.42)-(2.45) is presented in Table 2–7.

Table 2–7: Values of geometric parameters in hull force equations

Parameter	Value
Planform Area, A_p	5.229 m^2
Reference Area, A	1.740 m^2
Overall Length, l	4.768 m
Pitching Moment Center, x_m	2.247 m
Centroid of Planform Area, x_p	2.323 m
Reference Diameter, d	1.489 m
Axial Drag Coefficient, C_A	0.041

Resolving forces in body-fixed frame

The normal force coefficient in (2.42) is converted to a force by multiplication with the dynamic pressure q_0 and reference area A:

$$N = q_0 A C_N \tag{2.46}$$

The angle of attack α computed from equation (2.41) ranges from 0° to 180°. The 180° to 360° range can be accounted for by decomposing the normal force along the body-fixed y and z axes as follows:

$$f_{V_y} = \frac{-N v_{ac}}{\sqrt{v_{ac}^2 + w_{ac}^2}}, \qquad f_{V_z} = \frac{-N w_{ac}}{\sqrt{v_{ac}^2 + w_{ac}^2}} \tag{2.47}$$

The axial drag force can be computed by:

$$\begin{aligned} f_{V_x} &= -q_0 C_A cos^2\alpha; \quad u_{ac} \geq 0 \\ f_{V_x} &= q_0 C_A cos^2\alpha; \quad u_{ac} \leq 0 \end{aligned} \tag{2.48}$$

Equation (2.48) is valid for the 0° to 360° range. When the aerodynamic center has a positive forward speed, the vehicle experiences a drag force in the -ve x direction and vice versa.

Similarly, the pitching moment M about the center of buoyancy can be determined by multiplying (2.45) with the dynamic pressure q_0, reference area A and reference length (maximum hull diameter) d.

$$M = q_0 A d C_M \tag{2.49}$$

Resolving M along the y and z axes we get:

$$n_{V_y} = \frac{M w_{ac}}{\sqrt{v_{ac}^2 + w_{ac}^2}}, \qquad n_{V_z} = \frac{-M v_{ac}}{\sqrt{v_{ac}^2 + w_{ac}^2}} \tag{2.50}$$

For the time being, we have assumed that there are no aerodynamic moments associated with rolling motion, hence $n_{v_x} = 0$. Writing out the force and moment terms as vectors:

$$\boldsymbol{f}_V = \begin{bmatrix} f_{V_x} \\ \frac{-q_0 A C_N v_{ac}}{\sqrt{v_{ac}^2 + w_{ac}^2}} \\ \frac{-q_0 A C_N w_{ac}}{\sqrt{v_{ac}^2 + w_{ac}^2}} \end{bmatrix}, \qquad \boldsymbol{n}_V = \begin{bmatrix} 0 \\ \frac{q_0 A d C_M w_{ac}}{\sqrt{v_{ac}^2 + w_{ac}^2}} \\ \frac{-q_0 A d C_M v_{ac}}{\sqrt{v_{ac}^2 + w_{ac}^2}} \end{bmatrix} \tag{2.51}$$

At each simulation time step, the force and moment terms $\mathbf{f}_V$ and $\mathbf{n}_V$ are evaluated from the translational and angular velocities of the airship, and the body-fixed wind components. The viscous drag contribution is then incorporated into the equations of motion by substituting $\mathbf{f}_V$ and $\mathbf{n}_V$ from equation (2.51) into equation (2.4).

CHAPTER 3
Thruster Model

This chapter describes the modeling of the MkII's vectorable thrusters based on data from lab tests. Each of the MkII's thrusters is comprised of a brushless motor and propeller unit as well as a system to tilt that unit, and hence the thrust vector. With a total of eight (4 thrust magnitudes and 4 tilt angles) independent control inputs available, the relatively small MkII is capable of executing quick and precise maneuvers. However, before we can design flight controllers, we first need to characterize the capabilities of its vectored thrusters. It is well known that transient thruster behavior becomes more significant as the speed of a vehicle's dynamics approaches that of its thrusters. Considering the MkII's inherently maneuverable design, it is possible that its behavior will be heavily influenced by the thruster's dynamics. Because of this, special attention will be paid to capturing the thruster's transient characteristics in this chapter. In the following section, the MkII's thruster sub-system is discussed along with pertinent specifications of its components. Thereafter, the chapter is divided into two parts, the first of which discusses identification and validation of the thrust dynamics. In the second part, a model of the thrust vectoring system is developed and validated.

3.1 System Description

The thruster sub-assembly (shown in Figure 3–1) provides vectorable thrust to the MkII airship. It includes the brushless motor and propeller, electronic speed controller, servo motor, and battery. A three legged base houses the servo motor which connects to a rotating arm through a bearing. The electronic speed controller and

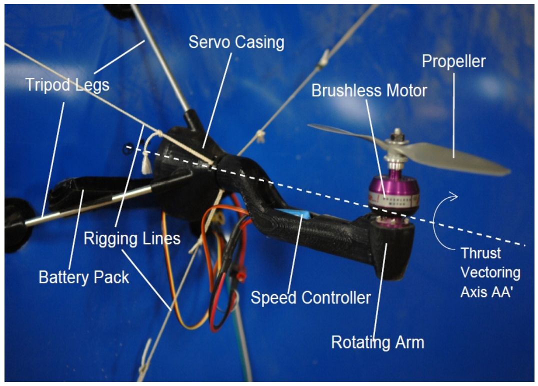

Figure 3–1: Quanser MkII Thruster.

brushless motor are both mounted on this arm and vectoring of thrust in flight is achieved by tilting the arm about axis AA' while keeping the base stationary. The rotating arm and the base were fabricated by rapid prototyping since the thermoplastic material used is extremely light and provides reasonable strength for normal flight operation. The entire assembly is attached to the airship by Velcro pads on the legs of the tripod base as well as three rigging lines whose tension can be adjusted individually.

The increasing popularity of recreational radio-controlled aircraft flying has led to the availability of a variety of brushless motors, servos and battery packs to satisfy any price/performance requirement. This makes it possible to use commercially available off-the-shelf components in the four vectored thrusters on the Quanser MkII. Thrust is generated by a PJS 3D-1000N (Figure 3–3) brushless motor paired with an APC 0.305 m(12") diameter x 0.1 m(3.8") constant pitch propeller. Compared to conventional brushed motors, brushless motors offer higher efficiency, and longer life due to the absence of brushes, which get worn out over time. The 3D-1000N has a K_v motor constant of 1240 rpm per Volt and is most efficient at a current of 26 A [48].

Figure 3–2: Jeti Advance 30-Plus Speed Controller.

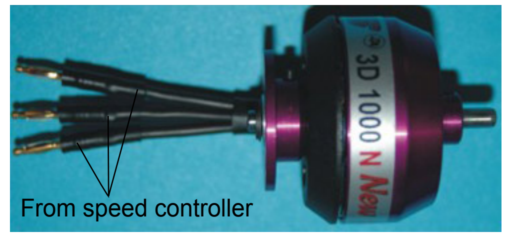

Figure 3–3: PJS 3D-1000N Motor.

A JETI Advance 30 Plus electronic speed controller(ESC)(Figure 3–2) is used to drive the PJS 3D-1000N. It can supply a maximum of 30 Amperes continuously to the brushless motor. The input to the speed controller is a 50 Hz square-wave pulse in which the width of the pulse is changed to vary the voltage applied to the motor, and hence its speed; a technique commonly known as Pulse Width Modulation (PWM). In the present setup, this pulse is generated by a microcontroller on board the airship based on a normalized input from 0 to 1. The width of pulse sent to the speed controller varies linearly with the normalized input as shown in Figure 3–4.

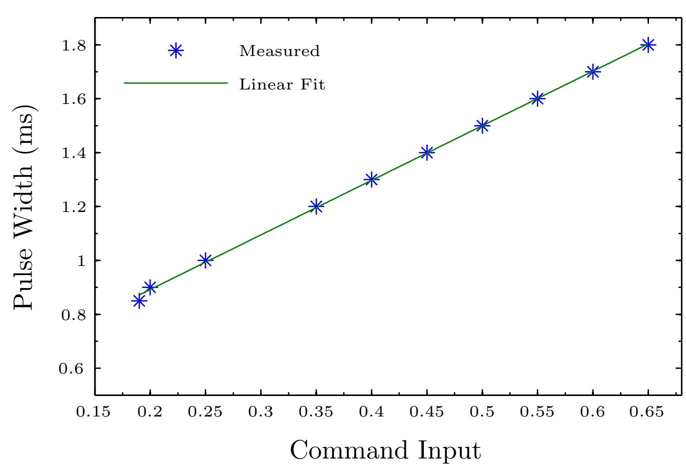

Figure 3–4: Pulse width (ms) as a function of normalized input.

The Jeti Advance 30 plus speed controller has a safety feature which prevents the 3D-1000N brushless motor from spinning immediately after the battery is connected.

In order to run the motor, the speed controller must first be sent a PWM signal of width 0.75 ms (command input of 0.13). Upon receiving this signal, the ESC emits a beep indicating that the motor is ready to run. This process is referred to as 'arming'. Once the ESC is armed, the motor's speed can be varied by sending the commands shown in Figure 3–4. The output from the speed controller is a polyphase current which powers each winding of the brushless motor in sequence to reach a desired speed. One drawback of the Advance 30 Plus is that the motor's direction of rotation cannot be reversed without physically switching two of the three current carrying wires going to the motor. A 12.64 V, 4000 mAh ThunderPower lithium polymer battery pack powers the speed controller and brushless motor. It is rated to provide a maximum continuous current of 48 A and short bursts up to 72 A.

Vectoring of thrust is provided by a Hitec HS-322HD analog servo motor (shown in Figure 3–5) which is housed in the servo casing (shown in Figure 3–1). Similar to the electronic speed controller, the servo accepts a PWM input to set the desired angle of the output shaft. The HS-322HD can be driven up to $\pm 90°$ from its neutral (vertical thrust) position with the input pulse widths shown in Figure 3–6. Using the information in Figure 3–6, the linear relationship between the input pulse width and servo angle can be written as follows

$$\beta_{des} = 100(PW - 0.6) - 90 \tag{3.1}$$

where PW is the input pulse width and β_{des} is the desired angle of the servo's output shaft in degrees measured from the vertical. The servo is powered by a circuit on the Advance 30 Plus electronic speed controller, which supplies 5 V through the signal input cable shown in Figure 3–2. When powered with a $5V$ DC power supply, the HS-322HD is rated to generate a maximum torque of around 0.3 $N \cdot m$ and has a maximum speed of $\approx 316 \frac{deg}{s}$ when not loaded.

Figure 3–5: Hitec HS-322HD servo motor.

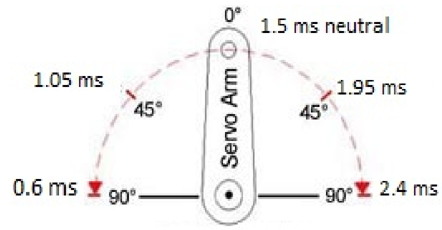

Figure 3–6: Variation of servo angle with input pulse width.

3.2 Thrust Motor Model

The first part of the thruster dynamics model focuses on the subsystem that generates thrust, which consists of the brushless motor, electronic speed controller, and Lithium polymer battery. From a modeling point of view, the speed controller adds a dimension of complexity since it contains digital circuits that regulate the power being delivered to the brushless motor. In light of this, the modeling approach for the thruster dynamics described herein relies solely on data from lab tests to determine its steady-state and transient characteristics. Steady-state tests are used to identify two aspects important to real-world operation of the thruster, namely: the static thrust available for a given motor speed and the *maximum* thrust that can be generated with the current hardware configuration. The latter will be a limiting factor in the MkII's ability to cope with winds. For the transient part of the thruster dynamics model, we deduce characteristics such as the time constant and bandwidth of the thrust response from experimental data. In the following section, the setup that was used to collect this data from the thruster is discussed.

3.2.1 Experimental Setup

The detailed description of the MkII's thruster in Section 3.1 lays the groundwork for the experimental setup used in its characterization. In order to identify of the thruster dynamics, experimental force-torque data was collected from the brushless motor. Clearly, carrying out tests with a thruster mounted on the inflated airship hull is impractical and more controlled laboratory tests were preferred. To minimize the experiment's design and setup complexity, an effort was made to use (wherever possible) components of the thruster and airship as-is. Figure 3–7 depicts the important parts of the experimental setup used.

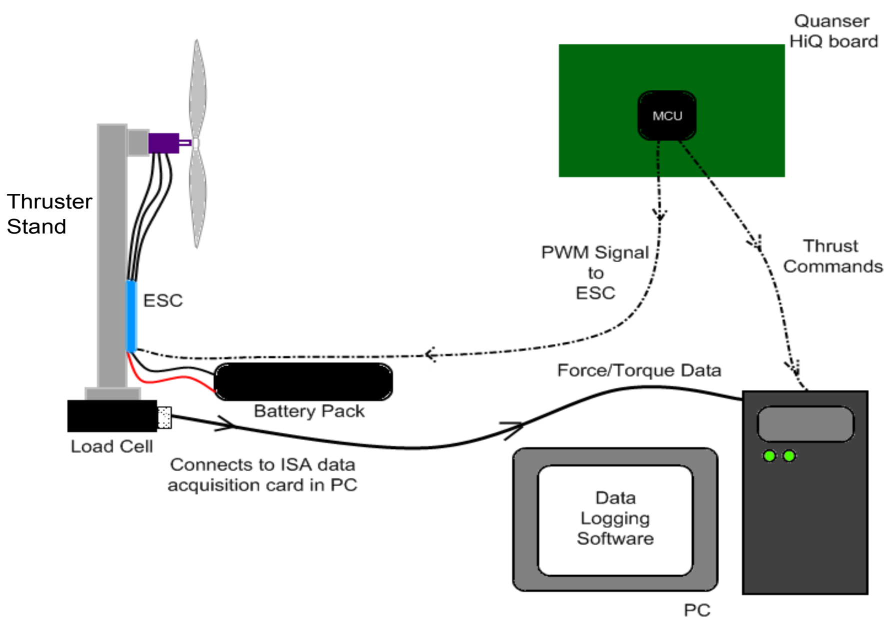

Figure 3–7: Schematic of experimental setup.

1. **Thruster stand** - To securely mount the electronic speed controller (ESC) and motor during experiments. Transmits forces and moments to attached load cell.
2. **Load cell** - ATI Gamma F/T transducer attached to base of thruster stand measures forces and moments generated by thruster. Interfaces with ISA bus data acquisition card in PC.
3. **Quanser HiQ board** - Airship avionics board used to send command signals to the ESC.

4. **PC** - Desktop personal computer that interfaces with load cell and Quanser HiQ board to log force/torque and thrust inputs respectively.

Load Cell(Force/Torque Sensor)

Figure 3–8: ATI Gamma Force-Torque sensor.

An ATI Gamma force-torque transducer was used in the experiments due to its large measurement ranges of ± 65 N in the x/y (horizontal) direction and ± 200 N in the z (vertical) direction. It can also measure moments up to 5 $N \cdot m$ about its x,y and z axes. The Gamma has a low resolution of $\frac{1}{40}$ N for the x and y axes and $\frac{1}{20}$ N for the z axis. These features combined with a high signal-to-noise ratio, stiffness and easy to use logging software make it an ideal choice for the experiments to be conducted.

Thruster Stand

Rapid prototyped parts such as the MkII thruster arm are susceptible to shear failure along the thermoplastic layers in addition to being vulnerable to impacts. In order to avoid subjecting the thruster to undue loads while testing, a simple stand was constructed to hold the motor and transmit its forces to the attached load cell. It can be seen in Figure 3–9 attached to the load cell, which itself was bolted to a sturdy bench. A 3.18 cm diameter aluminum rod was used to construct the 40 cm long stem of the stand. This length gave sufficient clearance between the tips of the spinning propeller and the bench on which the apparatus was mounted. The base of the stand was bolted to the F/T sensor (Figure 3–10) thus creating a strong and

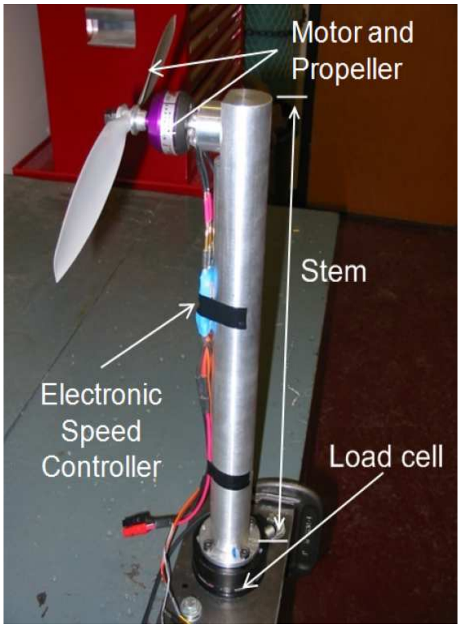

Figure 3–9: Thruster stand.

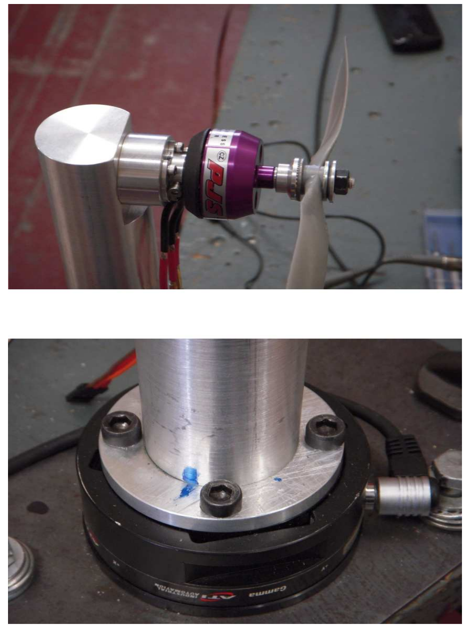

Figure 3–10: Motor and propeller mounted (Top) Base of thruster stand (Bottom).

rigid connection between the two. The motor was bolted to the top of the stand with its thrust axis oriented along the y axis of the transducer. Calibration tests at high thrust levels showed that the x component of the load cell output was insignificant compared to y, indicating that the alignment had little to no error.

Quanser HiQ Board

The HiQ board is a versatile control board for unmanned aerial vehicles (UAVs) developed by Quanser Control Inc. It is equipped with two processors, the first of which is an 8051 microcontroller to handle the low-level UAV functions such as processing sensor data and attitude control. The second processor is an Intel PXA255 that manages the high-level functions such as data logging, mission planning and Wi-Fi communication with the ground station. In the thruster characterization experiments being performed, the 8051 microcontroller was used to perform the following functions:

1. Send user-specified thrust commands in the form of PWM signals to the electronic speed controller.
2. Send thrust commands mentioned in 1) through serial port to desktop personal computer for logging purposes.
3. Record time history of battery voltage during experiments.

Desktop Personal Computer

A desktop personal computer was used to log and synchronize data from the force-torque sensor and HiQ board. Software provided by ATI Industrial Automation was used to configure the force-torque sensor and log incoming data to text files. The maximum rotation speed of the motor being used is approximately 10000 rpm. For a two bladed propeller rotating at this speed, the thruster stand would be subject to a oscillating force at a frequency of $2 \times \frac{10000}{60} = 334\ Hz$. In order to avoid aliasing in the sampled data, load cell data would need to be sampled at least five times faster (1670 Hz). A sampling frequency of 1953 Hz was set through the ATI software interface. However, after averaging the sample rate achieved over several tests, it was found that the value was actually closer to 1934 Hz. Despite the large volume of incoming data, no problems were encountered with buffering and writing operations. Because of a limitation in the software provided by ATI, timestamps for the transducer data had to be deduced during post-processing by utilizing the start time of logging and the sampling rate of 1934 Hz.

The 8051 microcontroller on the HiQ board was interfaced through a serial port on the desktop computer to log the thrust command signal being sent to the electronic speed controller in real-time. A simple serial data logger was written in Visual Basic to receive float values from the microcontroller and store them with a timestamp appended. Timestamps were generated using the *GetTickCounter()* timer in Windows XP, which returns the time elapsed since the computer was turned on. Unfortunately, it only has a resolution of 16 milliseconds so two or more thrust commands being received within 16 milliseconds of each other were assigned the same timestamp.

3.2.2 Test Results

Speed Measurements

Recall from Section 3.1 that a PWM input to the electronic speed controller is generated by the HiQ board's 8051 microcontroller based on a normalized input value (henceforth referred to as the 'command input'). However, it would also be useful to relate the thruster dynamics to physical quantities such as motor speed. Using a handheld analog tachometer, measurements were taken to determine the motor speed for a variety of command inputs. A plot of the measured values is shown in Figure 3–11. Once the tachometer is started, a reading is only obtained

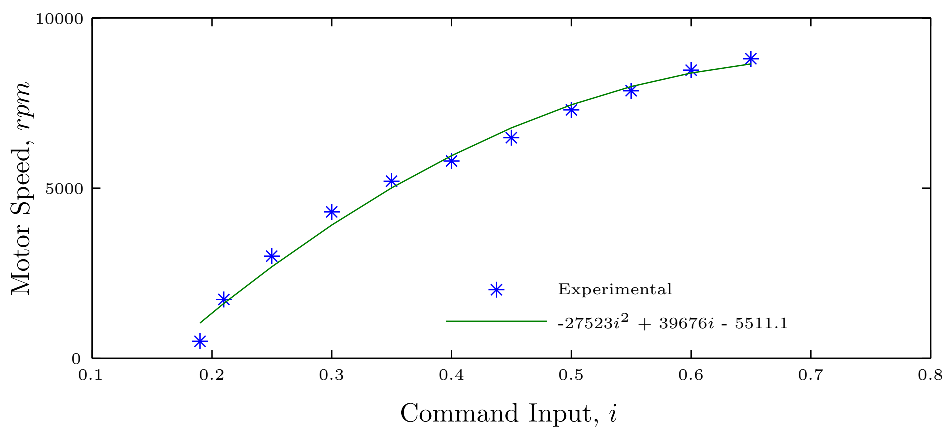

Figure 3–11: Output pulse width (ms) as a function of command input.

after six seconds thus constraining its use to steady-state testing with no changes in speed. Figure 3–4 shows that the lowest command input of 0.19 (idle) runs the motor at 500 rpm with a maximum speed of 8800 rpm being reached at an input of 0.65. It can be seen from the trend line that the motor speed is roughly a quadratic function of the command input. The data from Figure 3–11 and Figure 3–4 has been

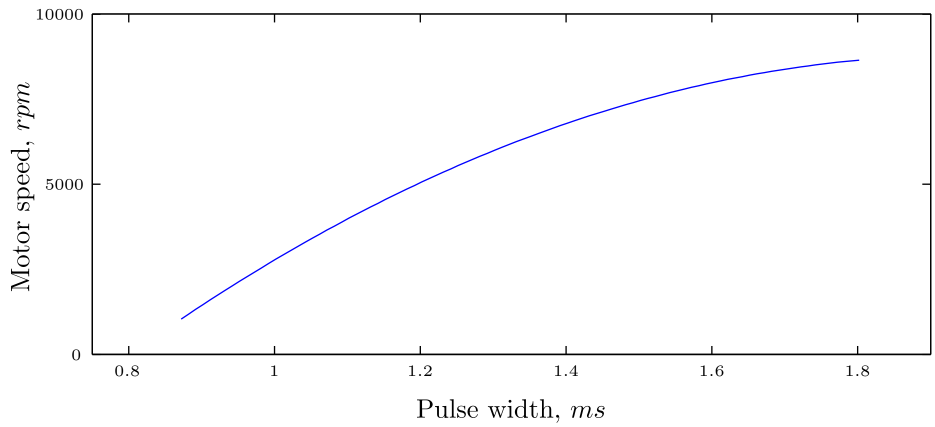

Figure 3–12: Motor speed (*rpm*) as a function of pulse width (*ms*) of input signal.

combined to generate the plot of motor speed versus pulse width shown in Figure 3–12. For reasons explained in the following section, these speed measurements become less accurate at higher command inputs and should therefore only be regarded as an approximation to the actual motor speed.

Step Responses

The first stage in identifying the thruster's dynamics was to determine the steady state thrust produced for a given input to the speed controller. To this end, a number of step command inputs were sent to the speed controller and force-torque transducer data was recorded for each run. Upon plotting data logged using the experimental setup discussed in Section 3.2.1, it was observed that the thrust commands from the HiQ board were delayed by a small amount with respect to the load cell data. An example of this lag is shown in Figure 3–13. It is believed that this offset was caused by a combination of delays in the ISA data acquisition card and serial link with the 8051 microcontroller. In an attempt to compensate for these delays, the time axes for all experimental thrust responses in the following sections have been shifted forward by 0.353 seconds, which was the average offset determined from experimental data.

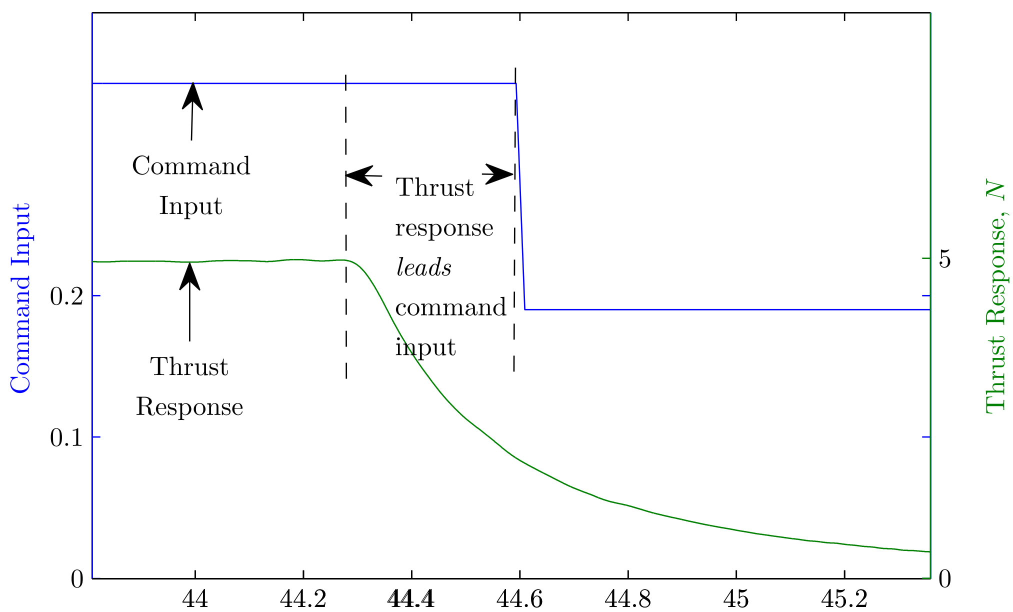

Figure 3–13: Time lag of recorded thrust response with respect to input signal.

While operating the thruster, it is preferable to limit the lowest control input to idle speed since stopping the motor in-flight requires the speed controller to be re-armed. Keeping this in mind, each step input was applied with the motor idling initially. After holding the command constant for a period of 40 seconds, a negative step was applied to bring the speed back down to idle again. Measurement noise and vibrations were removed from all recorded load cell data by applying a third-order zero-phase[52] Butterworth low-pass filter with a cutoff frequency of 9.67 Hz. Two such filtered responses can be seen in Figures 3–14 and 3–15 and the complete set of responses may be viewed in Appendix A. Figure 3–14 shows that approximately 1.8 N of thrust was generated for a step command input of 0.25 (3000 rpm). For command inputs up to 0.30 (4300 rpm), a distinct steady-state value could be determined from the recorded load cell data. However, responses to higher inputs showed that the thrust reached a peak and then dropped steadily despite the command being held constant. As an example, Figure 3–15 shows the thrust response to a command input of 0.50 (7300 rpm). After reaching an initial peak of 11.36 N, the thrust dropped by approximately

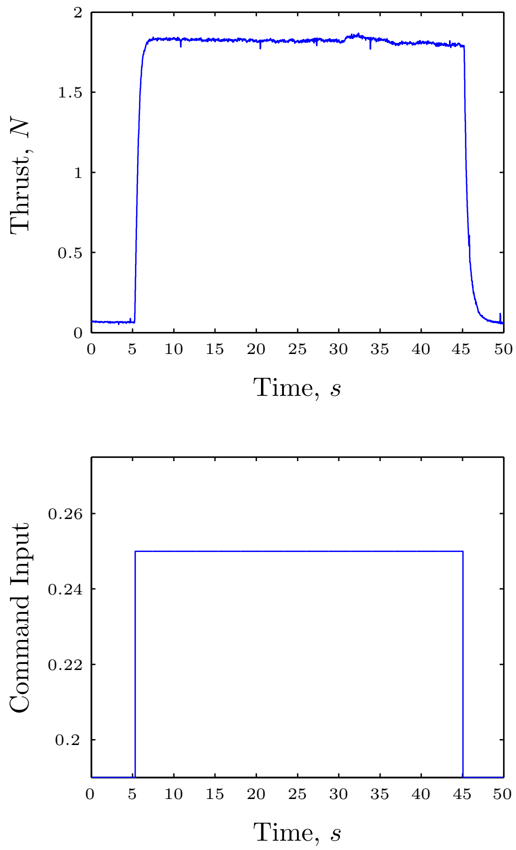

Figure 3–14: Step response(top) to command input(bottom) of 0.25

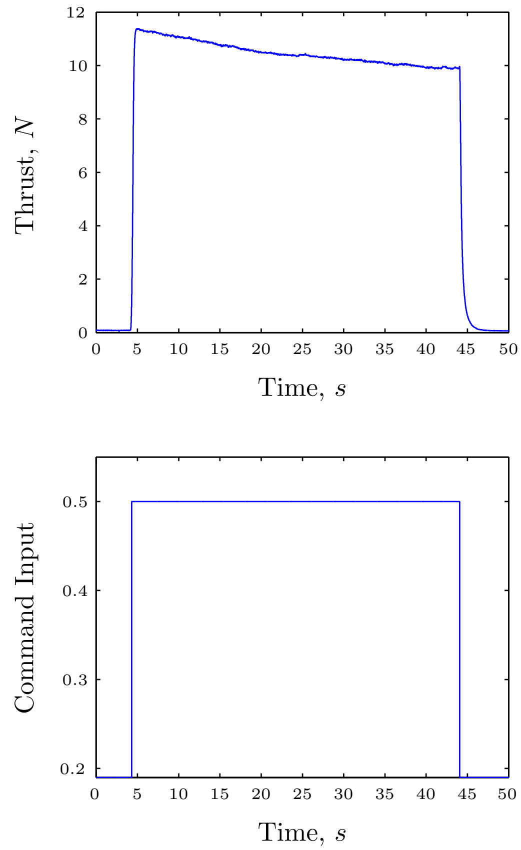

Figure 3–15: Step response(top) to command input(bottom) of 0.50.

12% to 10 N over the 40 second duration of the step. Ammeter readings taken during the experiment showed that the motor current did not stay constant, increasing to approximately 24 A at first and then dropping steadily accompanied by a reduction in motor speed. This behavior is not unusual for Lithium polymer battery packs. Figure 3–16 shows a typical battery discharge curve, in which the battery's terminal voltage is plotted against the utilised capacity. It can be seen that at higher discharge rates (higher current draw), there is a sharper drop in the terminal voltage when the battery is fully charged (leftmost point of each curve in Figure 3–16). This drop in terminal voltage occurs due to the larger voltage drop across the battery's own internal resistance. As the terminal voltage drops, the battery's capacity drops and it is no longer able to maintain a constant power output. Since all step responses

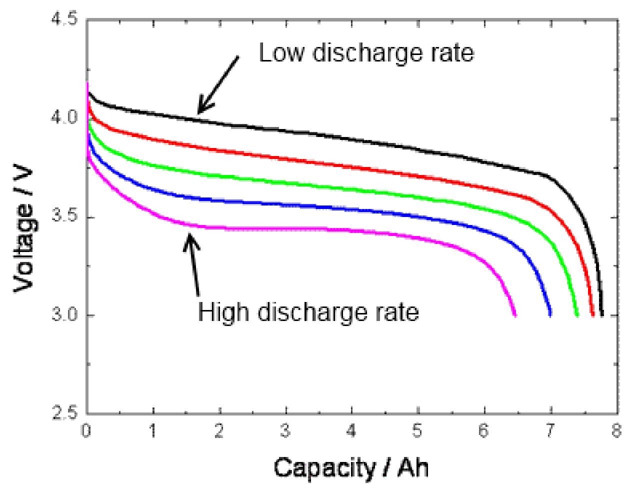

Figure 3–16: Typical battery discharge curve[49].

were measured with a freshly charged battery, a similar drop in the terminal voltage could have occured, thereby reducing the power delivered to the motor and causing a reduction in thrust.

To further investigate the drop in thrust, the system was subjected to two square-wave pulse trains, each with a command input of 0.50: one with short 2 second pulses and another with longer 5 second pulses. Results from these two tests can be seen in Figures 3–17 and 3–18 respectively. In both cases, a 2 second rest was given between pulses. Comparing the two, it is clear that the drop in thrust is lower for the short pulses. Another trend of interest is the reduction in peak thrust of consecutive pulses, an effect which was more pronounced when the pulses were long. Similar tests with a longer rest time between the pulses showed that the reduction in peak thrust was almost negligible, which could be explained by the battery's terminal voltage to recovering to a higher value between pulses. It can be seen that the battery response is not synchronized with the input. This is because the voltages of the batteries on the airship are not measured concurrently but in a fixed sequence with a sampling time of 500 ms. Since the airship has five batteries, four

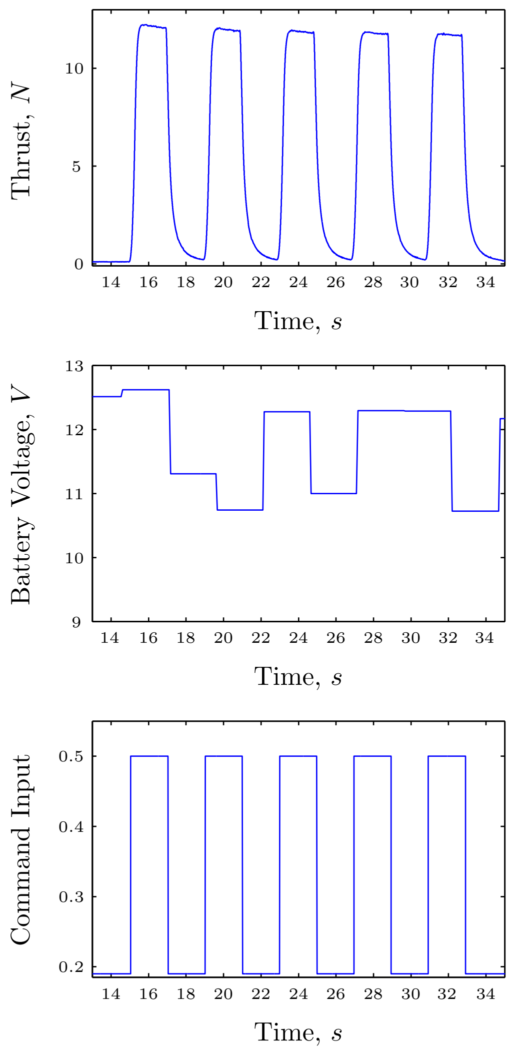

Figure 3–17: Thrust(top) and battery voltage(middle) response to short, high frequency pulse input(bottom).

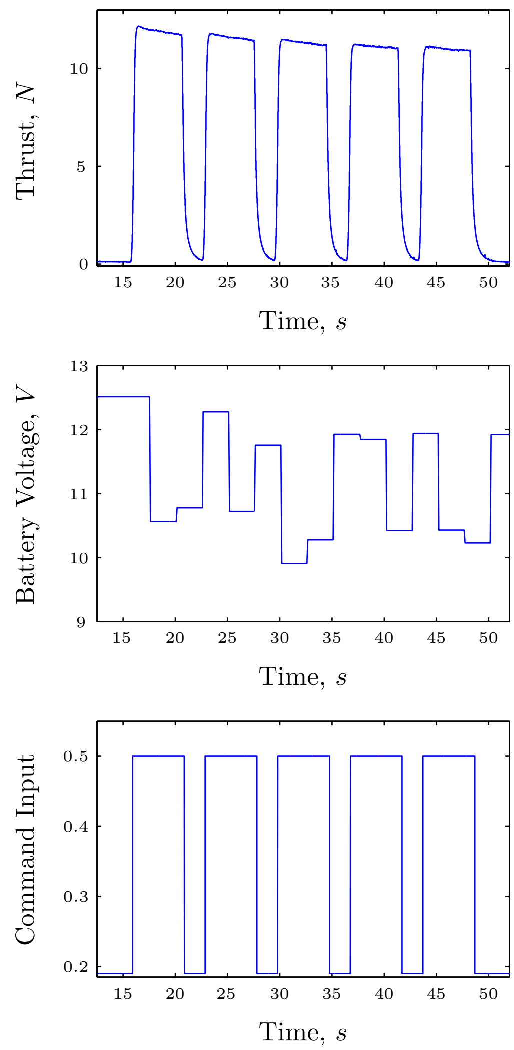

Figure 3–18: Thrust(top) and battery voltage(middle) response to long, high frequency pulse input(bottom).

for its thrusters and one for its avionics, there is a delay of 2.5 s between successive voltage measurements for a particular battery. An additional delay is introduced in the voltage readings by a low-pass filter which is applied to the analog-to-digital converter (ADC) measurements.

The transient portion of all recorded thrust responses exhibited no overshoot in either the ascent or descent of thrust, which is indicative of an over-damped system. In general, it was observed that the time required to slow down to idle speed from a higher commanded speed was greater than that required when speeding up from idle. As well, the rise and fall of thrust appeared to get faster with increasing command inputs.

These initial tests helped determine the amount of thrust available for various inputs to the system. While step command inputs of 0.30 and below yielded a clear steady-state value, this was not the case at higher speeds since the thrust began to decay after reaching a peak value. Results from the square-wave pulse tests confirmed that the amount of thrust generated had a correlation with the battery pack's terminal voltage, which is reduced by sustained current draw due to its internal resistance. The influence of the battery's dynamics on thrust requires further study but is beyond the scope of this thesis. Another outcome of the tests conducted was the identification of an upper limit on permissible control inputs during flight. It was found that command inputs greater than 0.50 (7300 rpm) resulted in a current draw that approached the electronic speed controller's rated limit. The following section discusses the development of a thruster model fitted to experimental step responses and tuning of model parameters using more complex inputs.

3.2.3 Modeling and Validation

The previous section covered step responses collected from the experimental setup and preliminary observations were made on the effect of battery voltage on generated thrust. In general, thruster models have not incorporated the effect of drain on the power source. As an example, [36] proposes a simple single-pole single-zero dynamics model but neglects the reduction in terminal voltage stating that it has minimal effect on the system. Others [37][39] neglect the battery dynamics completely. For the time being, we shall not model the drop in thrust caused by battery drain experienced at higher motor speeds because we only expect to be operating at such high thrust levels for short intervals of time. Broadly speaking, the model development may be broken down into the following steps:

1. **Fitting** - Fit transfer functions to experimental data and implement model in MATLAB/Simulink.
2. **Tuning and Validation** - Test model with more elaborate inputs and tune parameters if necessary. Validate with more tests.

Response Fitting and Model Implementation

In this section, we use simple transfer functions to generate artificial thrust responses that match responses obtained from the experiment. The form of these transfer functions is determined by examining experimental response characteristics such as the rise time, damping, overshoot, and steady state value. As an example, the ascending and descending part of the experimental curve in Figure 3–14 resemble the step response of a first-order low-pass filter. No overshoot is present in either case but they approach their steady-state values at different speeds. At higher thrust levels (such as in Figure 3–15), if one were to neglect the drop in thrust over the step, similar first-order low-pass filter behavior may be seen in the ascent and descent dynamics. For each test case, we now fit a simple first order transfer function of the form:

$$G(s) = \frac{T(s)}{C(s)} = \frac{\alpha(s)}{\tau s + 1} \tag{3.2}$$

where $\frac{T(s)}{C(s)}$ represents the transfer function from command input c to the thrust T. α is a constant gain that determines the steady state thrust level for a command input c. τ is the time constant of the thrust response, or the time taken to reach 63% of the steady state thrust. The experimental and fitted responses for step inputs of 0.25 (3000 rpm) and 0.50 (7300 rpm) are plotted in Figure 3–19 and 3–20 respectively. Appendix A shows the fitted response for all other test cases. The

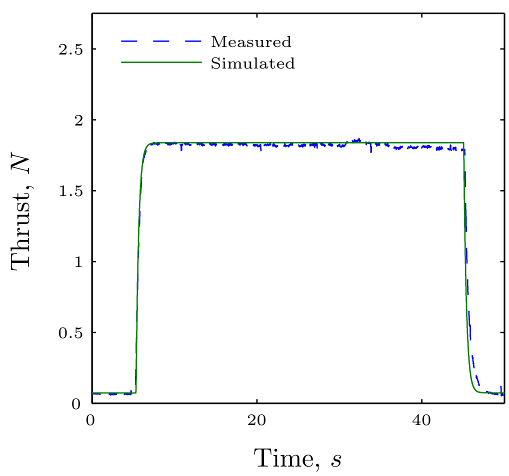

Figure 3–19: Experimental and simulated step responses for command input of 0.25. In the model, α=7.06 and τ=0.16 s.

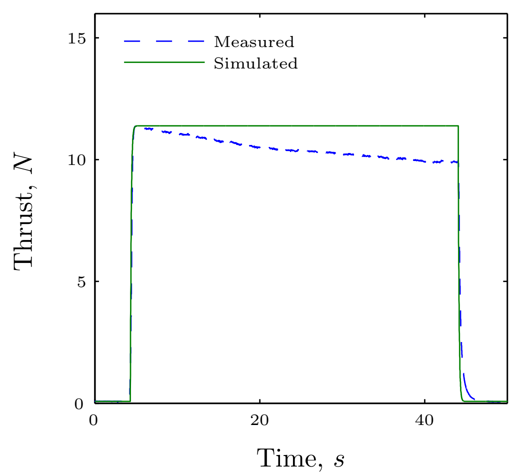

Figure 3–20: Experimental and simulated step responses for command input of 0.50. In the model, α=22.6 and τ=0.05 s.

transfer function in equation (3.2) was used with a gain of 7.06 and time constant of 0.16 seconds to generate the simulated response in Figure 3–19. It can be seen that a single time constant cannot fit both the ascent and descent of the thrust response because the response is slower on the way down. The transfer function was chosen to provide a better fit to the positive step response while the simulated negative step response remains slightly faster than the experiment. To simulate the step response to a command input of 0.50 (Figure 3–20), we use equation (3.2) with a gain of 22.6 and a time constant of 0.05 seconds. The difference between the simulated and experimental thrust response is immediately noticeable. As discussed previously, the drop in thrust will not be modeled for now and it will need to be taken into account during controller design. Once again, the single time constant chosen provides a slightly better fit for the ascent of the thrust response compared to the descent. After fitting similar low-pass transfer functions to all other step responses, the values for the time constant and gain obtained in case are tabulated in Table 3–1. For each command input in column 1, the motor speeds in column 5 are obtained from the experimental data points in Figure 3–11.

Table 3–1: Gain, time constant and discrete filter coefficients for fitted transfer functions.

Command Input, c	Gain, α	Time Constant, τ	Approx. Peak rpm	a_1	b_1
0.19	0.39	0.21	500	0.005	-0.988
0.20	0.48	0.20	1730	0.117	-0.988
0.25	7.06	0.16	3000	0.456	-0.985
0.30	10.9	0.13	4300	0.566	-0.981
0.35	14.6	0.10	5200	0.790	-0.975
0.40	17.8	0.08	5800	1.043	-0.969
0.45	21.6	0.06	6480	1.309	-0.965
0.50	22.6	0.05	7300	1.780	-0.951

A peak thrust can be obtained from each gain α by multiplication with the corresponding command input in column 1. If this product is plotted against the square of the rotation speed in column 4, it can be seen (Figure 3–21) that the relation is almost linear and hence, in agreement with data from marine thrusters under bollard pull conditions[37][38][39].

The trend seen in the time constants of Table 3–1 is somewhat counter-intuitive since the response appears to get slower with decreasing inputs. Interestingly, this is almost

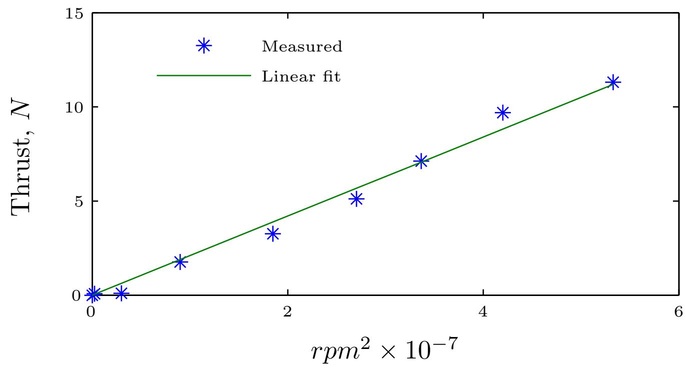

Figure 3–21: Thrust versus square of propeller rotation speed.

identical to the results from [40], in which simulation results exhibited a similar degradation in the time response with lower magnitude inputs. This has important design implications for the MkII flight controller since excluding the variation in time constants could induce limit cycling behavior[40] in the closed loop system (sustained oscillations about a desired set point). Furthermore, the quicker thrust response at higher motor speeds suggests that it might be advantageous to run the thrusters in this regime by adding ballast to the airship. However, this would necessarily reduce the endurance of the airship.

Having obtained a set of low-pass filters that simulate step responses to various command inputs, the functioning of the dynamics model can be described as follows: it is essentially a single low-pass filter whose time constant and gain are obtained from Table 3–1 based on the instantaneous command input. For inputs that fall between those in column 1, filter parameters can be determined by a linear interpolation between rows. The following section explains the integration of the thrust dynamics into the overall airship dynamics model.

Implementation in Airship Dynamics Model

The dynamics equations for the MkII ALTAV are currently implemented in a continuous-time Simulink model. In order to implement the thruster model as described in the previous section, we need a low-pass filter block whose parameters can be changed dynamically based on the command input. Since this cannot be achieved with a continuous-time filter block in Simulink, we resort to using a discrete version which accepts numerator and denominator coefficients through separate inputs. A first-order discrete representation of the transfer function in equation(3.2) is shown in equation (3.3)

$$G(z) = \frac{T(z)}{C(z)} = \frac{a_1 z^{-1}}{1 + b_1 z^{-1}} \tag{3.3}$$

where z^{-1} denotes a delay of 1 sample. For each transfer function obtained in the previous section, we first apply MATLAB's *c2d* (continuous to discrete) command to obtain the discrete representation in equation (3.3). A sample time of $\frac{1}{400}$ seconds is chosen for discretization in order to accommodate future implementation of the thruster model on board the airship, whose attitude controller generates desired thruster inputs at 400 Hz. Next, we use the *tfdata* command to extract the coefficients a_1 and b_1. These coefficients are listed in columns 5 and 6 of Table 3–1.

In the airship simulation, the thruster model receives inputs from a controller in the form of desired thrust values. Before a desired thrust can be passed to the thruster dynamics model, it must first be converted to a command input. This is achieved by deriving the inverse of the thruster dynamics model (or the *forward* dynamics). In contrast to the forward (thruster) dynamics model, the *inverse* model's input is a desired thrust and its output is the command input required to generate said thrust. Figure 3–22 shows a plot of the command input versus the steady-state thrust computed by multiplying the gain α in Table 3–1 by the command input c. For a given desired thrust T_{des} on the horizontal axis of the plot, the corresponding command input c on the vertical axis can be determined from Figure 3–22 by performing a linear interpolation between the highlighted experimental data points. A block diagram of the overall thruster dynamics model is shown in Figure 3–23. The input to the

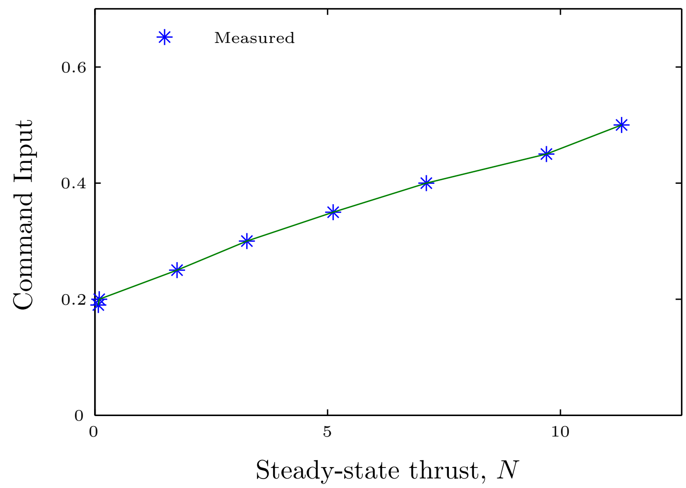

Figure 3–22: Command input versus steady-state thrust.

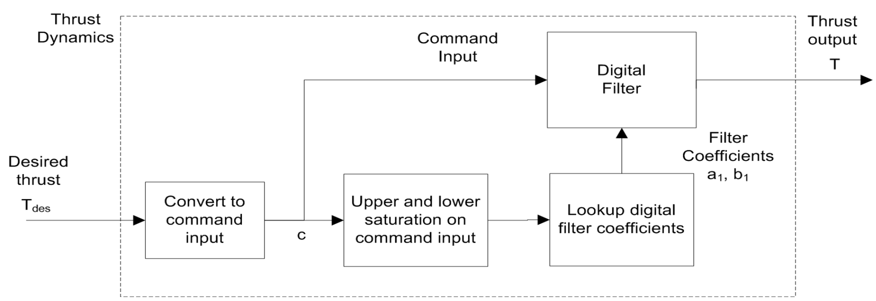

Figure 3–23: Block diagram of thrust dynamics model.

dynamics model is a desired thrust denoted by T_{des} and the output is the simulated thrust T. The desired thrust is first converted to a command input using the method described above. A saturation block has been implemented which limits the lowest command input to 0.19 (500 rpm, idle speed) and the highest to 0.5 (7300 rpm). Next, this command input is passed through a block which looks up the appropriate digital filter coefficients from Table 3–1 using linear interpolation. The numerator and denominator coefficients are then fed into a digital filter block which filters the command input values to generate thrust values.

Model Tuning and Validation

The model developed in the previous section was tested and tuned with more elaborate sequences of force inputs of varying amplitude and frequency. Upon comparing experimental and simulated responses to the two input sequences, it was found that the model was faster than the experiment particularly at lower command thrusts. An example of this can be seen in Figure 3–24, which compares the desired, measured and simulated thrust responses for the first of these input sequences.

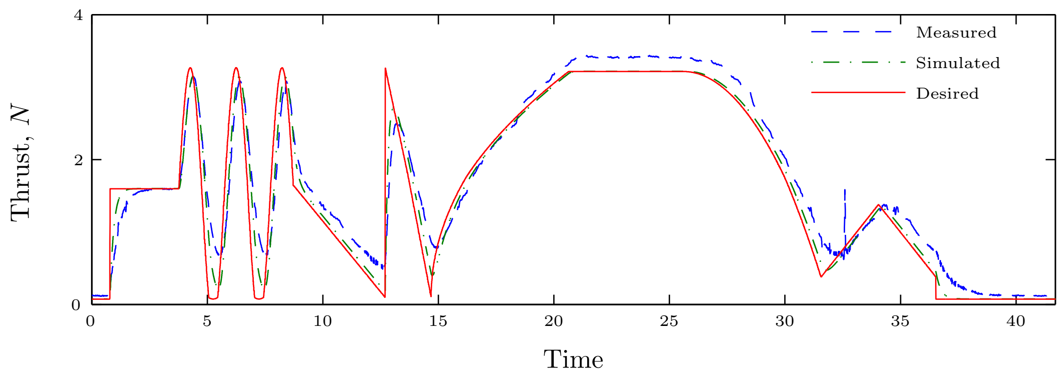

Figure 3–24: Thrust input sequence 1 with untuned coefficients - Comparison between experimental and simulated responses.

The time constants in Table 3–1 were tuned by trial and error until a reasonable fit was obtained in both tests. Results from the tuned model can be seen in Figures 3–26 and 3–27. The tuned continuous filter parameters and discrete filter coefficients for each command input are shown in Table 3–2.

The difference between the two sets of time constants, shown in Figure 3–25, shows the large level of adjustment that was required to produce a good fit between simulation and experiment for arbitrary inputs. One possible explanation for this might be due to the approach used in Section 3.2.3 for selecting a time constant for each experimental step input. In Section 3.2.2, it was noted that the rising part of the step thrust responses was faster than the fall. The low-pass filters developed in Section

Table 3–2: Tuned gain, time constant and discrete filter coefficients for fitted transfer functions.

Command Input, c	Gain, α	Tuned Time Constant, τ	Approx. Peak rpm	a_1	b_1
0.19	0.39	0.5263	500	0.0018	-0.9953
0.20	0.48	0.5033	1730	0.0024	-0.9950
0.25	7.06	0.4000	3000	0.0440	-0.9938
0.30	10.9	0.2145	4300	0.1262	-0.9884
0.35	14.6	0.1500	5200	0.2418	-0.9835
0.40	17.8	0.1200	5800	0.3669	-0.9794
0.45	21.6	0.1050	6480	0.5071	-0.9765
0.50	22.6	0.0750	7300	0.7419	-0.9672

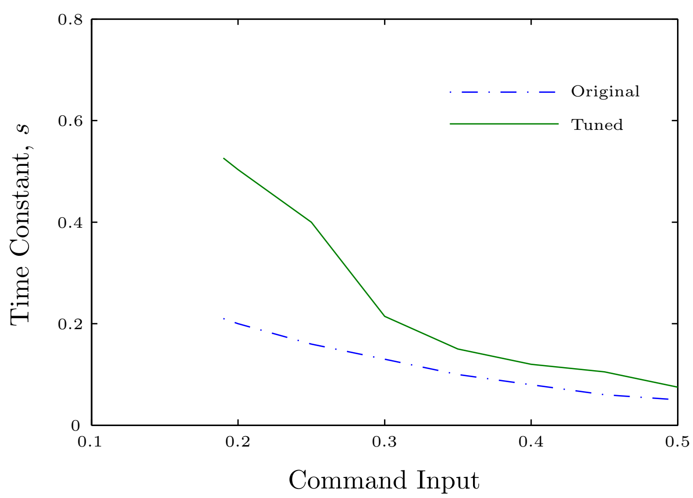

Figure 3–25: Comparison between original and tuned time constants.

3.2.3 matched the rise of the response better than the decay, which resulted in the simulated response always being faster than the experiment for the negative part of the step input. Since the tuned time constants are all higher than the original values, perhaps the thrust response to the negative step input might have been a better representation of the plant's dynamics.

From the plots in Figures 3–26 and 3–27, it can be seen that the model predicts the generated thrust and its transient characteristics quite well. Due to the adjustment made to the time scale of the experimental responses (see Section 3.2.2) it is difficult

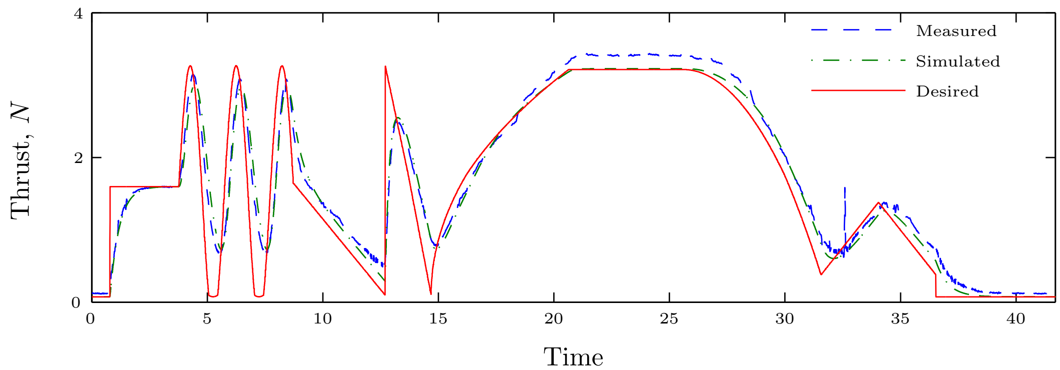

Figure 3–26: Thrust input sequence 1 with tuned coefficients - Comparison between experimental and simulated responses.

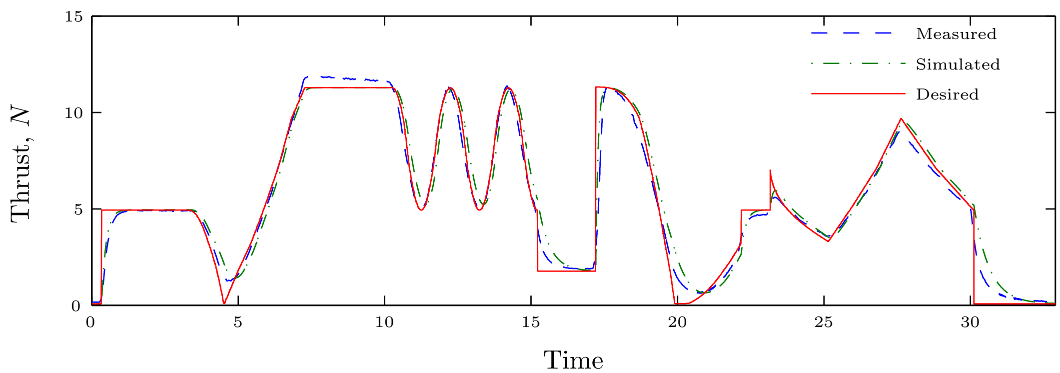

Figure 3–27: Thrust input sequence 2 with tuned coefficients - Comparison between experimental and simulated responses.

to compare phase lag in the experimental data to that in the model. In Figure 3–27, the largest error (5.4%) in the simulated response occurs at the peak thrust between t=7 s and t=10 s. This could be due to slight differences in capacities and discharge characteristics of the battery packs used during experiments. An error of similar magnitude is present in the results of the first validation test (Figure 3–26) between t=20 s and t=27 s. The thruster model's bandwidth increases with the instantaneous thrust command, and this can be seen in Figure 3–26 between t=4 s and t=9 s. Here, the model is able to track the sinusoidal thrust input signal at higher thrust values but is unable to do so at lower thrusts.

A third sequence of arbitrary thrust inputs was applied to the thruster and compared with simulation data to ensure the model hadn't been tuned specifically to the previous test cases. Results from the experiment and simulation are compared in Figure 3–28. Once again, the experimental and simulated responses are in very good agreement with each other.

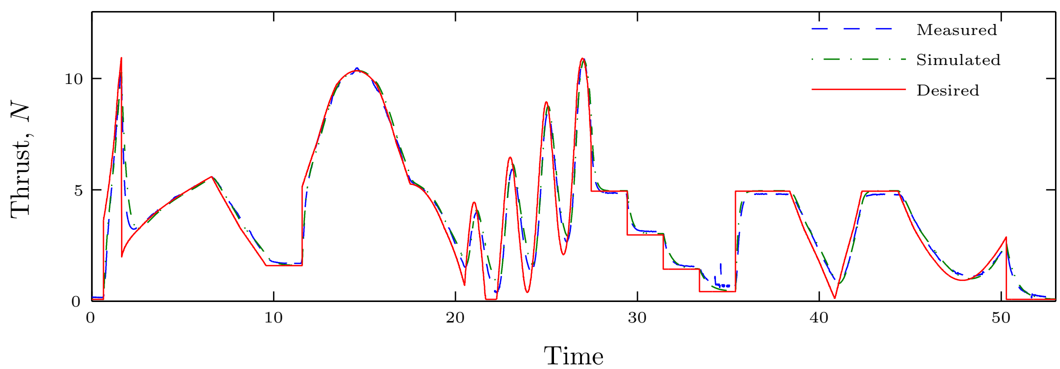

Figure 3–28: Thrust input sequence 3 with tuned coefficients - Comparison between experimental and simulated responses.

3.2.4 Delay Identification

In Section 3.2.2, it was shown that the measured thrust responses were *leading* the input signal by approximately 0.353 seconds. While the exact cause of this was unclear, delays in logging the input signal were most likely responsible for this error. In order to facilitate comparison with the simulated thrust responses, the time axes for all experimental data shown in Section 3.2.2 were adjusted to match the input signals. However, there is still a lack of information on how much time elapses between issuing a thrust command and seeing a change in the thrust response. In order to characterize this delay, a simple experimental setup was devised, different from the one in Section 3.2.1.

The experimental setup in Figure 3–29 was designed to drive the thruster as if it were receiving commands from an attitude controller on the airship. This is typically how

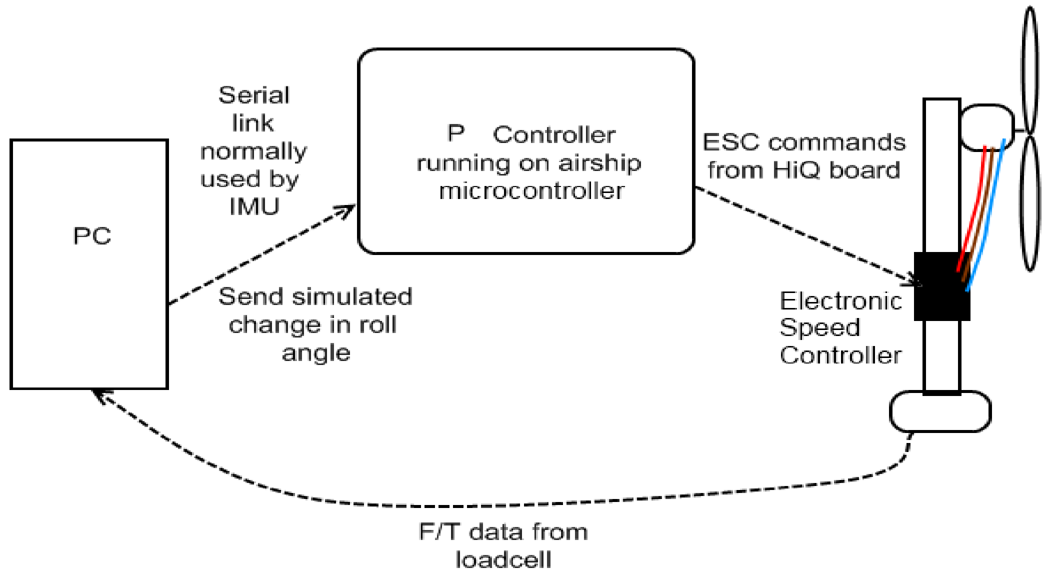

Figure 3–29: Experimental setup used in delay characterization.

the thrusters are operated during flights and such a setup allows us to evaluate the delays under realistic conditions. Figure 3–29 shows a schematic of the experimental setup used.

Normally, the HiQ board receives attitude information from an inertial measurement unit (IMU) connected by a serial link. For our experiment, we replace the IMU by a desktop computer and send an artifical roll angle signal from it. This simulated roll angle ϕ_{sim} is read by the HiQ board at 100 Hz and then passed on to a simple proportional controller ($K_p = 0.2$) running at a rate of 64 Hz. The controller converts the simulated change in attitude to a thrust demand as follows

$$T = T_{offset} + K_p\phi_{sim} = T_{offset} + 0.2\phi_{sim} \tag{3.4}$$

where T_{offset} is a constant thrust offset (in Newtons) used to raise the overall thrust level and operate the thruster in different motor speed regimes. ϕ_{sim} is the simulated roll angles in degrees. The thrust demand T is in turn converted to a HiQ command input using the data in Figure 3–22. A PWM signal is then generated based on the command input c and sent to the thruster's electronic speed controller. The thrust is recorded by the ATI force-torque sensor and logged on the same desktop computer that generates the artificial roll angle signal, and thus all data can be timestamped by a single clock.

Results

Step changes in the roll angle were generated from the desktop computer and sent to the HiQ board. In all cases, the step was applied 5 seconds after the test began. Force-torque transducer data from one such test is shown in Figure 3–30. The graph has been magnified to show the region immediately after the step input command at $t = 5s$. A thrust offset of T_{offset}=5 N was used in the test and the roll angle ϕ_{sim} was changed from 0° to 20°. This corresponds to an initial thrust demand of 5 N and a final (after the step input) thrust demand of 9 N. We can see from Figure

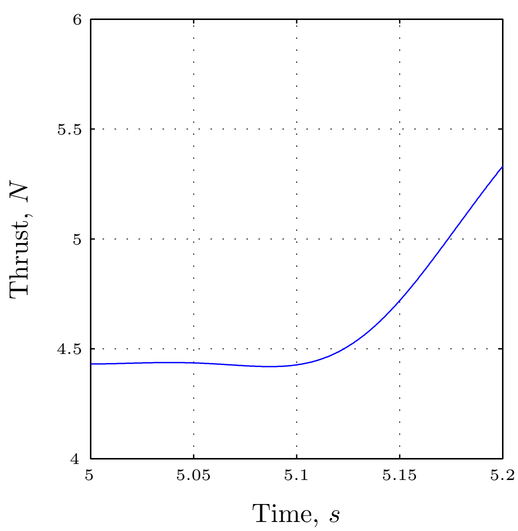

Figure 3–30: Delay in thrust response to positive step input at $t = 5s$.

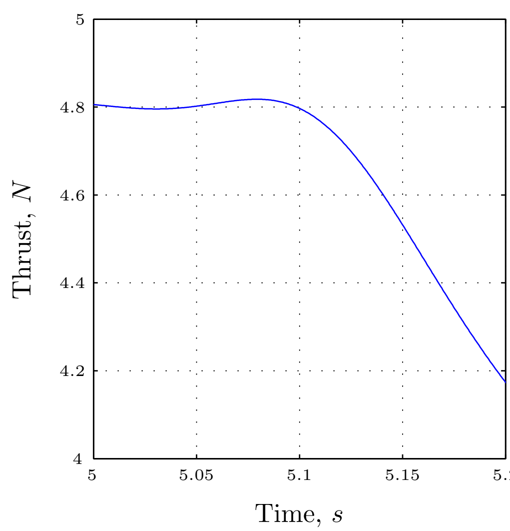

Figure 3–31: Delay in thrust response to negative step input at $t = 5s$.

3–30 that it takes ≈ 90 ms after the step change for the thruster to respond to the command. Another test case with a negative step (reduction in thrust) is shown in Figure 3–31. Here, the thrust offset was 5 N and a negative step from 0° to -10° was sent to the proportional controller. As for Figure 3–30, there is a delay of around 85 ms in the thrust response after application of the step input. In general, the observed delays ranged from 80-90 ms and we choose an average value of 85 ms for the thruster dynamics model. With the added delay in the thrust dynamics we can modify the block diagram in Figure 3–23 to get the model in Figure 3–32.

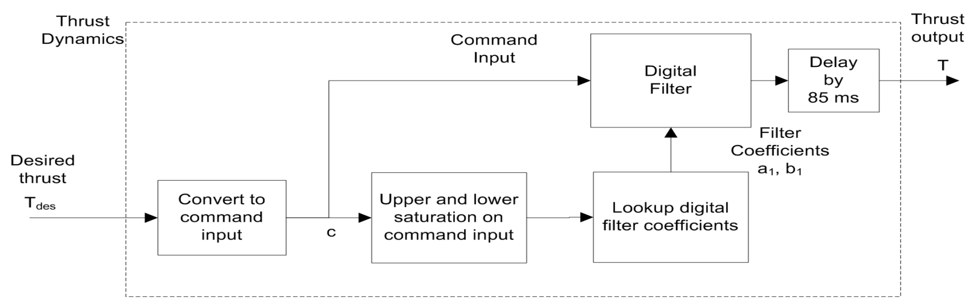

Figure 3–32: Revised block diagram of thrust dynamics model.

Part of this delay could be due to the 64 Hz iteration rate of the flight controller. To demonstrate this experimentally, the speed of the controller was increased to 100 Hz and the thruster's response to a step change in roll angle was measured. The response time was measured to be 60 ms, around 30 ms faster than the delay with a 64 Hz controller. Other possible sources of delay include the speed controller and the force/torque data acquisition system.

3.3 Servo Motor Model

The second part of the thruster's operation is the vectoring capability provided by the Hitec HS-322HD servo motor. For applications which don't require high accuracy positioning, such as the MkII's thrust vectoring system, the HS-322HD offers a quick response time with little to no overshoot and sufficient torque to hold its position. Servos typically make use of closed-loop control to set the position of the output shaft. A schematic illustrating this is shown in Figure 3–33. Since details of the servo's internal components were not available, a model of the servo's dynamics was

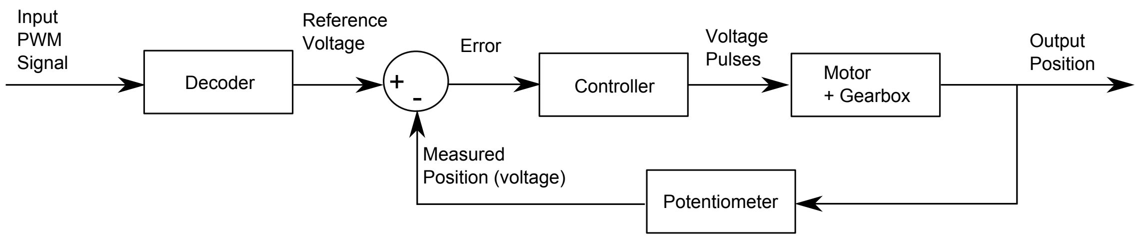

Figure 3–33: Schematic of feedback controller in servo motors.

developed by treating it as a 'black box' and using experimental data to identify its dynamics. Section 3.3.1 discusses the experimental setup used in the servo characterization. In Section 3.3.2, responses of the servo are analysed for sinusoidal inputs of varying amplitude and frequency. A servo model is then developed in Section 3.3.3 and validated against experimental data.

3.3.1 Experimental Setup

The experimental setup used to characterize the servo, shown in Figure 3–34, has three main functions: send commands to the servo motor, read the position of the output shaft, and log time histories of the desired and measured shaft position. A

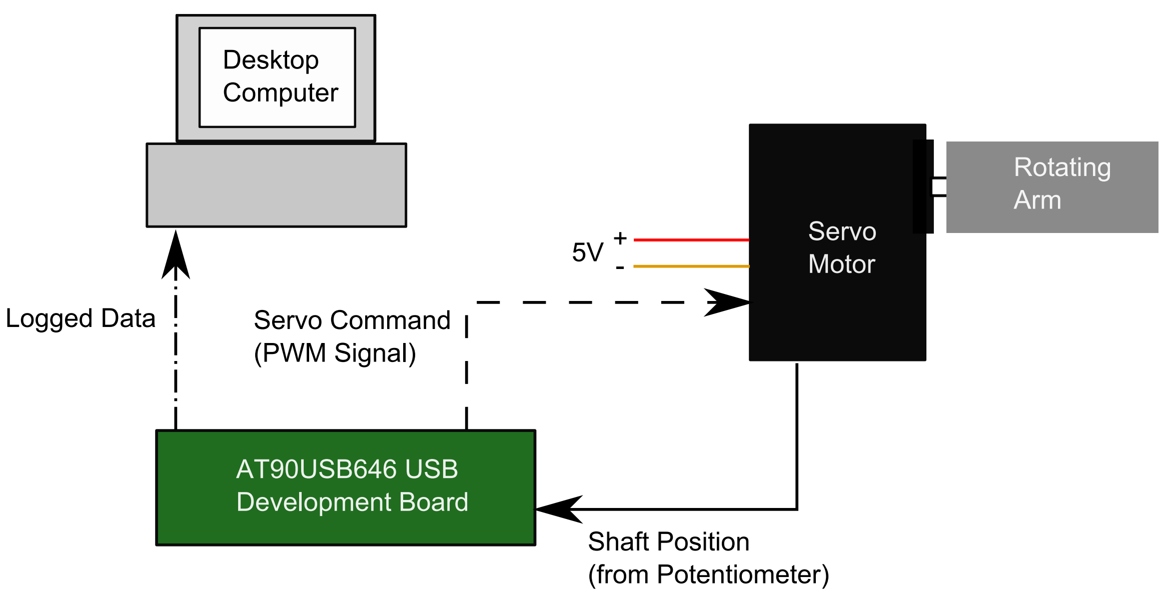

Figure 3–34: Experimental setup for servo characterization.

programmable USB development board[50] based on the 8-bit Atmel AT90USB646 microcontroller was used to send commands to the servo motor. As discussed previously, all servos have a potentiometer to provide feedback on the position of the output shaft. A wire was soldered to the output terminal of this potentiometer in the HS-322HD servo and connected to a 10-bit analog input channel on the USB development board. The servo was powered by a 5 volt DC supply. As shown in Figure 3–34, the rotating thruster arm (with the brushless motor, propeller and speed controller) was attached to the servo during the tests to mimic the load it would experience in normal operation.

The AT90USB646 USB development board can be programmed using the freeware Arduino[51] integrated developement environment. A short script was written to execute the following steps in a loop running at 500 Hz:

Send Command to the Servo

The Arduino Servo software library was used to send PWM commands to the HS-322HD motor. It generates a 50 Hz pulse with a user-specified width between 0.54 ms and 2.40 ms. Given a desired servo angle $-90° \leq \beta_{des} \leq +90°$, the required input pulse width, PW_{req}, in ms, can be computed by rearranging equation (3.1).

$$PW_{req} = 0.6 + \left(\frac{\beta_{des} + 90}{100}\right) \tag{3.5}$$

Read Potentiometer Voltage on Analog Channel

The servo's angular position is read from the potentiometer as a voltage. A relation between the two was determined by measuring the potentiometer's output voltage at an angle of 0° and +90°. At 0°, the voltage was measured to be 1.18 V and at +90°, the voltage was 1.98 V. Under the assumption that the potentiometer's resistance varies linearly with the angular position, we can compute the measured servo angle

β_{meas} for a potentiometer voltage, V_{pot}

$$\beta_{meas} = 90\left(\frac{V_{pot} - 1.18}{1.98 - 1.18}\right) = 112.5(V_{pot} - 1.18) \tag{3.6}$$

Send Data to Desktop Computer

After issuing the servo command and reading the current angular position, the script sends an elapsed time value along with the desired and measured servo angles to a desktop computer via a serial port on the microcontroller. Transmission delays in the serial link did not affect the results since timestamps for the data were generated on the microcontroller rather than the desktop computer.

3.3.2 Test Results

Sinusoidal responses

The response of the servo was recorded for sinusoidal inputs of varying frequency and amplitude about $\beta = 0$ (the vertical position). Measurement noise was removed from all responses presented in this section by applying a fourth-order zero-phase[52] Butterworth low-pass filter with a cutoff frequency of 50 Hz. Figure 3–35 shows the servo response to a 0.3 Hz sinusoidal input of amplitude 10°. From Figure 3–35, we can see that the servo tracks the input signal reasonably well albeit with an error of ±1° in the measured response. This level of accuracy is typical for hobby servos such as the HS-322HD. There is also a slight delay in the response with respect to the input signal. This delay was estimated to be ≈50 ms by adjusting the time axis of the input signal to match the response. We now double the frequency of the input sinusoid to 0.6 Hz and set an amplitude of 30°. The response to this input can be seen in Figure 3–36

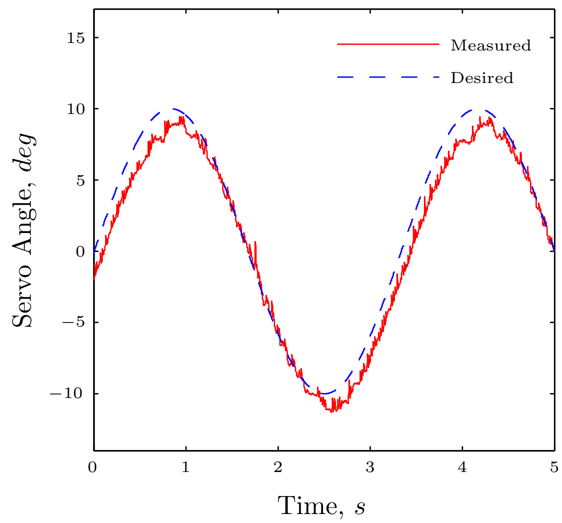

Figure 3–35: Servo response to input sine wave of 10° amplitude, 0.3 Hz frequency..

With a faster input signal of larger amplitude, the servo still managed to track the reference angular position. The error between the two was around 1.5° and as before, the response was delayed by 50 ms. This delay was also observed in other sets of measured data. In the experimental setup used, servo commands were being sent at a rate of 500 Hz, causing a delay of 2 ms, at most attributable to the AT90USB646 microcontroller. We can therefore conclude that atleast 48 ms of the observed delay is due to the internal circuitry of the servo.

As the amplitude and frequency of the input signal were increased, the servo reached its speed limit and was no longer able to track the reference angular position. An example of this is seen in Figure 3–37, which is the servo's response to a 90° sinusoidal input at 1 Hz. The servo's response resembles a triangle wave more than a sinusoid since it reaches its maximum speed in both directions. Measuring the slope of the servo's response, we find that the maximum servo speed is around $287\frac{deg}{s}$. As expected, this value is lower than the manufacturer's rated no-load speed of $316\frac{deg}{s}$.

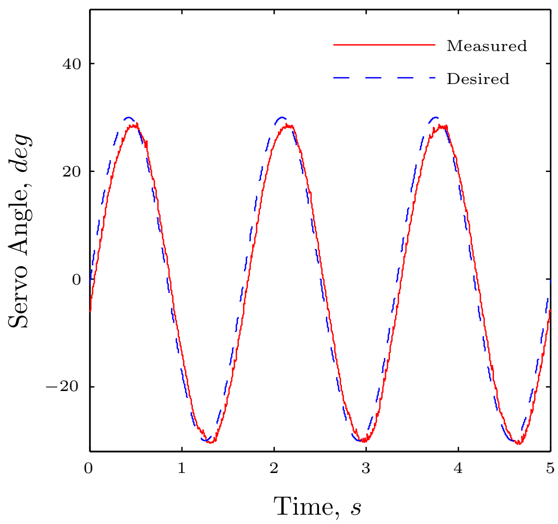

Figure 3–36: Servo response to input sine wave of 30° amplitude, 0.6 Hz frequency..

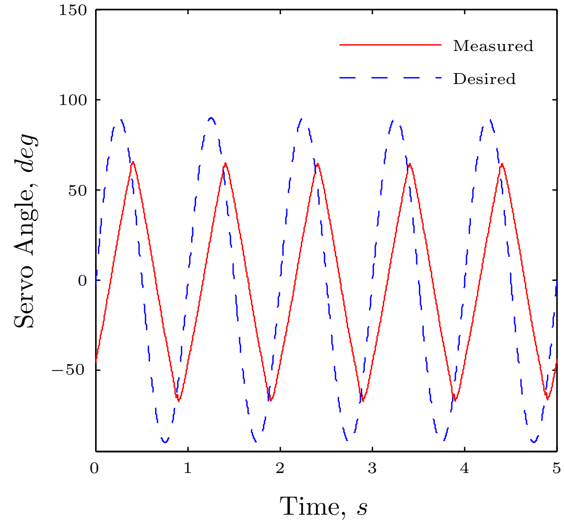

Figure 3–37: Servo response to input sine wave of 90° amplitude, 1 Hz frequency.

3.3.3 Modeling and Validation

Based on the servo characteristics observed in the sinusoidal responses, a model has been implemented in Simulink as shown in the block diagram in Figure 3–38.

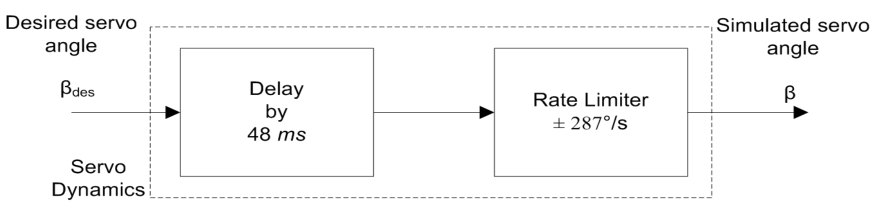

Figure 3–38: Proposed servo dynamics model..

In Figure 3–38, the input to the model (desired servo angle) is denoted by β_{des} and the output from the model, β, is the simulated servo angle. When subject to inputs changing faster than $287\frac{deg}{s}$ clockwise or counter-clockwise, the servo will be limited to operating at its maximum speed. A constant transport delay of 48 ms is applied to mimic the lag seen in the experimental data. The above-mentioned model was compared to experimental servo responses for a slow input signal (Figure 3–39) and

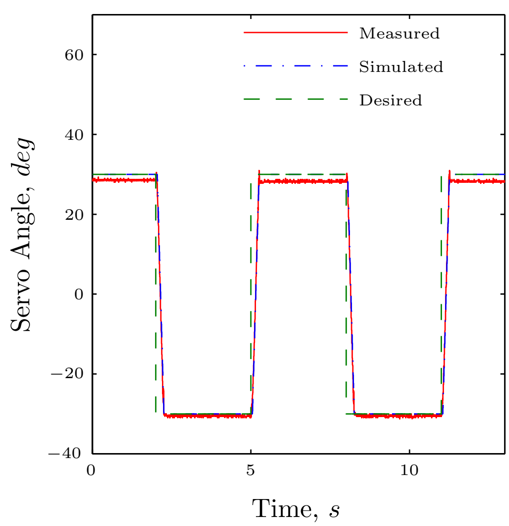

Figure 3–39: Simulated and experimental servo responses to square wave input..

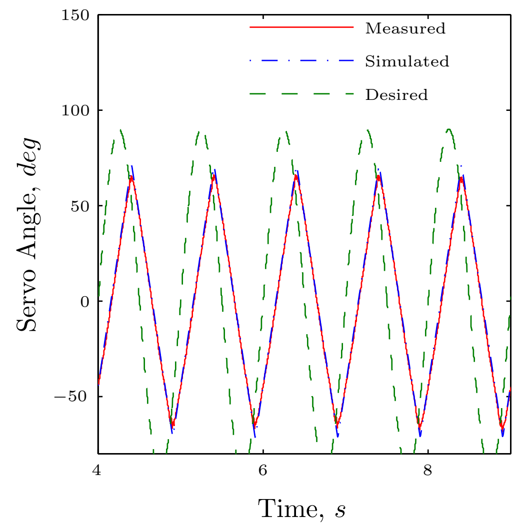

Figure 3–40: Simulated and experimental servo responses to fast sine input in Figure 3–37..

a relatively fast input signal (Figure 3–40). In both cases, it can be seen that the servo model captures the behavior of the HS-322HD servo quite well.

3.4 Computing the Net Thruster Force and Moment

Knowing the outputs of the thruster and servo dynamics models, T and β, we can now compute the net thruster force ($\boldsymbol{f}_T$) and moment($\boldsymbol{n}_T$) in equation(2.1). The numbering of the MkII's thrusters is as follows: the front right thruster is 1, the rear right is 2, the rear left is 3, and the front left is 4. Servo angles are defined with respect to the $-z$ (vertically up) axis of the body frame and the $-y$ direction defines positive rotations. This is shown in Figure 3–41.

As seen in Figure 3–41, the thrust T_i generated by the i'th thruster is assumed to act in the airship's xz plane (no lateral components) at a positive angle β_i to the $-z$ axis. The thrust vector $\boldsymbol{f}_{Ti}$ for the i'th thruster can be written in terms of its thrust

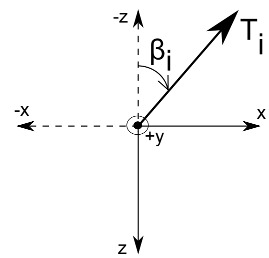

Figure 3–41: Sign convention for servo angles in simulation..

T_i and servo angle β_i as follows

$$\boldsymbol{f}_{Ti} = \begin{bmatrix} T_{xi} \\ 0 \\ T_{zi} \end{bmatrix} = \begin{bmatrix} T_i sin\beta_i \\ 0 \\ -T_i cos\beta_i \end{bmatrix} \tag{3.7}$$

T_{zi} will always be negative since the HS-322HD servos cannot direct the thrust vector downwards. The net thruster force can be written as the sum of the four thrust vectors

$$\boldsymbol{f}_T = \begin{bmatrix} \sum_{i=1}^{4} T_{xi} \\ 0 \\ \sum_{i=1}^{4} T_{zi} \end{bmatrix} \tag{3.8}$$

The net moment acting on the airship can be computed by summing the moments of each thruster about the origin of the body frame. This is depicted in Figure 3–42 for the i'th thruster whose thrust vector $\boldsymbol{f}_{Ti}$ acts at a point located by the position vector $\boldsymbol{r}_{Ti}$ expressed in the body frame. The net moment is calculated by adding up the moment contributions of the four thrusters about the origin of the body frame

$$\boldsymbol{n}_T = \boldsymbol{r}_{T1} \times \boldsymbol{f}_{T1} + \boldsymbol{r}_{T2} \times \boldsymbol{f}_{T2} + \boldsymbol{r}_{T3} \times \boldsymbol{f}_{T3} + \boldsymbol{r}_{T4} \times \boldsymbol{f}_{T4} \tag{3.9}$$

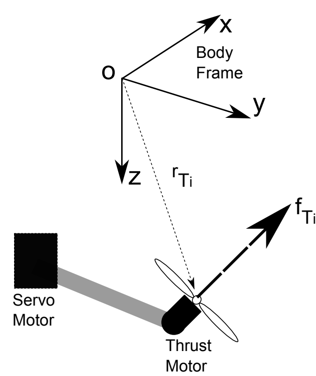

Figure 3–42: Thrust vector and moment arm..

CHAPTER 4
Flight Tests and Model Validation

This chapter deals with the validation of the dynamics model developed in Chapters 2 and 3 by comparing simulated responses of the airship to flight data. Flight tests were performed at the Rutherford Park in Montreal in which the airship's responses to thruster inputs and environmental disturbances were recorded. In Section 4.1, the experimental setup used in the flights is discussed. Next, the closed-loop controller implemented on the airship is detailed in Section 4.2. Section 4.2.1 describes the processing of sensor data to provide the airship's controller with the necessary state variables. In Section 4.3, we first discuss estimation of the wind conditions during the test flights. Next, in Sections 4.3.2 and 4.3.3, the open-loop response of the airship with and without thrusters is compared to the simulation along with a discussion on the performance of the model. Finally, in Section 4.3.4, a simple closed-loop maneuver is simulated to demonstrate the airship's flying qualities under closed-loop control.

4.1 Experimental Setup

The experimental setup used in the flight tests may broadly be broken down into two parts: the ground station and the airship with its instrumentation. A schematic of both these parts is shown in Figure 4–1.

Airship

Since the physical characteristics of the airship hull were discussed extensively in Chapter 2, this section will focus more on the instrumentation on board the airship. At the heart of the MkII's avionics system is the HiQ control board. It is equipped

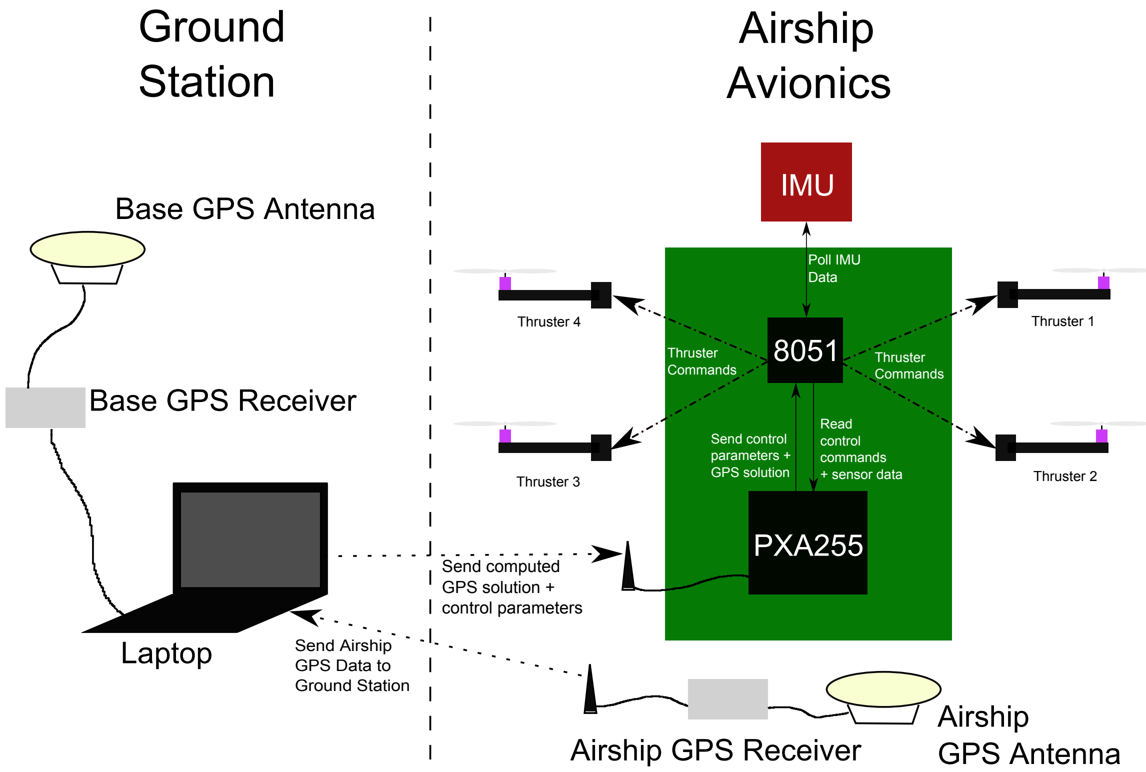

Figure 4–1: Schematic of ground station and airship avionics system.

with two processors, the first of which is an 8051 microcontroller to handle the low-level UAV functions such as processing sensor data and attitude control. The second processor is an Intel PXA255 that manages the high-level functions such as data logging, mission planning and Wi-Fi communication with the ground station.

The airship is equipped with a Microstrain 3DM-GX1 Inertial Measurement Unit (IMU) to provide attitude, angular rate and acceleration data. A serial port on the 8051 microcontroller is used to interface with the IMU, from which data is polled at 64 Hz. The 8051 also runs the airship's low-level (attitude, forward speed, height) controller. Using GPS and IMU data as inputs, this controller generates thrust and servo commands which are sent to the MkII's thrusters through digital I/O pins on the 8051 microcontroller.

A Novatel DGPS(differential GPS) setup is used to track the inertial position and velocity of the airship. A DGPS system has one GPS antenna and receiver at the ground station, and a second pair on the vehicle being tracked. The MkII has an Antcom 1G1215A-XS-4 dual-frequency antenna mounted at the top of its hull which is connected to a Novatel OEM4G2L receiver in the gondola. Binary outputs from the receiver are sent over a Wi-Fi connection to the ground station for further processing. The GPS solution containing the airship's position and velocity is sent back from the ground station to the HiQ board's PXA255 processor over the Wi-Fi network. This GPS data is logged by the PXA255 along with other sensor data and control parameters. The GPS information is also relayed to the 8051 microcontroller for use in the low-level controller.

Ground Station

The ground station consists of a laptop attached to a GPS receiver. It has three main functions in the experiments:

1. To display information to the operator on the airship's state.
2. To compute the airship's position using data from the ground station GPS receiver and the airship's GPS receiver.
3. To transmit user-specified controller setpoints, gains and other parameters to the airship.

A software called Waypoint RTK-Nav is used to process the streams of GPS data from the ground station GPS receiver and the airship's receiver. It is capable of computing the airship's position with centimeter-level accuracy, in real time. The airship's position and velocity are computed at 5 Hz and transmitted over a Wi-Fi connection to the HiQ board on the airship.

4.2 Closed-Loop Controller

As discussed previously, the airship quickly becomes unstable in open-loop flight due to the absence of fins. In addition to being problematic for model validation, this unstable behavior also has an effect on the recording of the airship's position by GPS. During field tests, the airship's GPS antenna would fail to detect satellites when inclined at large roll or pitch angles. It was therefore necessary to implement a controller that would stabilize the airship before commencing the open-loop maneuver.

Five separate PID (Proportional-Integral-Derivative) controllers are used to control the forward speed u, the airship's altitude h, and the three Euler angles ϕ, θ and ψ. The output from the height, roll, and pitch controllers is a force command in the z direction of the body frame. The yaw and forward speed controllers output a force command in x direction of the body frame. In the control laws given below, the convention for the force command is as follows: a force command of $F_{ia,b}$ refers to the force required from thruster number i along the a axis of the body frame to control the state variable b. The numbering of the thrusters is 1 for the forward right thruster, 2 for the rear right thruster, 3 for the rear left thruster and 4 for the forward left thruster. The control gain $k_{P/I/D,b}$ refers to the proportional(P)/integral(I)/derivative(D) gain for state variable b. The subscript d indicates the desired value of a particular state variable.

The control law for forward speed is

$$\begin{bmatrix} F_{1x,u} \\ F_{2x,u} \\ F_{3x,u} \\ F_{4x,u} \end{bmatrix} = \begin{bmatrix} k_{P,u} \\ k_{P,u} \\ k_{P,u} \\ k_{P,u} \end{bmatrix} (u_d - u) + \begin{bmatrix} k_{I,u} \\ k_{I,u} \\ k_{I,u} \\ k_{I,u} \end{bmatrix} \int (u_d - u)dt + \begin{bmatrix} k_{D,u} \\ k_{D,u} \\ k_{D,u} \\ k_{D,u} \end{bmatrix} (\dot{u}_d - \dot{u}) \quad (4.1)$$

The yaw is controlled by commanding differential thrust in the x direction between the left and the right pairs of thrusters.

$$\begin{bmatrix} F_{1x,\psi} \\ F_{2x,\psi} \\ F_{3x,\psi} \\ F_{4x,\psi} \end{bmatrix} = \begin{bmatrix} -k_{P,\psi} \\ -k_{P,\psi} \\ k_{P,\psi} \\ k_{P,\psi} \end{bmatrix} (\psi_d - \psi) + \begin{bmatrix} -k_{I,\psi} \\ -k_{I,\psi} \\ k_{I,\psi} \\ k_{I,\psi} \end{bmatrix} \int (\psi_d - \psi)dt + \begin{bmatrix} -k_{D,\psi} \\ -k_{D,\psi} \\ k_{D,\psi} \\ k_{D,\psi} \end{bmatrix} (\dot{\psi}_d - \dot{\psi}) \tag{4.2}$$

The roll angle ϕ is controlled by commanding differential thrust in the z direction between the left and the right thrusters

$$\begin{bmatrix} F_{1z,\phi} \\ F_{2z,\phi} \\ F_{3z,\phi} \\ F_{4z,\phi} \end{bmatrix} = \begin{bmatrix} k_{P,\phi} \\ k_{P,\phi} \\ -k_{P,\phi} \\ -k_{P,\phi} \end{bmatrix} (\phi_d - \phi) + \begin{bmatrix} k_{I,\phi} \\ k_{I,\phi} \\ -k_{I,\phi} \\ -k_{I,\phi} \end{bmatrix} \int (\phi_d - \phi)dt + \begin{bmatrix} k_{D,\phi} \\ k_{D,\phi} \\ -k_{D,\phi} \\ -k_{D,\phi} \end{bmatrix} (\dot{\phi}_d - \dot{\phi}) \tag{4.3}$$

The controller for the pitch angle θ creates a moment around the body y-axis by commanding differential thrust in the z direction between the forward and the rear thrusters

$$\begin{bmatrix} F_{1z,\theta} \\ F_{2z,\theta} \\ F_{3z,\theta} \\ F_{4z,\theta} \end{bmatrix} = \begin{bmatrix} -k_{P,\theta} \\ k_{P,\theta} \\ k_{P,\theta} \\ -k_{P,\theta} \end{bmatrix} (\theta_d - \theta) + \begin{bmatrix} -k_{I,\theta} \\ k_{I,\theta} \\ k_{I,\theta} \\ -k_{I,\theta} \end{bmatrix} \int (\theta_d - \theta)dt + \begin{bmatrix} -k_{D,\theta} \\ k_{D,\theta} \\ k_{D,\theta} \\ -k_{D,\theta} \end{bmatrix} (\dot{\theta}_d - \dot{\theta}) \tag{4.4}$$

Finally, the height controller commanding a force in the z-direction is

$$\begin{bmatrix} F_{1z,h} \\ F_{2z,h} \\ F_{3z,h} \\ F_{4z,h} \end{bmatrix} = \begin{bmatrix} k_{P,h} \\ k_{P,h} \\ k_{P,h} \\ k_{P,h} \end{bmatrix} (h_d - h) + \begin{bmatrix} k_{I,h} \\ k_{I,h} \\ k_{I,h} \\ k_{I,h} \end{bmatrix} \int (h_d - h)dt + \begin{bmatrix} k_{D,h} \\ k_{D,h} \\ k_{D,h} \\ k_{D,h} \end{bmatrix} (\dot{h}_d - \dot{h}) \quad (4.5)$$

The net thrust for the i'th thruster is computed by

$$T_i = \sqrt{(F_{ix,u} + F_{ix,\psi})^2 + (F_{offset} + F_{iz,h} + F_{iz,\phi} + F_{iz,\theta})^2} \quad (4.6)$$

where the force term F_{offset} is a constant thrust offset added to the z force command of each thruster in order to counter-act the weight of the airship or if desired, to run the brushless motors in different speed regimes. The computed thrust T_i is limited to a maximum of 11.3 N, which is the maximum available thrust as determined in Section 3.2.2. This thrust value is then converted to a HiQ command input using Figure 3–22. The required servo angle β_i is calculated from the net thrust commands in the x and z directions.

$$\beta_i = \tan^{-1} \frac{F_{ix,u} + F_{ix,\psi}}{-(F_{offset} + F_{iz,h} + F_{iz,\phi} + F_{iz,\theta})}. \quad (4.7)$$

A servo angle of 0° indicates a thrust command vertically up (negative z direction). The current thruster configuration does not allow for downward thrust, as the tilt servos provide a range of motion of ±90°. If the sum of the thrust commands in the z direction for a particular thruster results in a downward(positive) or zero thrust command, the command is instead set to a small non-zero upward thrust command of -0.1 N. Equation (4.7) also shows that the amount of servo deflection can be adjusted by varying the constant thrust offset F_{offset} i.e. a larger F_{offset} results in a smaller servo deflection β_i and vice versa. The computed servo angle is then converted to a normalized HiQ servo input as shown below

$$\mu_i = 0.5 + \frac{\beta_i}{180} \tag{4.8}$$

4.2.1 Computing Airship Motion from Sensor Measurements

The control law for forward speed in equation (4.1) of the previous section makes use of the airship's surge speed u, which cannot be obtained from a GPS solution alone. As described in Section 4.1, the airship receives its inertial position and velocity from the ground station over a Wi-Fi network. This inertial position and velocity are relative to the antenna at the ground station, measured in an East-North-Up (ENU) inertial reference frame. In order to determine the surge(u), sway(v) and heave(w) speeds of the airship, we need to transform the measured inertial velocity components of the airship to the body frame. We also have to adjust the heading(yaw) output of the IMU to be expressed relative to true North, consistent with the GPS measurements. We begin by defining the key reference frames that will be used in this section.

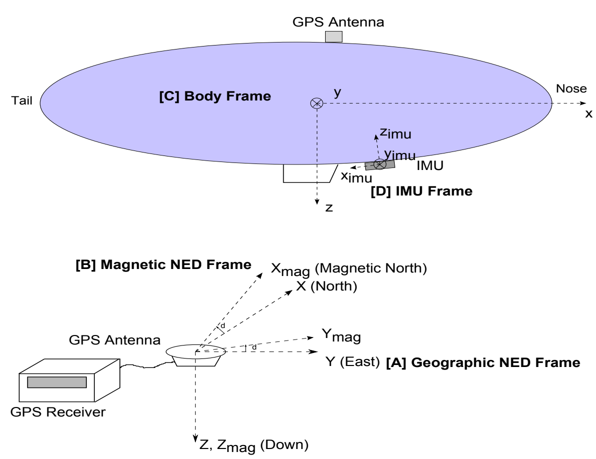

Figure 4–2: Illustration of reference frames used

[A] Geographic North-East-Down (NED) frame: As mentioned in Section 2.1, this is an earth-fixed frame centered at the base GPS antenna whose X axis points to geographic north, Y axis points east and Z axis points downwards to the center of the earth.

[B] Magnetic North-East-Down (NED) frame: Similar to the geographic NED frame, this reference frame is also centered at the base GPS antenna except that its X axis point to magnetic north. As shown in Figure 4–2, magnetic north is inclined at an angle d to the geographic north. This angle is also known as the magnetic variation (or declination) and usually varies with location and time of the year. An estimate of the magnetic variation can be obtained through Natural Resources Canada[53], which provides a declination angle for various Canadian cities based on a user-selectable date. Over the two month test period in Montreal from July to August 2009, the variation ranged from 15.05°W to 15.033°W. However, for the sake of simplicity, we use the average magnetic variation of $d = 15.042°$ W. An enlarged view of the magnetic and geographic NED frames is shown in Figure 4–3. It can be seen that a rotation of $d = -15.042°$ about the inertial Z(down) axis aligns the geographic NED frame with the magnetic NED frame.

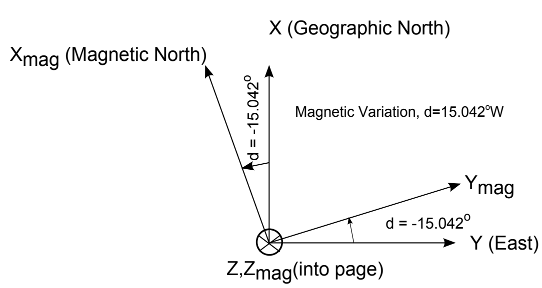

Figure 4–3: Magnetic and Geographic NED frames

[C] Body frame: A reference frame located at the airship's center of volume with the X axis pointing towards the nose, Y axis pointing to the right of the airship, and Z axis pointing down towards the airship's gondola.

[D] IMU frame: This is a reference frame centered at the Microstrain 3DM-GX1 IMU. The Euler angle outputs from the IMU describe the orientation of the IMU frame with respect to the magnetic NED frame. Since the IMU is attached directly to the curved surface of the hull, its axes are not parallel to those of the body frame. The roll and pitch offsets of the mounted IMU with respect to the body axes were determined by holding the airship level and recording the mounted IMU's Euler angle outputs. The pitch offset was approximately 186° while the roll offset was negligible and won't be considered in the current analysis. The yaw offset is assumed to be zero, as well. We can thus depict the IMU axes in relation to the body axes as shown in Figure 4–4. A rotation of $\theta_{mount} = -186°$ about the Y_{IMU} axis is required to align the IMU axes with the body frame.

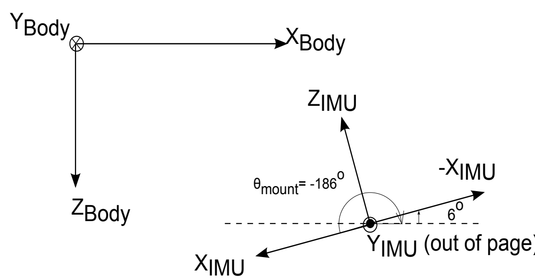

Figure 4–4: IMU and body frames

Transformation Matrix from Geographic NED to Body Frame

Having defined the necessary reference frames, we can now develop a generalized expression for the transformation matrix from the geographic NED to the body frame, $\mathbf{R}_{Geo \to Body}$. From Figure 4–3, we see that a $d°$ rotation about the Z axis can be used to align the geographic NED axes with the magnetic NED axes. Using an elementary rotation matrix about the Z axis to define this transformation we get:

$$\boldsymbol{R}_{Geo\rightarrow Mag} = \begin{bmatrix} c_d & -s_d & 0 \\ s_d & c_d & 0 \\ 0 & 0 & 1 \end{bmatrix} \tag{4.9}$$

where the terms s_x and c_x represent $\sin(x)$ and $\cos(x)$ respectively. Similarly, using Figure 4–4, the transformation from the IMU frame to the body frame is described by a rotation matrix about the Y axis of θ°_{mount}:

$$\boldsymbol{R}_{IMU\rightarrow Body} = \begin{bmatrix} c_{\theta_{mount}} & 0 & s_{\theta_{mount}} \\ 0 & 1 & 0 \\ -s_{\theta_{mount}} & 0 & c_{\theta_{mount}} \end{bmatrix} \tag{4.10}$$

The orientation of the IMU with respect to the magnetic NED axes is given by the following direction cosine matrix which can be derived using the commonly used 3-2-1 (Yaw-Pitch-Roll) rotation sequence:

$$\boldsymbol{R}_{Mag\rightarrow IMU} = \begin{bmatrix} c_{\theta'}c_{\psi'} & c_{\theta'}s_{\psi'} & -s_{\theta'} \\ s_{\theta'}s_{\phi'}c_{\psi'} - c_{\phi'}s_{\psi'} & s_{\theta'}s_{\phi'}s_{\psi'} + c_{\phi'}c_{\psi'} & s_{\phi'}c_{\theta'} \\ c_{\phi'}s_{\theta'}c_{\psi'} + s_{\phi'}s_{\psi'} & c_{\phi'}s_{\theta'}s_{\psi'} - s_{\phi'}c_{\psi'} & c_{\theta'}c_{\phi'} \end{bmatrix} \tag{4.11}$$

where ψ',θ' and ϕ' are the yaw, pitch and roll outputs of the IMU. Finally, we find the transformation matrix $\boldsymbol{R}_{Geo\rightarrow Body}$ from the geographic NED axes to the body frame by multiplying the matrices from equations (4.9), (4.10), and (4.11) in the sequence shown below.

$$\boldsymbol{R}_{Geo\rightarrow Body} = \boldsymbol{R}_{IMU\rightarrow Body} \times \boldsymbol{R}_{Mag\rightarrow IMU} \times \boldsymbol{R}_{Geo\rightarrow Mag} \tag{4.12}$$

$\boldsymbol{R}_{Geo\rightarrow Body}$ can be evaluated by substituting values for the pitch mount offset ($\theta_{mount} = -186^{\circ}$), magnetic variation ($d = -15.042^{\circ}$), and the Euler angles output from the

IMU, ψ', θ' and ϕ'. The airship's true attitude can then be computed from the matrix $\boldsymbol{R}_{Geo\to Body}$ as follows

$$
\begin{aligned}
\psi &= atan2\left(\boldsymbol{R}_{Geo\to Body}(1,2), \boldsymbol{R}_{Geo\to Body}(1,1)\right) \\
\theta &= -asin(\boldsymbol{R}_{Geo\to Body}(1,3)) \\
\phi &= atan2\left(\boldsymbol{R}_{Geo\to Body}(2,3), \boldsymbol{R}_{Geo\to Body}(3,3)\right)
\end{aligned} \tag{4.13}
$$

where $\boldsymbol{R}(i,j)$ represents the matrix element in the i'th row and j'th column and the convention used for the four-quadrant inverse tangent is $atan2(y,x)$. The Euler angles given in equation (4.13) can be used in the control laws in equations (4.2)-(4.4).

Velocity of Center of Buoyancy in Body Frame

The measured position and velocity of the airship's GPS antenna are expressed in East-North-Up coordinates. Since the positive Z axis of the geographic NED frame points downwards, we multiply all GPS measurements along the $Up(Z)$ axis by -1. The velocity components of the airship's GPS antenna expressed in the body frame can then be computed using the measured GPS velocity as follows:

$$
\begin{bmatrix} u_{Ant} \\ v_{Ant} \\ w_{Ant} \end{bmatrix} = \boldsymbol{R}_{Geo\to Body} \begin{bmatrix} (v_X)_{Geo} \\ (v_Y)_{Geo} \\ -(v_Z)_{Geo} \end{bmatrix} \tag{4.14}
$$

where $(v_X)_{Geo}$, $(v_Y)_{Geo}$, and $(v_Z)_{Geo}$ are the measured components of the GPS antenna's velocity in the North, East and Up directions respectively. To find the velocity components at the center of buoyancy, we subtract the translational velocities generated at the GPS antenna due to rotation of the airship.

$$\begin{bmatrix} u \\ v \\ w \end{bmatrix} = \begin{bmatrix} u_{Ant} \\ v_{Ant} \\ w_{Ant} \end{bmatrix} - \begin{bmatrix} p \\ q \\ r \end{bmatrix} \times \begin{bmatrix} x_{Ant} \\ y_{Ant} \\ z_{Ant} \end{bmatrix} \tag{4.15}$$

where $\boldsymbol{v} = [u\ v\ w]$ and $\boldsymbol{\omega} = [p\ q\ r]$ are the velocity of the center of buoyancy and the angular velocity expressed in the body frame. $\boldsymbol{r}_{Ant} = [x_{Ant}\ y_{Ant}\ z_{Ant}]$ is the position vector of the GPS antenna with respect to the center of buoyancy expressed in the body frame. The angular velocity vector in the body frame can be expressed in the terms of the IMU's angular rates as:

$$\boldsymbol{\omega} = \boldsymbol{R}_{IMU\rightarrow Body} \cdot (\boldsymbol{\omega})_{IMU} \tag{4.16}$$

where $(\boldsymbol{\omega})_{IMU}$ is the vector of angular rates measured by the IMU about its own axes and $\boldsymbol{R}_{IMU\rightarrow Body}$ is from equation (4.10). Substituting (4.14) and (4.16) into equation (4.15):

$$\boldsymbol{v} = \boldsymbol{v}_{Ant} - [\boldsymbol{R}_{IMU\rightarrow Body} \cdot (\boldsymbol{\omega})_{IMU}] \times \boldsymbol{r}_{Ant} \tag{4.17}$$

The surge speed of the airship u is the first element in $\boldsymbol{v}$ and can be used in equation (4.1).

Finally, we convert the inertial position of the airship's GPS antenna to the inertial position of the center of buoyancy.

$$(\boldsymbol{r}_{COB})_{Geo} = (\boldsymbol{r}_{Ant})_{Geo} - \boldsymbol{R}^T_{Geo\rightarrow Body} \cdot \boldsymbol{r}_{Ant} \tag{4.18}$$

where $(\boldsymbol{r}_{COB})_{Geo}$ is the position vector of the airship's center of buoyancy with respect to the ground station antenna, expressed in the geographic NED frame. $(\boldsymbol{r}_{Ant})_{Geo} = [X_{Ant}\ Y_{Ant}\ -Z_{Ant}]$ is the measured position of the airship's antenna relative to the base station antenna. The altitude of the airship used in equation (4.5) is the third element of $(\boldsymbol{r}_{COB})_{Geo}$.

4.3 Experimental Results and Comparison

In this section, we compare simulation outputs to measured flight responses in an attempt to validate the dynamics model. Test flights were carried out at the Rutherford Park in Montreal which lies on the southwest facing slope of Mont Royal. An overhead satellite image of the test site can be seen in Figure 4–5.

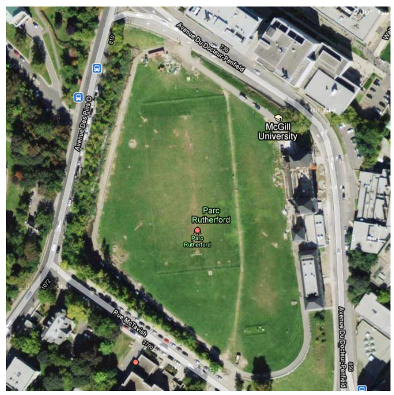

Figure 4–5: Satellite image of Rutherford Park[54].

The experimental setup described in Section 4.1 was used to record the motion of the airship when subject to thruster inputs and wind disturbances. Unfortunately, a few problems were experienced with the setup, which led to a reduction in quality of the data obtained. As mentioned previously, the GPS antenna would tend to lose track of satellites when inclined at large roll or pitch angles. Since the airship became unstable very quickly under open-loop inputs, only short segments of data with complete GPS and attitude information could be recorded. As an alternative, the flight tests could have been done entirely under closed-loop control. However, it is preferable to perform a validation of the airship dynamics model using open-loop data since the controller would dominate the airship's response both in the experiment and simulation.

The DGPS setup proved to be unreliable since the position and velocity data transmitted wirelessly from the ground station to the airship would drop out intermittently. This resulted in incomplete data logs on the airship as well as unpredictable behavior from the closed-loop controller, which utilises the altitude and forward speed in its control laws. As a result, only the attitude controller could be used in the flights. Due to the issues with the measured data, we shall only present two flight test cases to validate the dynamics model. The first one analyzes the motion of the airship under free-floating conditions. That is, the airship's motion was recorded as it drifted with the wind, without any applied thruster inputs. The second test case analyzes the response of the airship to thruster inputs.

4.3.1 Wind Estimation

Although the days on which the flights were conducted had relatively low wind, the effect of wind cannot be neglected completely in the simulation as it is bound to have an impact on the behavior of the airship. References [55] and [56] are examples of work in which the mean wind speed, direction, and turbulence are modeled based on field data measured at three altitudes from a wind sensor tower. However, despite the presence of a wind tower at the test site, detailed time histories of wind speeds were not available from it. The wind tower at the Rutherford Park is part of a larger weather station monitored by the Citizen Weather Observer Program(CWOP) [57], who compile data on the measured wind speed, direction, temperature, and humidity on an hourly basis. This data is still useful since it gives us an approximate idea of the conditions at the time of the flight test. The two test flights presented in following sections were conducted on 28th August 2009 and a sample of data from this day is shown in Table 4–1.

The wind direction in Table 4–1 indicates which direction the wind was blowing from and is measured in degrees from geographic north. As an example, a wind direction

Table 4–1: Wind speed and direction at CWTA weather station on 28th August 2009[57]

Time (EDT)	Wind Speed, $\frac{m}{s}$	Wind Direction, deg
8/28/2009 10:00	1.76	10
8/28/2009 11:00	1.32	60
8/28/2009 12:00	1.32	60
8/28/2009 13:00	1.32	60
8/28/2009 14:00	1.32	10

of $+90°$ would indicate a wind blowing from the east. It should be noted that both the wind speed and direction in Table 4–1 are averaged over the previous hour of measurements. From the GPS timestamps in the flight logs, it was determined that the test flights were conducted between 12:00 PM and 1:00 PM. We can see from Table 4–1 that the wind speed and direction do not change over this time span and for the simulation, we choose a constant mean wind speed of 1.32 $\frac{m}{s}$ blowing 60° from the geographic north direction. The mean wind speed can be decomposed along the inertial X (North) and Y (East) axes as shown in equation (4.19). Note that the vertical component of the wind speed has been set to zero since the wind data from CWOP is measured only in the horizontal plane.

$$
\begin{aligned}
(v_{wX})_{Geo} &= -1.32cos(60) = -0.660\frac{m}{s} \\
(v_{wY})_{Geo} &= -1.32sin(60) = -1.143\frac{m}{s} \\
(v_{wZ})_{Geo} &= 0
\end{aligned}
\tag{4.19}
$$

where $(\boldsymbol{v}_w)_{Geo} = [(v_{wX})_{Geo}\ (v_{wY})_{Geo}\ (v_{wZ})_{Geo}]$ is the wind vector expressed in the geographic NED frame. In the simulation, this vector can then be transferred to the body frame by multiplying with the DCM $\boldsymbol{R}_{Geo\to Body}$ defined in equation (2.1).

$$
\boldsymbol{v}_w = \boldsymbol{R}_{Geo\to Body}(\boldsymbol{v}_w)_{Geo} \tag{4.20}
$$

4.3.2 Open-loop Flight without Thrusters

The first test case involves flight of the airship without the thrusters running. Such a test allows us to validate the added mass, drag, gravity and buoyancy models independently from the otherwise-dominant thrust dynamics. Using the experimental setup in Section 4.1, the response of the airship was recorded while it was floating freely under the influence of wind. However, before doing so the airship first had to be brought up to a safe altitude under closed-loop control using the gains $K_{P,\phi} = 0.05\ N/deg$, $K_{I,\phi} = 0.05\ N/deg.s$, $K_{D,\phi} = 0.05\ N.s/deg$, $K_{P,\theta} = 0.05\ N/deg$, $K_{I,\theta} = 0.05\ N/deg.s$, $K_{D,\theta} = 0.05\ N.s/deg$ and a thrust offset $F_{offset} = 2\ N$ per thruster. The complete maneuver consisted of the following parts:

1. The airship was brought up to $\approx$10 m under closed-loop control.
2. All four thrusters were turned off and the airship was allowed to drift back down to the ground.

Of the two parts in the maneuver described above, only the flight data from the second one was used for comparison with the simulation. The wind-field discussed in Section 4.3.1 along with the airship's measured initial conditions at the start of this phase of the flight were used to drive the simulation. Figure 4–6 shows the experimental and simulated inertial position plots (North, East, and Down).

The vertical motion of the airship shows a better match to the experiment than the horizontal (North-East) trajectory. This suggests that the hull volume(and gross lift) chosen in Section 2.2.5 was close to the true value. A maximum error of 1.4 m is seen in the predicted altitude of the airship. At the end of the 8 second simulation, the North position is off by about 6 m and the East position is off by 6.3 m. As explained previously, the constant wind speed(and direction) that have been modeled are averages obtained over an hour of measurements. However in reality, wind

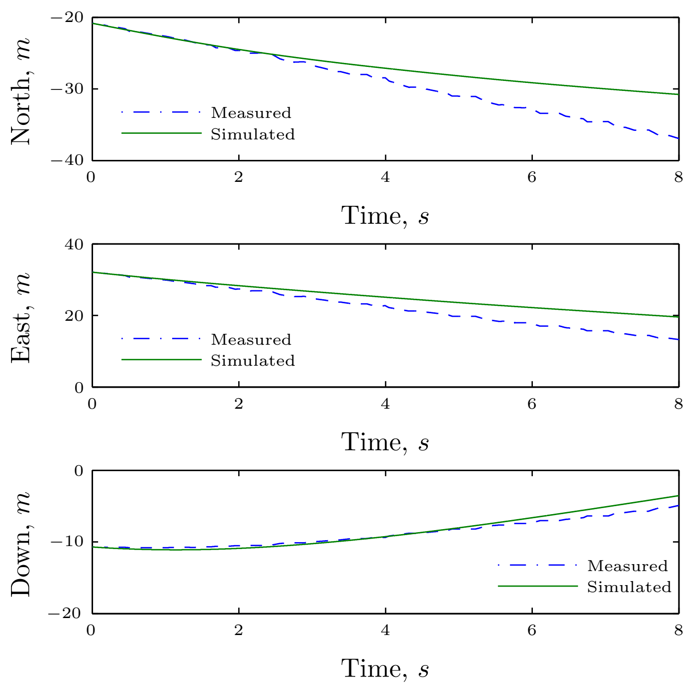

Figure 4–6: Measured and simulated inertial position - North(top), East(middle), Down(bottom)

conditions can be quite erratic and it is unlikely that these mean values represent the conditions experienced by the airship at the time of the test.

To investigate the effect of the chosen wind speed, the same test case was simulated with a wind speed deduced from the measured North and East speeds of the airship. Since the airship was not being propelled by its thrusters, we can assume that it was drifting with a speed equal to the wind speed. From Figure 4–7, the mean horizontal speed of the airship over the 8 second trial is roughly 3.1 m/s. Figure 4–8 shows the airship's North-East trajectory with the original wind speed of 1.32 m/s and the deduced speed of 3.1 m/s. A constant wind direction of 60° from geographic north is used in both cases. The simulated trajectory using a higher mean wind speed is clearly a better match to the experiment. This shows that the airship's dynamics in the absence of any propulsion are significantly influenced by the wind field chosen in the simulation.

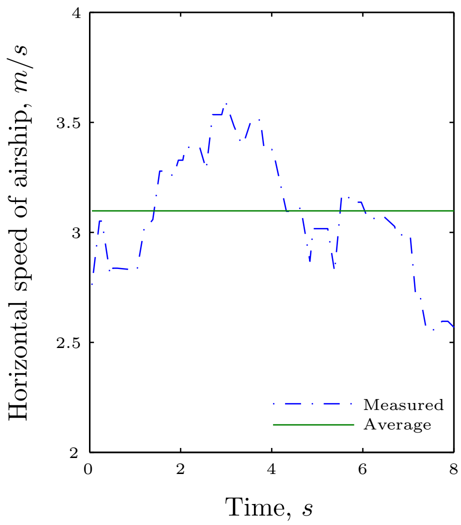

Figure 4–7: Mean horizontal speed of airship

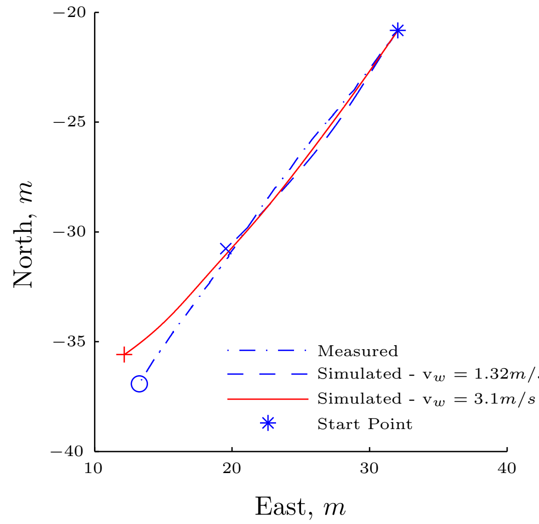

Figure 4–8: Airship trajectories for original and increased wind speed

A comparison of the experimental and simulated Euler angles is shown in Figure 4–9. Note that the simulation uses the wind speed of 1.32 $\frac{m}{s}$ chosen in Section 4.3.1. It can be seen from Figure 4–9 that the roll response of the airship is of similar frequency to the experiment but slightly larger amplitude. In general, the two sets of data are in good agreement with each other. This is expected since the roll motion of the airship is relatively free of aerodynamic moments as a result of which, the motion is akin to that of a pendulum pivoting about the center of buoyancy. If the airship is treated as a rigid body having an inertia I_{xx} about the x axis, with a mass m acting Z_{CG} units below the midplane of the airship, the theoretical period of oscillation may be computed using equation (4.21) and the airship's inertial properties in Table 2–6.

$$\begin{aligned}\gamma &= 2\pi\sqrt{\frac{I_{xx}}{mgZ_{CG}}} \\ &= 2\pi\sqrt{\frac{3.038}{6.346 \times 9.81 \times 11.65 \times 10^{-2}}} \\ &= 4.06s\end{aligned} \tag{4.21}$$

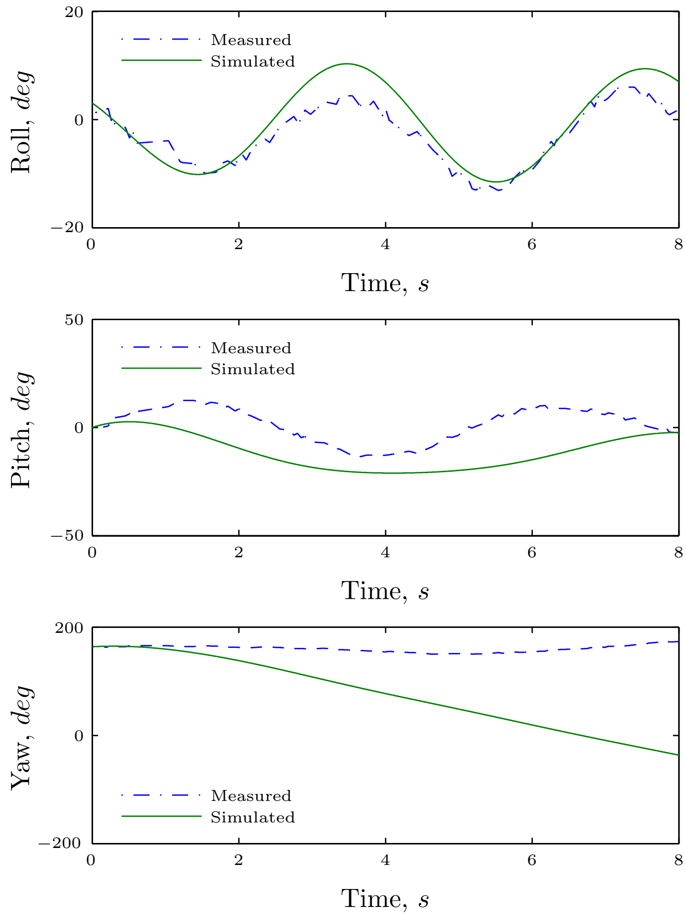

Figure 4–9: Measured and simulated Euler angles - Roll(top), Pitch(middle), Yaw(bottom)

The period of the experimental roll response is ≈3.88 s, roughly 4 % lower than the value computed above. Based on the good match between the periods of the experimental and simulated oscillations, we can conclude that the estimated roll inertia I_{xx} and vertical CG position Z_{CG} are reasonable. The experimental oscillations are centered about a roll angle of ≈-5°. This could be due to the IMU having a roll offset when mounted or due to the presence of a lateral offset in the CG, which has been neglected in the simulation. The maximum error between the simulated and experimental responses is about 5°.

The simulated pitch response is also oscillatory in nature, with a similar amplitude of ≈20° but larger period than the experiment. The period of the experimental response is about 5 seconds compared to 7.5 seconds for the simulated response. The simulated pitch oscillations also appear to be centered about an angle of -10°, in contrast to the experimental data. Unlike the roll response, the pitching motion of the airship cannot be analyzed with a pendulum analogy since there are moments other than the gravitational moment acting about the pitch axis, namely the Munk moment and the moment generated by the viscous drag. Both these moments vary with the airspeed $(\boldsymbol{v} - \boldsymbol{v}_w)$ and are hence sensitive to the wind speed and direction that have been chosen. To demonstrate this, the simulated pitch responses have been obtained with two different wind fields: one with a wind speed of 1.32 $\frac{m}{s}$ and direction +30°, and another with a wind speed of 2.2 $\frac{m}{s}$ and direction +60°. The results are compared in Figure 4–10. It can be seen that the period of the pitch response varies dramatically with changes in the speed and direction of the wind field. Also note that the responses in Figure 4–10 are, in general, fairly close to the experimental data.

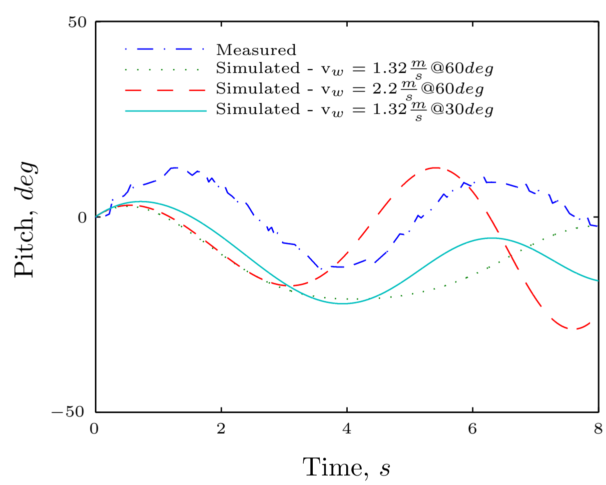

Figure 4–10: Variation in pitch response with different wind fields

Compared to the relatively constant experimental yaw motion, a large change in the simulated yaw angle can be seen in Figure 4–9. Of the three Euler angles, only the yaw does not benefit from the stabilizing action of the airship's vertically(downwards) displaced CG and is relatively less stable. Without further knowledge of the wind conditions during the test, the precise reason for the constant experimental heading is unclear. It is plausible that the airship was drifting with the wind at an airspeed close to zero thereby experiencing a very low Munk moment. We can, however, try to identify possible sources of error in the simulation. A time history of the simulated moments about the airship's z axis (Figure 4–11) shows that a large negative Munk moment is dominant for the first few seconds of the simulation, causing the airship to drift from its initial heading of ≈160°. Once again, this is most likely a result of the wind conditions that were chosen in Section 4.3.1.

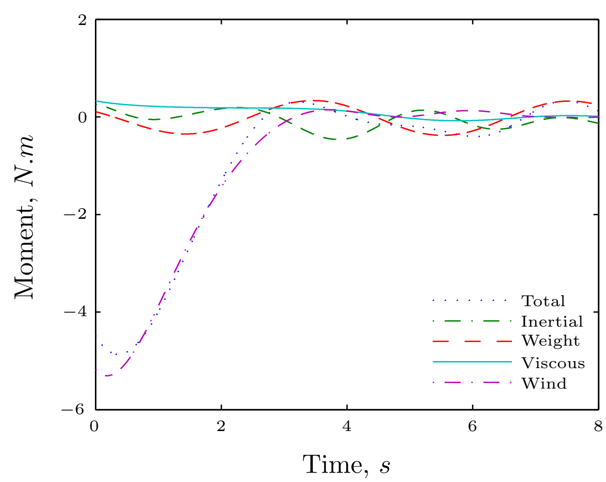

Figure 4–11: Moments about airship z axis

Similar to the pitching motion, the sensitivity of the airship's heading to the chosen wind conditions can be demonstrated by simulating the airship's response under a variety of wind conditions. These results are given in Figure 4–12. For the sake of clarity, the yaw responses have been represented on a scale from 0° to 360° instead of -180° to +180° as output by the dynamics model. The ranges of simulated wind

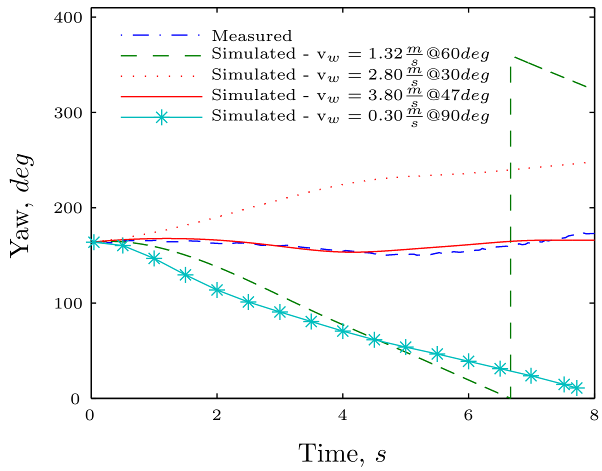

Figure 4–12: Variation in yaw response with different wind fields

speed and direction simulated were 0.2 $\frac{m}{s}$ to 3.8 $\frac{m}{s}$ and 30° to 90° respectively. Given the averaged wind speed and direction of 1.32 $\frac{m}{s}$ and 60° obtained in Section 4.3.1, these ranges are plausible variations in wind conditions that might have occured during the experiment. It can be seen that the evolution of the airship's heading is quite different for each of the wind fields tested. For example, under the influence of a 3.80 $\frac{m}{s}$ wind blowing 47° from true North, the airship exhibits a yaw response that is an excellent match with the near-constant measured heading. Clearly, wind conditions at the test site need to be measured and modeled more accurately in order to better predict the airship's relatively unstable yaw motion.

While the simulated roll and altitude showed a reasonable match with the experimental results, predictions of the airship's pitch, heading, and horizontal (North-East) trajectory had larger errors compared to the experiment. By adjusting the constant wind field in the simulation it was shown that the simulated trajectory of the airship could be improved significantly, which suggests that the present approach to estimate wind conditions is not adequate for modeling the disturbances experienced in outdoor flight. As well, a more realistic model of the wind needs to be implemented in the simulation which includes turbulence and variation in the mean wind speed and direction. In the simulation, the Munk moment had a significant impact on the pitch and yaw dynamics of the MkII. This was most evident in the yaw response, which was seen to drift much more than in the experiment. While the simulated Munk moment depends on the implemented wind model, future research should also focus on identifying the hull's longitudinal and lateral added mass coefficients k_1 and k_2, which govern the Munk moment contribution. In order to facilitate identification of model parameters, future flights should be conducted under more controlled conditions i.e. either in an indoor setting, or outdoors with recorded time histories of the wind speed and direction.

4.3.3 Open-Loop Flight with Thrusters

In the second test case, we compare the simulated and experimental open-loop responses of the airship while subject to thruster forces. During field tests, the MkII proved to be unstable under open-loop thrust inputs as a result of which most tests lasted only a few seconds before the thrusters had to be turned off. Similar to the previous test case, the airship was first stabilized under closed-loop control using the gains $K_{P,\phi} = 0.05\ N/deg$, $K_{I,\phi} = 0.05\ N/deg.s$, $K_{D,\phi} = 0.05\ N.s/deg$, $K_{P,\theta} = 0.05\ N/deg$, $K_{I,\theta} = 0.05\ N/deg.s$, $K_{D,\theta} = 0.05\ N.s/deg$ and a thrust offset $F_{offset} = 2.5\ N$ per thruster. The complete maneuver consisted of the following segments:

1. The airship was brought up to $\approx 5\ m$ under closed-loop control.
2. The thrusters were then commanded to deliver 2.5 N each with the servos tilted forward at 45°. This command was held for 2 seconds.

The data from the second(open-loop) segment was used for comparison with the simulation. Initial conditions for the four thruster models in were set to the closed-loop thrust commands at the timestep before the open-loop sequence began. The airship's initial conditions were set using the measured inertial position and attitude at the start of the open-loop segment. The constant wind field blowing at a speed of 1.32 $\frac{m}{s}$, 60° from true North (described in Section 4.3.1) was applied. The change in the airship's Euler angles over a two second period after application of the thruster inputs can be seen in Figure 4–13.

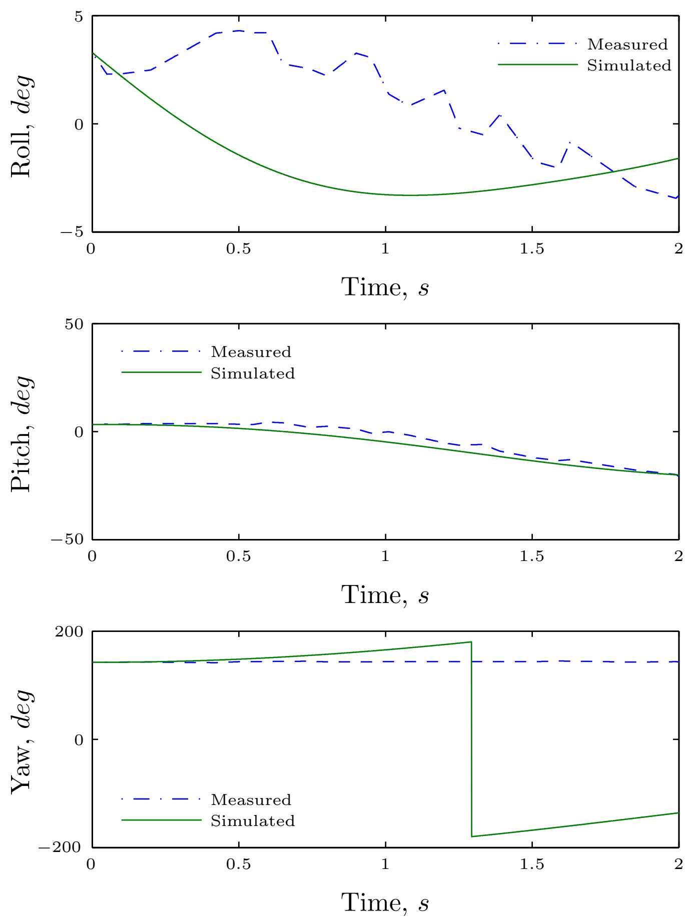

Figure 4–13: Measured and simulated Euler angles - Roll(top), Pitch(middle), Yaw(bottom)

With all four thrusters tilted forward, the airship pitched nose down during the experiment and the simulation reproduces this behavior quite well. Despite a maximum error of ≈6° between the two roll responses the simulation predicts the roll angle well from an order-of-magnitude point of view. Similar to the previous test case, the largest error in the simulation results is seen in the heading. From the plot of the moments about the z axis shown in Figure 4–14, we see once again that the large Munk moment of approximately 10 $N \cdot m$ is most likely what initiates the drift in heading over the simulation run.

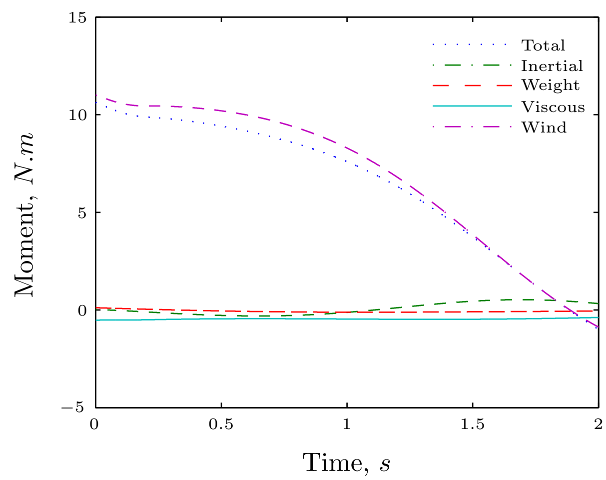

Figure 4–14: Moments about airship z axis

The experimental and simulated inertial position of the airship are compared in Figure 4–15. The North position of the airship shows a very good match with the experiment while the East and Down positions are off by roughly 2.8 m and 1.4 m respectively. Despite the error, the general trend in the simulated East and Down positions matches the experiment. These results are satisfactory considering the simple wind model implemented, but could be improved with a more accurate representation of the wind conditions at the test site.

The results from this open-loop maneuver are by no means a comprehensive validation of the combined vehicle and thruster model. Rigorous testing of the thrusters under the influence of varying ambient winds is required before the airship model can be used for control development. The good agreement in the pitch response of the airship indicates that the peak thrust and transient behavior of the modeled thrusters is comparable to the actual thrusters. Similar to the previous test case,

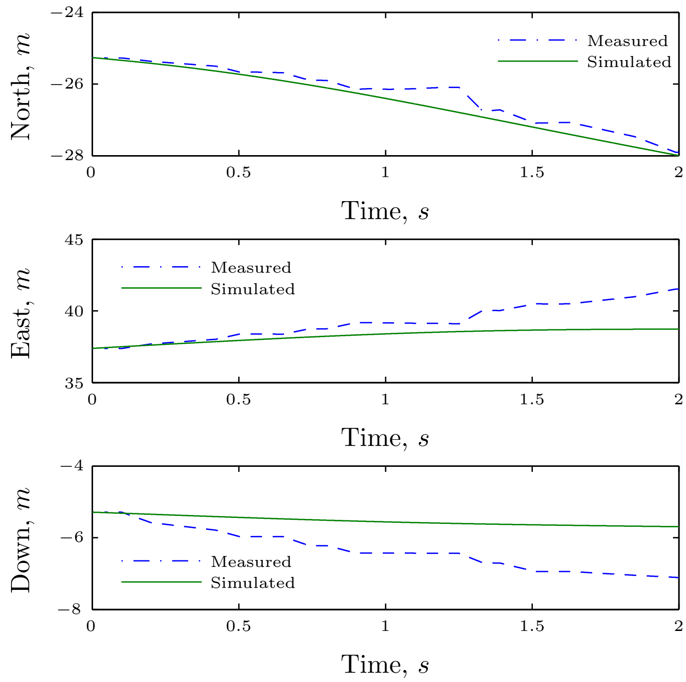

Figure 4–15: Measured and simulated inertial position - North(top), East(middle), Down(bottom)

the largest error in the simulation results is in the yaw angle, which drifted by a large amount even during the short two second simulation run. After examining the moment contributions about the airship's yaw axis, the Munk moment was found to be considerably higher than the other contributions. As stated previously, a wind model based on sensor data from the test site would improve this aspect of the model's performance.

The two test cases that have been analyzed are insufficient to make a definitive statement on the accuracy of the dynamics model. More flight data is required to completely evaluate the various parts of the dynamics model, such as the added mass, drag, and thruster forces. As suggested previously, indoor open-loop flights should be conducted at first so that the effect of wind may be neglected completely in the model validation. Outdoor flights may then be conducted with real-time measurements of the changing wind conditions. However, before conducting further flights, the sensor platform needs to improved to ensure robust data logging under a variety of conditions.

4.3.4 Closed-Loop Flight

In the analysis of the previous test cases, the simulation was shown to be weak in predicting the yaw response of the airship. Despite the model's shortcomings, a simple closed-loop maneuver has been simulated in order to demonstrate the viability of a finless airship when operated under closed loop control. Since the airship simulation also includes the thruster dynamics, we can examine how controllable the airship is in a wind field given a fixed amount of total available thrust. The PID controller described in Section 4.2 was implemented in the airship dynamics model using a thrust offset $F_{offset} = 1.5\ N$ and the gains shown in Table 4–2. It should be noted that these gains were determined iteratively and may not be optimal.

Table 4–2: Control gains used in closed-loop simulation

Gain	Value
$k_{P,\phi}$, $k_{I,\phi}$, $k_{D,\phi}$	0.05 N/deg, 0.01 $N/deg.s$, 0.07 $N.s/deg$
$k_{P,\theta}$, $k_{I,\theta}$, $k_{D,\theta}$	0.28 N/deg, 0.01 $N/deg.s$, 0.22 $N.s/deg$
$k_{P,\psi}$, $k_{I,\psi}$, $k_{D,\psi}$	0.25 N/deg, 0 $N/deg.s$, 0.1 $N.s/deg$
$k_{P,h}$, $k_{I,h}$, $k_{D,h}$	0.4 N/m, 0 $N/m.s$, 0.25 $N.s/m$
$k_{P,u}$, $k_{I,u}$, $k_{D,u}$	0.75 $N.s/m$, 0 N/m, 0 $N.s^2/m$

The wind field for the duration of the maneuver is constant, with a mean wind speed of 0.5 $\frac{m}{s}$ blowing 60° from geographic North. The maneuver begins with the airship level and at rest, oriented at a heading of 45°. The airship takes off under closed-loop control with roll and pitch setpoints of 0°, a heading setpoint of 45°, and a target altitude of 10 m. After 10 seconds, the desired forward speed is set to 0.5 $\frac{m}{s}$ and maintained at this value for the remainder of the simulation. At t=20s, the airship's desired heading is ramped up by 90° over a period of 10 seconds. The desired heading at the end of the ramp input is then held for a period of 10 seconds. This sequence is repeated twice until the airship's heading reaches a value of 315°. Figures 4–16 and 4–17 show the airship's altitude and horizontal (North-East) trajectory during the maneuver. It can be seen from Figure 4–16 that the

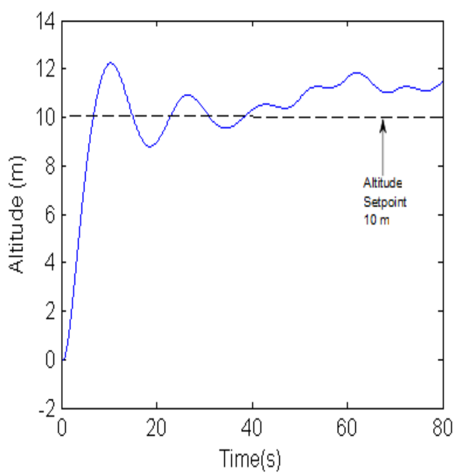

Figure 4–16: Change in the airship's altitude

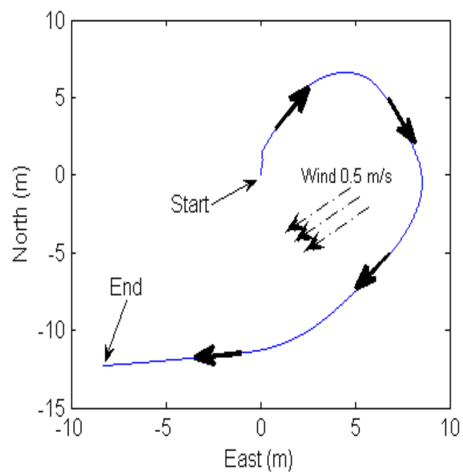

Figure 4–17: North-East trajectory of airship

airship maintains the desired altitude reasonably well but with a maximum error of ± 2 m. Past t$\approx$35s, the airship maintains an altitude between 10 m and 12 m. Since the airship cannot produce downward thrust with the present thruster configuration, its weight brings it back down after overshooting the target value. However, this is not guaranteed to work in the presence of vertical gusts of wind. Furthermore, any upward thrust produced in order to adjust the attitude of the airship can prevent it from descending to the desired height. One solution to this might be to implement propellers with reversible pitch, which would allow the thrust to be reversed rapidly and hence increase the thrust vectoring range of the thrusters to 360°. From the airship's horizontal trajectory(Figure 4–17), it can be seen that the airship's final position is South-West of the starting point. This drift is due to the wind blowing from the North-East, which was not compensated by the closed-loop controller.

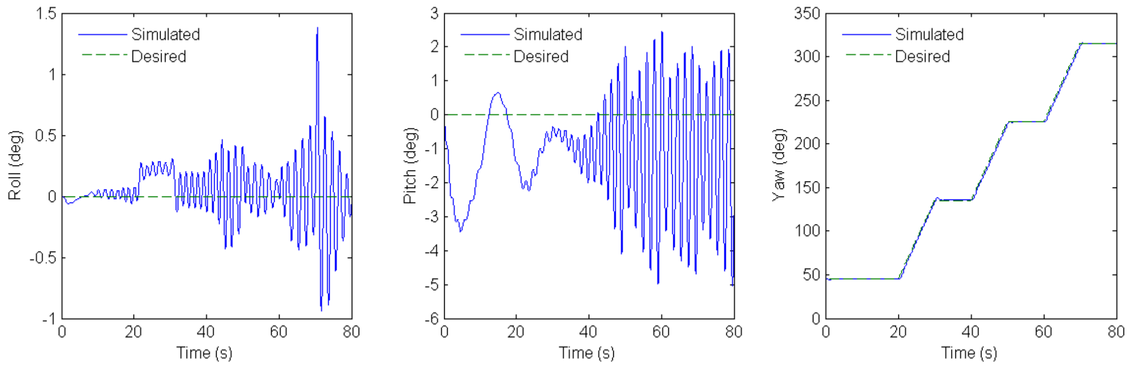

Figure 4–18: Time history of the airship's roll(left), pitch(middle), and yaw(right)

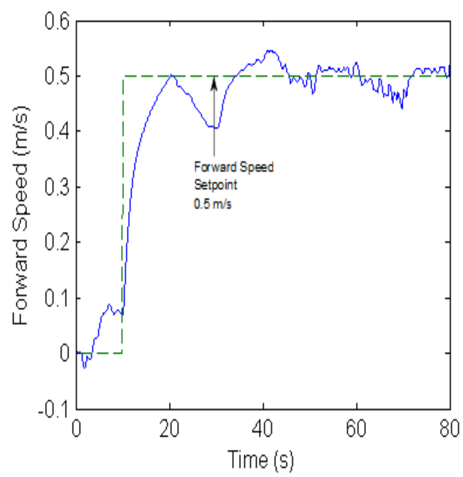

Figure 4–19: Time history of the airship's forward speed

A time history of the airship's Euler angles is shown in Figure 4–18. In general, the controller keeps the pitch and roll excursions to a minimum while tracking the ramp changes in heading with little to no overshoot. A slight drop in forward speed(Figure 4–19) can be seen at t=20s, t=40s, and t=60s when the ramp changes in heading are initiated. Upon completion of the heading change, it can be seen that the forward speed recovers back to the desired value. All in all, the simple proportional speed controller works well, as evidenced by the small maximum error of 0.1 $\frac{m}{s}$ in the forward speed.

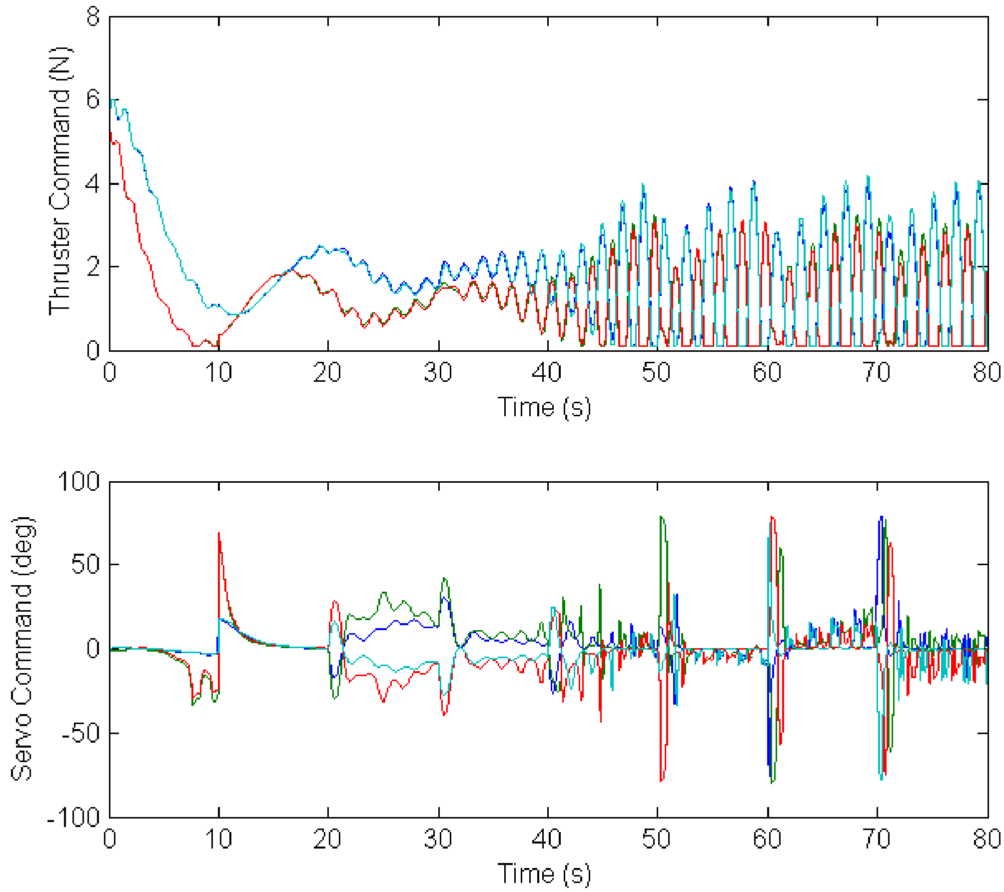

Figure 4–20: Time histories of command thrust(top) and servo angle(bottom)

The command thrust and servo angle for all four of the MkII's thrusters are shown in Figure 4–20. It can be seen that the thrust commands exhibit oscillatory behavior which is of comparable frequency to the roll and pitch oscillations shown in Figure 4–18, approximately 0.5 Hz. The magnitude of the command thrust is quite low for all four thrusters, less than half the available thrust per thruster (11.3 N). The servo angles are somewhat higher and in a few instances reach the maximum available tilt angle ($\pm 90°$ from the vertical). As mentioned in Section 4.2, the level of servo deflection could be reduced by increasing the constant thrust offset F_{offset} in the closed-loop controller.

Under mild wind conditions, the closed-loop results using a simple PID controller are satisfactory. The airship was able to track the reference commands accurately with reasonable thruster and servo commands. However, in order to design controllers for higher wind speeds, a more thorough validation of the airship dynamics model will be required. In particular, two areas that will merit attention are the drag and added mass models. The thruster model will need to be refined to incorporate the effect of ambient wind on the generated thrust, which can be significant in windier conditions.

CHAPTER 5
Conclusion and Future Work

The goal of this work was to develop and validate a non-linear 6 DOF model of the Quanser MkII ALTAV. In the simulation, special attention was paid to two areas, namely: modeling of the thruster dynamics and estimation of the viscous drag acting at large angles of attack. Compared to flight test data, the simulation was found to offer a reasonable prediction of the airship's motion with the exception of the yaw motion. In the sections below, concluding remarks are given for each of the main areas of this work.

5.1 Vehicle Model

In Chapter 2, the 6 DOF non-linear equations of motion were presented followed by the estimation of physical parameters used in them. The profile of the MkII's hull was measured in the lab to obtain a polynomial representation of the shape. In later tests, the internal pressure of the hull was seen to have significant impact on the hull's dimensions, with the diameter increasing by roughly 8 cm over a pressure range of 2.5-5 $mBar$. Because of this, the previously measured hull profile had to be adjusted to reflect the 3.5 $mBar$ internal pressure, which was estimated to exist during the test flights. A CAD model was then constructed and the airship's inertial properties were computed from it. While most CAD values agreed well with the experimental data, the internal volume (and gross lift) were found to have a 11% discrepancy. Since the gross lift is crucial in an airship model, the possible sources of error were analyzed. It was found that the error in the fish scales used in the experiment was not enough to explain the discrepancy. Data from the lab tests also showed that the volume computed from the adjusted hull profile was most probably overestimated. Ultimately, an average of the CAD and experimental volume was used in the dynamics model.

The normal force and pitching moment acting on the airship hull were estimated using a semi-empirical formulation by Jorgensen[34]. It can be applied to airflow at angles of attack up to 360° and was hence ideal for the MkII dynamics model. Since Jorgensen's equations were formulated and validated for slender rocket-like shapes, a number of assumptions had to be made to adapt them to the MkII. The most significant result of these assumptions was the elimination of the potential flow terms.

5.2 Thruster Model

An experimental setup was designed to characterize thruster performance and log force-torque transducer data in real-time. The steady-state thrust for a number of command inputs was determined by recording step responses of the system. At higher thrust levels, a gradual drop in motor speed and thrust was seen in cases where the command was held for a relatively long duration. This was most likely due to a reduction in terminal voltage of the battery, which in turn reduced its capacity. The dependence of thrust on the dynamics of the power source will require further investigation since it is not well understood. The effect of battery voltage was not included in the thruster dynamics model, but this should not have a major impact since we do not expect to hold high thrust commands for long durations. From the step responses, the maximum thrust was determined to be 11.3 N per thruster. The experimental step responses were used to construct a Simulink based dynamics model in the form of an adaptive filter whose time constant and gain vary with the command input. One interesting characteristic of the model is that the response of the system actually slows down (higher time constant) at lower command inputs.

Validation tests showed that the tuned model managed to reproduce the thruster's transient behavior well across the permissible range of command inputs.

A servo model was developed using characteristics deduced from measured sinusoidal responses of the servo. The servo was observed to reach a maximum speed limit of 287 $\frac{deg}{s}$ when subject to high frequency input signals. There was also a constant delay of 48 ms in the measured servo position with respect to the input signal. The servo's dynamics modeled using a rate limiter and transport delay showed an excellent match with experimental data for inputs of varying amplitude and frequency.

5.3 Flight Tests and Model Validation

Initial flights of the MkII showed that it became unstable quickly under open-loop inputs due to the absence of fins. It was therefore necessary to implement a closed-loop controller to stabilize the airship before commencing the open-loop maneuvers. A PID controller was implemented for the airship's attitude, height, and forward speed. Unfortunately, during flight tests, the height and forward speed controllers did not work well since the GPS solution transmitted wirelessly from the ground station did not always reach the airship. It is believed that this was due to interference with the Wi-Fi signals while flying outdoors. As a result, most flight tests were performed with only attitude stabilization. In addition to the wireless communication issues, the GPS antenna also failed to detect satellites when inclined at large angles, which occasionally resulted in poor quality position and velocity data.

Flight tests were conducted at the Rutherford Park, in Montreal. The airship's responses to thruster responses and environmental disturbances was recorded. Using data from a wind tower at the park, wind conditions at the test site were approximated by modeling a constant wind speed and direction in the simulation. The first flight used for model validation was one in which the airship floated freely with the wind without any thruster forces. While the simulated vertical trajectory of the airship showed a good match with the experiment, the horizontal (North-East) trajectory had a large error. By adjusting the wind speed in the model, it was shown that a much better prediction of the airship's trajectory could be obtained. The simulated roll and pitch responses of the airship were also seen to be reasonably close to the measured data. The agreement between the two sets of roll responses provided some validation of the airship's vertical CG displacement and roll inertia. The largest error was in the simulated yaw of the airship, which drifted by a large amount compared to the experiment. This was attributed to the Munk moment, which was found to be dominant over other moments contributions about the yaw axis. Since the Munk moment depends on the wind speed, it was clear that the chosen wind field had a large impact on the resulting yaw motion of the airship.

In the second test case, the airship's experimental response to thruster forces was compared to the simulation. The simulated inertial position of the airship showed reasonable agreement with the experiment, as did the roll and pitch responses. Similar to the first test case, a large discrepancy was present in the simulated yaw of the airship, and again it was determined that the drift in the yaw was due to the Munk moment.

A simple closed loop maneuver was simulated to show the airship's flying qualities under closed-loop control. In a relatively mild wind field, the controller stabilized the roll and pitch of the airship. The reference yaw commands were tracked well with reasonably low servo deflections. The commanded thrust values were not very smooth and exhibited some oscillations. This was most likely because the set of gains chosen for the controller was not optimal. The reference altitude of 10 m was maintained with an error of ± 1 m. However, the forward speed of 0.5 $\frac{m}{s}$ was not maintained well and the airship's speed oscillated between 0.2 $\frac{m}{s}$ and 0.5 $\frac{m}{s}$.

5.4 Future Work

The following suggestions pertain to the dynamics model:

- Future work should focus on incorporating a more realistic wind model based on measured data from the field. Simulation results have shown that the wind model can affect the yaw and pitch responses of the airship through the Munk moment and it is therefore crucial that the wind be modeled more accurately.
- The contribution of the airship hull to the pitch and yaw damping of the airship model should be investigated.
- The effect of the protruding gondola and thruster arms should be included in the axial drag estimation of the airship hull
- Wind-tunnel testing of the thrusters should be conducted to determine the thrust generated under varying ambient winds.
- Gyroscopic moments produced due to the vectoring of thrust should be incorporated into the model. The brushless motors in the MkII's thrusters can spin as fast as 10,000 *rpm* and it is likely that gyroscopic moments are generated while tilting them.
- The effect of battery voltage should be incorporated into the thruster model to better estimate thrust when the battery is being drained.

The following suggestions pertain to the experimental setup:

- In order to identify model parameters, future flights should be conducted under more controlled conditions. Indoor flights are preferred since the effects of wind can be neglected completely. Outdoor flights should include measurements of time histories of the wind speed and direction.
- The reliability of GPS measurements should be improved. One option would be to connect the airship GPS receiver directly to HiQ board. While the

GPS solution would not be as accurate as DGPS, there would be no risk of interruptions in the stream of GPS data.

- The hull profile should be measured at the correct inflation pressure of 3.5 $mBar$.
- The data logging system on the airship should be improved to record data at higher rates.
- A measurement of the gross lift and hull pressure should be performed before commencing flights.

REFERENCES

[1] Image of TCOM-71M aerostat available at http://www.tcomlp.com/71m.htm

[2] Image of AS-300 thermal airship available at http://www.hotairships.com/airships/lindstrand/as300/raft.jpg

[3] Airships: A Hindenburg and Zeppelin History Site: *USS Akron ZRS-4* (n.d.). Retrieved February 8, 2010, from: http://www.airships.net/us-navy-rigid-airships/uss-akron-macon/uss-akron

[4] B. Nagabhushan; D. Lichty; N. Tomlinson: *Control Characteristics of a Buoyant Quad-rotor Research Aircraft,* AIAA Journal of Guidance, Control, and Dynamics, Vol. 6, 1983, pp. 91-99.

[5] B. Nagabhushan; N. Tomlinson: *Thrust-Vectored Takeoff, Landing, and Ground Handling of an Airship,* AIAA Journal of Aircraft, Vol. 23, 1986, pp. 250-256.

[6] B. Nagabhushan; G. Faiss: *Thrust Vector Control of a V/STOL Airship,* AIAA Journal of Aircraft, Vol. 21, 1984, pp. 408-413.

[7] H. Curtiss; V. Sumantran: *Stability and Control of VTOL Capable Airships in Hovering Flight,* AIAA Journal of Guidance, Control, and Dynamics, Vol. 8, 1985, pp. 753-60.

[8] B. Etkin: *Dynamics of Flight: Stability & Control,* Wiley, New York, 3rd ed., 1996, pp. 93-104, 156-159.

[9] W.F. Philips: *Mechanics of Flight,* Wiley, New York, 1st ed., 2004, pp. 599-691.

[10] H. Lamb: *Hydrodynamics,* Dover, New York, 6th ed., 1945, pp. 160-201.

[11] M. B. Tischler; H.R. Jex; R.F. Ringland: *Simulation of Heavy Lift Airship Dynamics over Large Ranges of Incidence and Speed,* AIAA Lighter-Than-Air Systems Technology Conference, Annapolis, MD, July 8-10, 1981, pp. 96-115.

[12] M. B. Tischler; R.F. Ringland: *Heavy-Lift Airship Dynamics,* Journal of Aircraft , Vol. 20, No. 5, 1983, pp. 425-433.

[13] M.B. Tischler; H.R. Jex: *Effects of Atmospheric Turbulence on a Quadrotor Heavy Lift Airship,* Journal of Aircraft , Vol. 20, No. 12, 1983, pp. 1050-1057.

[14] H.R. Jex; R.E. Magdaleno; P. Gelhausen: *Pre and Post-Flight-Test Models versus Measured Skyship-500 Control Responses,* 7th AIAA Lighter-Than-Air Technology Conference, Monterey, CA, August 17-19, 1987, pp. 87-97.

[15] H.R. Jex; J.R. Hogue; P. Gelhausen: *Control Response Measurements of the Skyship-500 Airship,* 6th AIAA Lighter-Than-Air Technology Conference, Norfolk, VA, June 26-28, 1985, pp. 130-141.

[16] J.H. Amann: *A Comparison of a Nonlinear Flight Dynamic Simulation of an Airship with Flight Test Results,* 7th AIAA Lighter-Than-Air Technology Conference, Monterey, CA, August 17-19, 1987, pp. 78-86.

[17] S.P. Jones; J.D. Delaurier: *Aerodynamic Estimation Techniques for Aerostats and Airships,* AIAA Journal of Aircraft, Vol. 20, No. 2, 1983, p. 120-126.

[18] D.B. Bailey: *Patrol Airship Concept Evaluation (PACE),* Naval Air Development Center, Airtask No. 62241N/F41-411/DH814, March 1985.

[19] S.B.V. Gomes; J.G. Ramos Jr: *Airship Dynamic Modeling for Autonomous Operation,* Proceedings of IEEE International Conference on Robotics and Automation, Vol. 4, 1998, pp. 3462-3467.

[20] T. Yamasaki; N. Goto: *Identification of Blimp Dynamics via Flight Tests,* Transactions of the Japan Society for Aeronautical and Space Sciences, Vol. 46, No. 153, 2003, pp. 195-205.

[21] Y. Li; M. Nahon: *Simulation of Airship Dynamics,* AIAA Journal of Guidance, Control, and Dynamics, Vol. 30, No. 6, 2007, pp. 1691-1700.

[22] T. Lutz; P. Funk; A. Jakobi; S. Wagner: *Summary of Aerodynamic Studies on the Lotte Airship,* 4th International Airship Convention and Exhibition, July 28-31, 2002, Cambridge, England. a

[23] P.G. Thomasson: *On the Equations of Motion of a Vehicle in a Moving Fluid,* AIAA Journal of Aircraft, Vol. 37, No. 4, 2000, pp. 630-639.

[24] J.R. Azinheira; E.C. Paiva; S.S. Bueno: *Influence of Wind Speed on Airship Dynamics,* AIAA Journal of Guidance, Control and Dynamics, Vol. 25, No.6, 2002, pp. 1116-1124.

[25] J.R. Azinheira; A. Moutinho; E.C. Paiva: *Erratum - Influence of Wind Speed on Airship Dynamics,* AIAA Journal of Guidance, Control and Dynamics, Vol. 31, No. 2, 2008, pp. 443-444.

[26] P. Peddiraju; T. Liesk; M. Nahon: *Dynamics Modeling for an Unmanned, Unstable, Fin-less Airship,* 18th AIAA Lighter-Than-Air Systems Technology Conference, Seattle, Washington, 2009.

[27] M. V. Cook; J. M. Lipscombe; F. Goineau: *Analysis of the Stability Modes of the Non-Rigid Airship,* The Aeronautical Journal , Vol. 104, No. 1036, 2000, pp. 279-290.

[28] M.M. Munk: *The Aerodynamic Forces on Airship Hulls,* NACA TR 184, 1924.

[29] H. Allen; E. Perkins: *A Study of Effects of Viscosity on Flow Over Slender Inclined Bodies of Revolution,* NACA Report No. 1048, 1951.

[30] E. J. Hopkins: *A Semi-empirical Method for Calculating the Pitching Moment of Bodies of Revolution at Low Mach Numbers,* NACA RM A51C14, 1951.

[31] Y. Li: *Dynamics Modeling and Simulation of Flexible Airships,* Ph.D Thesis, McGill University, 2007.

[32] K.P. Watson; J.S. Webster; J.W. Crane; N.S. Smith: *Prediction of Submersible Maneuvering Performance at High Incidence Angles,* OCEANS '93. Engineering in Harmony with Ocean Proceedings (Cat. No.93CH3341-5), II289-94 vol.2, 1993.

[33] M. Battipede; M. Lando; P. Gili: *Mathematical Modelling of an Innovative Unmanned Airship for its Control Law Design,* IFIP Systems, Control, Modeling and Optimization, Volume 202, 2006, pp. 31-42.

[34] L. Jorgensen: *Prediction of Static Aerodynamic Characteristic for Space-Shuttle-Like and Other Bodies at Angles of Attack from 0° to 180°,* NASA TN D-6996, January 1973.

[35] P. Pounds; R. Mahony; P. Corke: *Modelling and Control of a Quad-Rotor Robot,* Proceedings of the 2006 Australasian Conference on Robotics & Automation, Auckland, New Zealand, 2006.

[36] P. Pounds; R. Mahony; P. Corke: *System Identification and Control of an Aerobot Drive System,* Information, Decision and Control, February 2007, pp 154-159.

[37] A. Healey; S. Rock; S. Cody; D. Miles; J. Brown: *Toward an Improved Understanding of Thruster Dynamics for Underwater Vehicles,* IEEE Journal of Oceanic Engineering, Vol. 20, 1995, pp. 354-361.

[38] L. Whitcomb; D. Yoerger: *Development, Comparison, and Preliminary Experimental Validation of Nonlinear Dynamic Thruster Models,* IEEE Journal of Oceanic Engineering, vol. 24, 1999, pp. 481-94.

[39] A. Saunders; M. Nahon: *The Effect of Forward Vehicle Velocity on Through-body AUV Tunnel Thruster Performance,* Oceans 2002 Conference and Exhibition. Conference Proceedings, 29-31 Oct. 2002, Piscataway, NJ, USA, 2002, pp. 250-259.

[40] D. Yoerger; J. Cooke; J. Slotine: *The Influence of Thruster Dynamics on Underwater Vehicle Behavior and their Incorporation into Control System Design,* IEEE Journal of Oceanic Engineering, Vol. 15, 1990, pp. 167-178.

[41] Berkley Fishing: *Berkley Tournament Fish Scale - 15lb. Digital Specifications* (n.d.). Retrieved January 5, 2010, from http://www.berkley-fishing.com/

[42] UEI Test and Measurement Instruments: *UEI EM201/151 Datasheet* (n.d.) Retrieved January 8, 2010, from http://www.ueitest.com

[43] T.Dorion: 20° *Short History of the Standard Reference Temperature for Industrial Dimensional Measurements,* Journal of Research of the National Institute of Standards and Technology, Volume 112, Number 1, January-February 2007.

[44] T.I. Fossen: *Guidance and Control of Ocean Vehicles,* Wiley, United Kindom, 1994, pp. 5-42.

[45] L.E. Ericsson; J.P. Reding: *Asymmetric Vortex Shedding from Bodies of Revolution,* Progress in Astronautics and Aeronautics, Tactical Missile Aerodynamics, Vol. 104, 1986, pp. 243-296.

[46] J. Evans; M. Nahon: *Dynamics Modeling and Performance Evaluation of an Autonomous Underwater Vehicle,* Ocean Engineering, Vol. 31, 2004, pp. 1835-1858.

[47] S.F. Hoerner: *Fluid Dynamic Drag,* Hoerner Fluid Dynamics, 1965.

[48] PJS Motors: *Technical Information* (n.d.) Retrieved March 12, 2009, from http://www.pjs.cz/produkty/informace/800-1000/index2.htm

[49] The Electropadeia: *Battery Performance Characteristics - How to Specify and Test a Battery* (n.d.) Retrieved January 27, 2010, from http://www.mpoweruk.com/performance.htm

[50] PJRC: *Teensy++ USB Development Board* (n.d.) Retrieved January 14, 2010, from http://www.pjrc.com/store/teensypp.html

[51] Arduino: *Arduino - Servo*(n.d.) Retrieved January 14, 2010, from http://arduino.cc/en/Reference/Servo

[52] The Mathworks: *Zero-phase Digital Filtering* (n.d.) Retrieved February 1, 2010, from http://www.mathworks.com/access/helpdesk/help/toolbox/signal/filtfilt.html

[53] Natural Resources Canada: *GSC - Geomagnetism - Magnetic Declination Calculator* (2009-11-6) Retrieved October 6, 2009, from http://geomag.nrcan.gc.ca/apps/mdcal-eng.php

[54] Google: *Google Maps* (n.d.) Retrieved January 30, 2010, from http://maps.google.ca

[55] A. Howard: *Experimental Characterization and Simulation of a Tethered Aerostat with Controllable Tail Fins,* Master's Thesis, McGill University, 2007.

[56] P. Coulombe-Pontbriand: *Modeling and Experimental Characterization of a Tethered Spherical Aerostat,* Master's Thesis, McGill University, 2005.

[57] Citizen Weather Observer Program (CWOP): *METAR/Synop Information for CWTA in Mctavish, QB, Canada* (2010-24-01) Retrieved November 12, 2009, from http://weather.gladstonefamily.net/site/CWTA

Appendices

APPENDIX A
Experimental and simulated thruster step responses

Figures A–1 to A–5 show the experimental and simulated step thrust responses to command inputs of 0.20, 0.30, 0.35, 0.40 and 0.45.

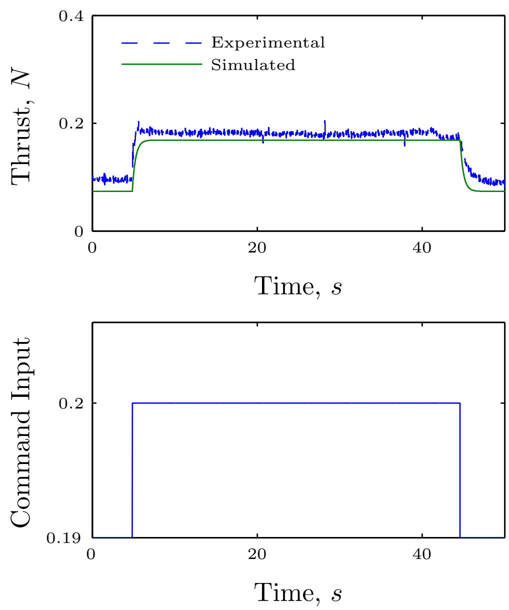

Figure A–1: Simulated and experimental responses (top) to step command input of 0.20(bottom).

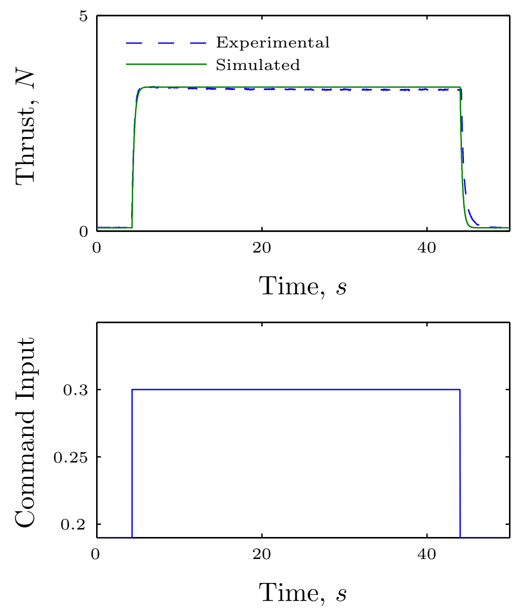

Figure A–2: Simulated and experimental responses (top) to step command input of 0.30(bottom).

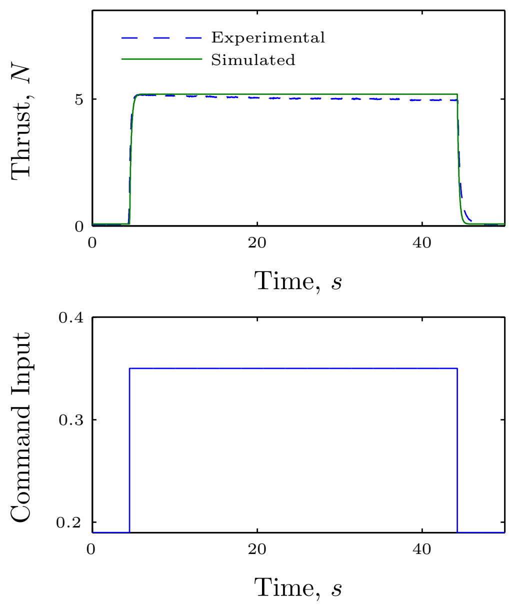

Figure A–3: Simulated and experimental responses (top) to step command input of 0.35(bottom).

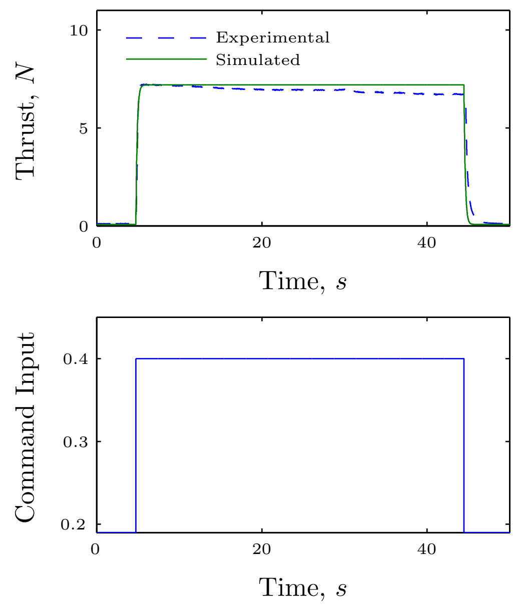

Figure A–4: Simulated and experimental responses (top) to step command input of 0.40(bottom).

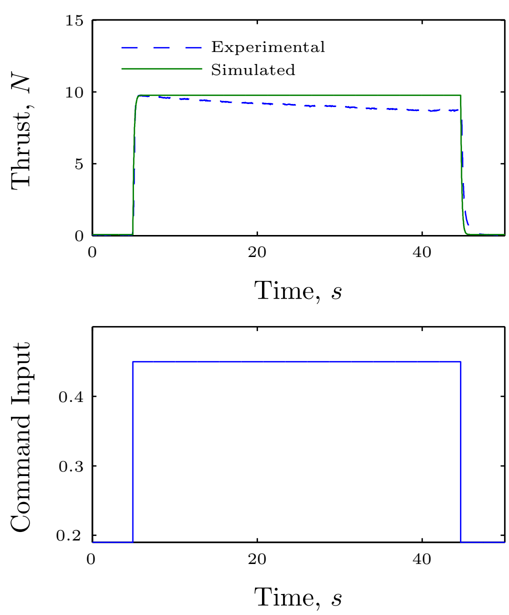

Figure A–5: Simulated and experimental responses (top) to step command input of 0.45(bottom).